

# Hydrogen Storage Materials for Remote Area Power Supply, Movable Power Supply and Automotive Applications

**Author:**

Tseng, Yu-Sheng

**Publication Date:**

2018

**DOI:**

<https://doi.org/10.26190/unsworks/3557>

**License:**

<https://creativecommons.org/licenses/by-nc-nd/3.0/au/>

Link to license to see what you are allowed to do with this resource.

Downloaded from <http://hdl.handle.net/1959.4/60555> in <https://unsworks.unsw.edu.au> on 2024-04-19

# **Hydrogen Storage Materials for Remote Area Power Supply, Movable Power Supply and Automotive Applications**

**Yu-Sheng Tseng**

Associate Professor Sammy Lap Ip Chan

A thesis in fulfilment of the requirements for the degree of

**Doctor of Philosophy**



School of Materials Science and Engineering

Faculty of Science

October 2018



## Thesis/Dissertation Sheet

|  |   |
|--|---|
| Surname/Family Name  | : Tseng   |
| Given Name/s   | : Yu-Sheng  |
| Abbreviation for degree as give in the University calendar | : PhD   |
| Faculty  | : Science   |
| School   | : Materials Science and Engineering   |
| Thesis Title   | : Hydrogen Storage Materials for Remote Area Power Supply, Movable Power Supply and Automotive Applications |

### Abstract 350 words maximum: (PLEASE TYPE)

Air pollution, global warming and the imminent exhaustion of fossil fuels drive people to use renewable energy to replace hydrocarbon fuels. Hydrogen is one of the most promising energy carriers to harvest the intermittent renewable energy. There are basically three types of applications: stationary Remote Area Power Supply (RAPS), Movable Power Supply (MPS) and automotive vehicles. The aim of this research is to develop suitable hydrogen storage materials for these three applications. In this study,  $V_{80}Ti_8Cr_{12}$  alloy was designed to meet the requirements of RAPS and MPS applications. The effects of particle size and mechanical treatment on the hydrogen storage properties of  $V_{80}Ti_8Cr_{12}$  alloy have been investigated. Briefly, the 5 mm  $V_{80}Ti_8Cr_{12}$  alloy has 2 wt% of usable hydrogen capacity under 20-50 °C and 0.2-2 MPa, which is 40% higher than commercial AB<sub>5</sub> alloys and fully satisfies the capacity needs of RAPS and MPS systems. The alloy provides a rapid hydrogen supply rate which is 9 times faster than the requirement. The alloy possesses an excellent cycle life up to 500 cycles with a 90 % of capacity retention.  $C_3N_4$  tubes were selected as the hydrogen storage materials for automotive applications because of their high theoretical hydrogen capacity (5.45 wt%) which reaches 2025 US DOE target. Currently, compressive hydrogen is used in fuel cell vehicles with 70 MPa of pressure, leading to uncertain hazards and extra energy consumption.  $C_3N_4$  tubes may potentially reduce the pressure from 70 MPa to several MPa without a significant capacity loss. The highest hydrogen capacity achieved in this work is 0.62 wt% at 3.6 MPa. This value corresponds to a surface area of 148.69 m<sup>2</sup>/g which is so far the highest record in N-rich  $C_3N_4$  tubes. The hydrogen capacity is predicted as 2.62 wt% at 10 MPa.  $C_3N_4$  tubes have a swift recharging speed (2-3 minutes), which is competitive to the refuelling of petrol. The special thermal dynamics enables  $C_3N_4$  tubes to absorb and desorb hydrogen at ambient conditions. Besides the material study, a novel and time-saving approach was developed to precisely measure the hydrogen capacity at various absorption/desorption temperatures.

### Declaration relating to disposition of project thesis/dissertation

I hereby grant to the University of New South Wales or its agents the right to archive and to make available my thesis or dissertation in whole or in part in the University libraries in all forms of media, now or here after known, subject to the provisions of the Copyright Act 1968. I retain all property rights, such as patent rights. I also retain the right to use in future works (such as articles or books) all or part of this thesis or dissertation.

I also authorise University Microfilms to use the 350 word abstract of my thesis in Dissertation Abstracts International (this is applicable to doctoral theses only).

|           |                   |            |
|-----------|-------------------|------------|
| .....     | .....             | 29.03.2018 |
| Signature | Witness Signature | Date       |

The University recognises that there may be exceptional circumstances requiring restrictions on copying or conditions on use. Requests for restriction for a period of up to 2 years must be made in writing. Requests for a longer period of restriction may be considered in exceptional circumstances and require the approval of the Dean of Graduate Research.

**FOR OFFICE USE ONLY** Date of completion of requirements for Award:

## **COPYRIGHT STATEMENT**

'I hereby grant the University of New South Wales or its agents the right to archive and to make available my thesis or dissertation in whole or part in the University libraries in all forms of media, now or here after known, subject to the provisions of the Copyright Act 1968. I retain all proprietary rights, such as patent rights. I also retain the right to use in future works (such as articles or books) all or part of this thesis or dissertation.

I also authorise University Microfilms to use the 350 word abstract of my thesis in Dissertation Abstract International (this is applicable to doctoral theses only).

I have either used no substantial portions of copyright material in my thesis or I have obtained permission to use copyright material; where permission has not been granted I have applied/will apply for a partial restriction of the digital copy of my thesis or dissertation.'

Signed .....

Date 18. 10. 2018 .....

## **AUTHENTICITY STATEMENT**

'I certify that the Library deposit digital copy is a direct equivalent of the final officially approved version of my thesis. No emendation of content has occurred and if there are any minor variations in formatting, they are the result of the conversion to digital format.'

Signed .....

Date 18. 10. 2018 .....

## Originality Statement

I hereby declare that this submission is my own work and to the best of my knowledge it contains no materials previously published or written by another person, or substantial proportions of material which have been accepted for the award of any other degree or diploma at UNSW or any other educational institution, except where due acknowledgement is made in the thesis. Any contribution made to the research by others, with whom I have worked at UNSW or elsewhere, is explicitly acknowledged in the thesis. I also declare that the intellectual content of this thesis is the product of my own work, except to the extent that assistance from others in the project's design and conception or in style, presentation and linguistic expression is acknowledged.

Signed .. .. .

Date .....29.03.2018.....

# Abstract

Air pollution, global warming and the exhaustion of fossil fuels by the coming several decades drive people to use renewable energy instead of hydrocarbon fuels. Renewable energy is a desired green technology both in the developed world and developing world due to its abundance and low carbon emission. Hydrogen is one of the most promising energy carriers to harvest the intermittent sustainable energy (e.g. solar, wind and hydro). The renewable energy stored in hydrogen form can be converted to electricity by the electrochemical reaction of hydrogen and oxygen in fuel cells. There are basically three different types of applications: stationary, mobile and automotive. The requirements of these three applications are different in terms of hydrogen storage capacity, operating conditions (temperature and pressure), charge/discharge rate and cycle life.

About one quarter of mankind in the world are dwelling in areas without electricity connection from centralized power plants. The cost of extending electricity grids to remote communities is very high and thus relatively unaffordable to these communities. Many efforts were made to establish a self-sustaining system that can provide reliable energy without the power grids. However, the main barrier limiting the development of this standalone remote area power supply (RAPS) is the energy storage system that is able to guarantee continuous electricity supply. The first part of this research has been the application of hydrogen storage materials to store hydrogen synthesized from the surplus energy of the sustainable power supply (e.g. solar energy) by electrolysis. The hydrogen source was then used to power the fuel cell to supply electricity when the external energy source is unavailable. Here solid-state hydrogen storage materials were employed for this purpose owing to their excellent volumetric storage density. Vanadium alloys were selected as the hydrogen carrier in the RAPS, since they can also find applications in

Movable Power Supply (MPS) systems. In the second part, the scope of this research extended to the hydrogen storage materials designed specially for hydrogen-powered automotive vehicles. Carbon nitride ( $C_3N_4$ ) tubes have been chosen as the potential candidate for this application.

In this study, a vanadium-based alloy was designed and tailored to meet the requirements of RAPS and MPS applications. The alloy design was carried out by comparing the properties of many hydrogen storage alloys and materials with different chemical compositions. The system requirements were then introduced to optimize the alloy composition, and the hydrogen storage performance of the designed alloy was predicted and assessed.  $V_{80}Ti_8Cr_{12}$  alloy was finalized as the optimum hydrogen storage alloy for RAPS and MPS systems. Since the MPS system specifically required the working conditions to be  $H_2$  absorption at 20 °C at 2 MPa and desorption at 50 °C at 0.2 MPa, a special isothermal hydrogen measurement was implemented in this work to simulate these requirements, and thereby the actual usable hydrogen capacity can be obtained under these operating circumstances. This new method is more accurate and time-saving as compared to the traditional isotherm, where the hydrogenation and dehydrogenation were carried out at a fixed temperature.

The designed  $V_{80}Ti_8Cr_{12}$  alloy was found to have a maximum hydrogen capacity of 3.5 wt% which was 2.5 times higher than the commercial  $LaNi_5$  type alloys (1.4-1.5 wt%). Because part of the  $H_2$  amount could not be released at ambient conditions, the usable hydrogen capacity of  $V_{80}Ti_8Cr_{12}$  alloy dropped to 2 wt%, which was still 40% higher than that of  $LaNi_5$ . Since the effect of particle size on the hydrogen storage properties of high V-containing alloys has not been clearly clarified, it was investigated in this present work. The mechanically sectioned samples with particle sizes from 5 mm to less than 100  $\mu m$

had descending usable capacities with the reduction of particle sizes and lattice constants. However, the sample with 7 mm of particle size didn't absorb hydrogen, indicating the upper limit of the alloy size. The kinetics was basically enhanced with the decrease of particle size, where the H<sub>2</sub>-embrittled samples have better overall performance. These suggested that the excessively large or small particle sizes both brought about negative influence on the H<sub>2</sub> properties. The optimized alloy size was worked out in this study. Briefly, the V<sub>80</sub>Ti<sub>8</sub>Cr<sub>12</sub> alloy with 5 mm of particle size had around 2 wt% of usable hydrogen capacity under 20-50 °C and 0.2-2 MPa, which fully satisfies the capacity needs of RAPS and MPS applications. Besides, the alloy was able to provide a rapid hydrogen supply rate which is 9 times faster than the requirement. The alloy also possessed an excellent cycle life up to 500 cycles with a 90 % of capacity retention. Compared to other room-temperature operational alloys with high H<sub>2</sub> capacities, V<sub>80</sub>Ti<sub>8</sub>Cr<sub>12</sub> alloy has a similar cycle stability with AB<sub>2</sub> type alloys, but a far superior durability to AB<sub>3</sub> type alloys (~40% drop after 500 cycles). Therefore, the 5 mm V<sub>80</sub>Ti<sub>8</sub>Cr<sub>12</sub> alloy has been shown in this work a promising candidature for the hydrogen storage in RAPS and MPS systems.

C<sub>3</sub>N<sub>4</sub> tubes were selected as the hydrogen storage materials for automotive applications because of their high theoretical hydrogen capacity (5.45 wt%) which reaches the 2025 target proposed by US Department of Energy. Currently, the hydrogen used in fuel cell vehicles is stored in compressive gas form with 70 MPa of pressure, leading to uncertain hazards and extra energy consumption for compression. C<sub>3</sub>N<sub>4</sub> tubes may potentially reduce the storage pressure from 70 MPa to several MPa by accumulating hydrogen in solid form. Due to the light weight of carbon and nitrogen, the gravimetric energy density is expected to be much higher than that of conventional metal hydrides. Up to date, tubular C<sub>3</sub>N<sub>4</sub> is generally prepared by syntheses required sophisticated facilities (chemical vapor deposition and sputtering), catalysts, substrates/templates, strong acid/base, toxic solvent,



etc. These may give complex and costly production processes which are not applicable for commercialization. In our work,  $C_3N_4$  tubes were synthesized by a facile method adopting the hydrothermal treatment and pyrolysis of sole melamine without any additives. The optimum parameters of material preparation are described as the followings. 10 % of melamine solution with 85 % of filling ratio is heated at 205 °C for 24 hours, followed by a pyrolysis in a sealed crucible with alumina partitions under 560 °C in air for 4 hours with 5 °C/minute of ramping rate. The hydrogen storage properties of  $C_3N_4$  tubes (nitrogen content: ~50 at%) have been measured for the first time. Tubular carbon nitrides have an improved hydrogen uptake with the increase of surface area. The optimized hydrogen capacity achieved in this work is 0.62 wt% at 3.6 MPa. This value corresponds to the surface area of 148.69 m<sup>2</sup>/g which is so far the highest record in N-rich  $C_3N_4$  tubes. The hydrogen capacity is predicted to reach 2.62 wt% at 10 MPa. Moreover,  $C_3N_4$  tubes have a swift charge and discharge speed (2-3 minutes), which allows the refuelling competitive to that of petrol. Last but not least, the special thermal dynamics enables  $C_3N_4$  tubes to absorb and desorb hydrogen at ambient conditions. In the future, if a catalyst doping and an enlargement of surface area are employed, the hydrogen capacity of  $C_3N_4$  tubes may be further improved at low H<sub>2</sub> pressure.

In RAPS and MPS systems, V-based alloy can be an ideal hydrogen storage medium because of its low operating pressure, which is beneficial for charged by electrolyzers, and reasonable capacity (2 wt%). However, a much higher H<sub>2</sub> capacity and a higher hydrogen charging pressure are necessary for the automotive field (5.5 wt%); and tubular  $C_3N_4$  could be a promising candidate to reach the goal and store hydrogen in a much safer pressure (several MPa) compared to that in the prevailed pressurized tanks (70 MPa). Thus, this research has successfully demonstrated different material systems to be used in RAPS, MPS and automotive applications.

# Table of Contents

|                                   |  |
|-----------------------------------|--|
| <b>Originality Statement.....</b> | <b>i</b>   |
| <b>Abstract.....</b>              | <b>ii</b>  |
| <b>Table of Contents.....</b>     | <b>vi</b>  |
| <b>List of Figures.....</b>       | <b>viii</b>  |
| <b>List of Tables.....</b>        | <b>xii</b>   |
| <b>List of Equations .....</b>    | <b>xii</b>   |
| <b>Chapter 1</b>                  | <b>Introduction ..... 1</b>  |
| 1.1                               | Background ..... 1   |
| 1.2                               | Project Target..... 4  |
| <b>Chapter 2</b>                  | <b>Literature Review ..... 8</b>   |
| 2.1                               | Framework of Remote Area Power Supply (RAPS) and<br>Movable Power Supply (MPS) ..... 8 |
| 2.2                               | Framework of Hydrogen Storage in Automotive Field..... 12                              |
| 2.3                               | Hydrogen as an Energy Carrier ..... 15   |
| 2.3.1                             | Gaseous Hydrogen Storage ..... 16  |
| 2.3.2                             | Cryogenic Liquid Hydrogen Storage ..... 17   |
| 2.3.3                             | Solid-state Hydrogen Storage..... 20   |
| <b>Chapter 3</b>                  | <b>V-Ti-Cr based BCC Solid Solution ..... 31</b>                                       |
| 3.1                               | Introduction ..... 31  |
| 3.2                               | Alloy Design ..... 41  |
| 3.3                               | Materials and Experimental Procedure ..... 46  |
| 3.3.1                             | Fabrication of Alloys..... 46  |
| 3.3.2                             | Alloy Characterizations ..... 47   |
| 3.4                               | Alloy Composition, Morphology and Crystal Structure ..... 49                           |
| 3.4.1                             | Composition Analysis ..... 49  |
| 3.4.2                             | Element Distribution in Alloy Ingot..... 50  |
| 3.4.3                             | Morphology..... 52   |
| 3.4.4                             | Phase Identification and Crystal Structure ..... 54                                    |
| 3.5                               | Hydrogen Storage Properties ..... 57   |
| 3.5.1                             | Absorption Kinetics ..... 57   |

|                         |   |            |
|-------------------------|---|------------|
| 3.5.2                   | Measurements for Usable Hydrogen Storage Capacity ...   | 59         |
| 3.5.3                   | Cycle Stability .....   | 63         |
| 3.5.4                   | Desorption Kinetics .....   | 65         |
| 3.6                     | Conclusion.....   | 69         |
| <b>Chapter 4</b>        | <b>Synthesis of Tubular Carbon Nitrides .....</b>   | <b>70</b>  |
| 4.1                     | Introduction .....  | 70         |
| 4.2                     | Materials and Experimental Procedure .....  | 81         |
| 4.2.1                   | Preparation of Carbon Nitride Micro/Nano Tubes .....  | 81         |
| 4.2.2                   | Characterizations .....   | 83         |
| 4.3.                    | Results and Discussion.....   | 83         |
| 4.3.1                   | Hydrothermal Treatment Studies .....  | 83         |
| 4.3.2                   | Calcination Studies for Carbon Nitride Tubes .....  | 94         |
| 4.4                     | Conclusion.....   | 104        |
| <b>Chapter 5</b>        | <b>Characterizations and Hydrogen Storage Properties of<br/>Tubular Carbon Nitrides .....</b> | <b>105</b> |
| 5.1                     | Introduction .....  | 105        |
| 5.2                     | Experimental Procedure .....  | 106        |
| 5.2.1                   | Characterizations .....   | 106        |
| 5.2.2                   | Hydrogen Storage Properties.....  | 106        |
| 5.3                     | Surface Properties and Structure Analysis .....   | 108        |
| 5.3.1                   | Composition Analysis.....   | 108        |
| 5.3.2                   | Surface Area Analysis .....   | 111        |
| 5.3.3                   | Phase Identification and Crystal Structure .....  | 114        |
| 5.3.4                   | Chemical Structure.....   | 116        |
| 5.4                     | Hydrogen Storage Properties .....   | 117        |
| 5.4.1                   | Absorption Hydrogen Capacity .....  | 117        |
| 5.4.2                   | Hydrogen Capacity at Various Temperatures.....  | 119        |
| 5.4.3                   | Chemisorption Measurement.....  | 120        |
| 5.4.4                   | Absorption and Desorption Kinetics .....  | 121        |
| 5.5                     | Conclusion.....   | 122        |
| <b>Chapter 6</b>        | <b>Final Remarks and Future Work.....</b>   | <b>123</b> |
| 6.1                     | Conclusion.....   | 123        |
| 6.2                     | Future Work.....  | 125        |
| <b>References .....</b> |   | <b>128</b> |

# List of Figures

|              |  |    |
|--------------|--|----|
| Figure 2.1:  | Stand-alone remote area power supply with photovoltaic sources, which ensures the uninterrupted electricity output by hydrogen production from electrolysis, hydrogen storage, electricity supply via fuel cells [1].  | 9  |
| Figure 2.2:  | A self-powered living unit based on PV system. The roof was equipped with solar panels for energy generation [4].  | 9  |
| Figure 2.3:  | A movable power supply which can be recharged by solar energy and store hydrogen with metal hydrides [30].   | 11 |
| Figure 2.4:  | Toyota Mirai equipped with two high pressure tanks [37].   | 14 |
| Figure 2.5:  | Energy contents of different fuels [33].   | 15 |
| Figure 2.6:  | Liquefied hydrogen storage system [43].  | 18 |
| Figure 2.7:  | Schematic diagram of (a) cryogenic liquid hydrogen tank; (b) newly designed insulating supports [44].  | 18 |
| Figure 2.8:  | Liquid hydrogen storage system with magnetic levitation [41].  | 19 |
| Figure 2.9:  | Family tree of metal hydrides [52].  | 22 |
| Figure 2.10: | Pressure-composition isotherms for the hydrogenation of intermetallic compound are demonstrated. The left end of isotherm is solid solution called $\alpha$ -phase, and the right end of isotherm is $\beta$ -phase hydride. The region consisting of two different phases is designated. The Van't Hoff plot is shown on the right hand side. [11]. | 25 |
| Figure 2.11: | LaNi <sub>5</sub> with substitution of Ni by different elements with the effect on (a) cell volume and (b) equilibrium pressure [51].  | 25 |
| Figure 2.12: | The correlation between equilibrium pressure and unit cell volume of the first plateau and second plateau in Ti-V-Mn BCC alloys [53].  | 26 |
| Figure 3.1:  | Illustration of phase transformation of V-Ti-Cr alloys in a PCI curve at 25 °C, where the hydride transformed from BCC to FCC structure [14, 103].   | 32 |
| Figure 3.2:  | Schematic PCI curves of V-Ti-Cr alloys in the low-pressure   |    |

|              |  |    |
|--------------|--|----|
|              | range [95].....  | 33 |
| Figure 3.3:  | Correlation between Ti content and pressure plateau with different V contents: (a) $Ti_xV_yMn_{1.9-x}$ , (b) $Ti_xV_yMn_{1.7-x}$ [53].....   | 34 |
| Figure 3.4:  | Schematic trend of V content versus hysteresis factor in xV-Ti-Cr alloys [104]. ....   | 35 |
| Figure 3.5:  | PCI curves of pure vanadium and Ti-Cr-xV alloys at 323 K [104].....  | 36 |
| Figure 3.6:  | PCI curves of as-cast and heat-treated $Ti_{25}Cr_{35}V_{40}$ alloys [16].....   | 36 |
| Figure 3.7:  | PCI diagram of $V_{55}Ti_{22.5-x}Cr_{16.1+x}Fe_{6.4}$ alloys with different Cr quantities [15].....  | 37 |
| Figure 3.8:  | Cycle stability of $V_{60}Ti_{16}Cr_{24}$ and $V_{80}Ti_8Cr_{12}$ (Cr/Ti=1.5) [106].....   | 39 |
| Figure 3.9:  | Schematic view of cycle life for $V_{10}Ti_{40}Cr_{50}$ (sample 16) and $V_{26}Ti_{32.7}Cr_{25.9}Mn_{14.8}Mo_{0.6}$ alloy (sample 10) [18].....  | 39 |
| Figure 3.10: | Correlation between hydrogen desorption pressure and different proportion of V, Cr and Ti [106].....   | 42 |
| Figure 3.11: | Influence of temperature on the plateau pressure of $V_{75}Ti_5Cr_{20}$ alloys [106].....  | 42 |
| Figure 3.12: | Relationship of composition, temperature and desorption pressure in V-Ti-Cr alloys. ....   | 43 |
| Figure 3.13: | Relationship of composition, temperature and absorption pressure in V-Ti-Cr alloys. ....   | 44 |
| Figure 3.14: | Three characterized parts of as-cast $V_{80}Ti_8Cr_{12}$ alloy. ....   | 50 |
| Figure 3.15: | EDS patterns of (a) Part 1, (b) Part 2, (c) Part 3 of as-cast $V_{80}Ti_8Cr_{12}$ alloy with 2000 times of magnifications. ....  | 51 |
| Figure 3.16: | SEM images of $V_{80}Ti_8Cr_{12}$ alloys with different particle size: (a) 5 mm, (b) 2 mm, (c) 300-500 $\mu m$ , (d) 100-300 $\mu m$ , (e) <100 $\mu m$ , (f) 5 mm alloy after 500 cycles..... | 53 |
| Figure 3.17: | XRD patterns of $V_{80}Ti_8Cr_{12}$ alloy with different particle sizes.....   | 55 |
| Figure 3.18: | Correlation between lattice constants and particle sizes of $V_{80}Ti_8Cr_{12}$ alloys.....  | 56 |
| Figure 3.19: | Absorption kinetics for the $V_{80}Ti_8Cr_{12}$ alloy with different   |    |

|              |   |     |
|--------------|---|-----|
|              | particle sizes. ....  | 59  |
| Figure 3.20: | Pressure-Composition-Isotherm (PCI) graph for the $V_{80}Ti_8Cr_{12}$ alloy with different particle sizes. ....   | 62  |
| Figure 3.21: | Correlation between lattice parameters and usable capacity of $V_{80}Ti_8Cr_{12}$ alloy with different particle sizes. ....   | 62  |
| Figure 3.22: | Usable hydrogen storage capacity of $V_{80}Ti_8Cr_{12}$ alloy with different particle sizes within 30 cycles ....   | 63  |
| Figure 3.23: | Durability test for $V_{80}Ti_8Cr_{12}$ alloy with 5 mm particle size. ....   | 64  |
| Figure 3.24: | Desorption rates of $V_{80}Ti_8Cr_{12}$ alloy with different particle sizes at 2 <sup>nd</sup> cycle. ....  | 66  |
| Figure 3.25: | Desorption rates of $V_{80}Ti_8Cr_{12}$ alloy with various particle sizes at 30 <sup>th</sup> cycle. ....   | 67  |
| Figure 3.26: | Full desorption time of $V_{80}Ti_8Cr_{12}$ alloy with different particle sizes at 2 <sup>nd</sup> and 30 <sup>th</sup> cycle. ....   | 67  |
| Figure 3.27: | Desorption kinetics of $V_{80}Ti_8Cr_{12}$ alloy with 5 mm of particle sizes at 2 <sup>nd</sup> and 500 <sup>th</sup> cycle. ....   | 68  |
| Figure 4.1:  | SEM images of (a) pure melamine and (b-r) hydrothermally treated melamine cyanurate under different synthesis conditions. ....  | 90  |
| Figure 4.2:  | SEM images of melamine cyanurate treated hydrothermally with the autoclave which has (a) 100 mL of volume, (b) the reduced volume from 100 mL to 70 mL and (c) 100mL of volume but horizontally placed in an oven. .... | 91  |
| Figure 4.3:  | XRD patterns of (a) pure melamine and (b-r) hydrothermal treated melamine. ....   | 92  |
| Figure 4.4:  | FT-IR spectrum of pure melamine and hydrothermally treated melamine. ....   | 93  |
| Figure 4.5:  | SEM images of $C_3N_4$ prepared at different pyrolysis conditions corresponding to Table 4.6. ....  | 101 |
| Figure 4.6:  | SEM images of selected $C_3N_4$ materials: (a) Bulk g- $C_3N_4$ ; (b) $H_{200}-C_{560}-C_3N_4$ ; (c) $H_{205}-C_{560}-C_3N_4$ ; (d) $H_{205}-C_{600}-C_3N_4$ . ....   | 103 |
| Figure 4.7:  | TEM images of $H_{205}-C_{560}-C_3N_4$ : (a) microtube; (b) nanotube. ....  | 104 |

|              |  |     |
|--------------|--|-----|
| Figure 5.1:  | EDS images of selected $C_3N_4$ materials: (a) Bulk g- $C_3N_4$ ; (b) $H_{200}-C_{560}-C_3N_4$ ; (c) $H_{205}-C_{560}-C_3N_4$ ; (d) $H_{205}-C_{600}-C_3N_4$ ..... | 110 |
| Figure 5.2:  | Nitrogen adsorption-desorption isotherms of selected $C_3N_4$ materials at 77 K. ....  | 113 |
| Figure 5.3:  | Pore size distribution of selected $C_3N_4$ materials.....   | 113 |
| Figure 5.4:  | XRD of selected $C_3N_4$ materials: (a) Bulk g- $C_3N_4$ ; (b) $H_{200}-C_{560}-C_3N_4$ ; (c) $H_{205}-C_{560}-C_3N_4$ ; (d) $H_{205}-C_{600}-C_3N_4$ .....        | 115 |
| Figure 5.5:  | FT-IR of selected $C_3N_4$ materials: (a) Bulk g- $C_3N_4$ ; (b) $H_{200}-C_{560}-C_3N_4$ ; (c) $H_{205}-C_{560}-C_3N_4$ ; (d) $H_{205}-C_{600}-C_3N_4$ .....      | 116 |
| Figure 5.6:  | Pressure-composition-isotherms for the hydrogen absorption capacities of selected $C_3N_4$ materials at 20 °C.....   | 118 |
| Figure 5.7:  | Correlation between surface area and $H_2$ uptake of selected $C_3N_4$ materials. ....   | 118 |
| Figure 5.8:  | Estimation of hydrogen storage capacity of $H_{205}-C_{560}-C_3N_4$ up to 10 MPa. ....   | 119 |
| Figure 5.9:  | Pressure-composition-isotherms of $H_{205}-C_{560}-C_3N_4$ at 0, 20, 50 and 100 °C.....  | 120 |
| Figure 5.10: | Chemisorption measurements of $H_{205}-C_{560}-C_3N_4$ from 20 °C to 500 °C, where the sample was pre-charged with 10% $H_2+Ar$ gas at 20, 50 and 100 °C. ....     | 121 |
| Figure 5.11: | Absorption and desorption kinetics of $H_{205}-C_{560}-C_3N_4$ . ....  | 122 |

## List of Tables

|            |  |     |
|------------|--|-----|
| Table 1.1: | The requirements of stationary RAPS, MPS and automotive system.....                                | 4   |
| Table 3.1: | Composition analysis of as-received $V_{80}Ti_{18}Cr_{12}$ alloy by ICP-OES.....                   | 49  |
| Table 3.2: | Results of phase identification of $V_{80}Ti_{18}Cr_{12}$ alloy with different particle sizes..... | 56  |
| Table 4.1: | Reaction enthalpy of given hydrogen storage alloys at 298 K. ....                                  | 74  |
| Table 4.2: | Experimental parameters and yields of product in hydrothermal treatment. ....                      | 86  |
| Table 4.3: | Dimension of bar-like melamine cyanurate with different synthesis conditions. ....                 | 86  |
| Table 4.4: | Calcination conditions for pure melamine and as-made melamine cyanurate. ....                      | 96  |
| Table 4.5: | Calcination conditions for ground melamine cyanurate. ....   | 97  |
| Table 4.6: | Pyrolysis conditions for $C_3N_4$ tubes preparation.....   | 100 |
| Table 5.1: | Composition distribution of selected $C_3N_4$ materials. ....                                      | 110 |
| Table 5.2: | BET surface area characteristics of carbon nitride materials.....                                  | 114 |

## List of Equations

|               |   |    |
|---------------|---|----|
| Equation 2.1: | Dissociative chemisorption.....           | 23 |
| Equation 2.2: | Electrochemical separation of water.....  | 23 |
| Equation 2.3: | Van't Hoff equation.....                  | 24 |
| Equation 4.1: | Binding energy for porous materials ..... | 72 |



# **Chapter 1 Introduction**

## **1.1 Background**

The delivery of electricity to remote areas, which are isolated from main power grids, is relatively cost-ineffective and energy consuming by erecting power transmission lines from central electricity plants. For example, Gray et al. [1] has stated that the expense of supplying electricity to remote areas that are away from the major cities in Australia would cost AUD \$1 million per kilometre. This is not economically viable as these areas are sparsely populated. In addition to the affordability of power-grid installation in the developing countries, the key reasons that prohibit the development of in even “not-so-remote” places are the frequent disruption in the supply of grid power, natural limitations and difficulties of regular maintenance. Therefore, it is indispensable to find a solution that can address the issue of energy insufficiency in remote areas. Generally, diesel generators are the primary sources to provide electricity to the facilities in suburban regions. Although the diesel generators driven by fossil fuels can offer convenient power supply, they are environmentally unfriendly and financially uncompetitive due to the prodigious greenhouse gas emission and the costly transportation of diesel fuels to remote areas.

To decrease the carbon discharge from combustion engines and addiction to fossil fuels in off-grid regions, a remote area power supply (RAPS) based on renewable energy could be a potential option to supplant power generators relying on fossil fuels. The aim of RAPS is to establish a system which can independently provide constant and reliable energy output using sustainable resources, such as solar, wind and hydro. Morton [2] reported that the present electricity demand in the whole world per year can be fulfilled

by solar radiation falling on the earth surface in an hour. However, up to now, the abundant solar resource is still hard to be completely converted into electrical energy because of the high construction cost and the unsatisfactory efficiency of the solar panels. In addition, the intermittent power supply caused by the unstable nature as well as the limited transferability of renewable energy hinder the popularization of green energy. Fortunately, in the past few decades, the development of advanced technologies and innovative materials has considerably enhanced the energy conversion efficiency, making solar energy competitive with fossil fuels. Nowadays, the major challenge is to store the excess energy during the energy production when the direct natural forces are available. The study published by Dell et al. [3] has revealed that energy storage plays a critical role in overcoming the bottleneck of sustainable energy supply. As a result, the exploration of dependable energy storage approaches definitely stands out a top priority in maximising the potential of these energy-generation technologies.

Batteries, including lead-acid, lithium-ion, nickel-base, redox flow and sodium sulphur, are common and straightforward ways to accumulate the electricity produced from renewable energy source. They respond rapidly to load change and have high energy storage efficiency. Furthermore, they are initially cost competitive. However, some issues have been reported with respect to batteries, such as unpredictable and short cycle life, self-discharge, temperature sensitivity, limited discharge capability, high maintenance cost, lower safety and environmental hazards. In comparison to batteries, an alternative is hydrogen storage. A much higher energy density per volume and per mass are realized with hydrogen than batteries. Even considering the efficiency penalty of using a fuel cell or gas burner instead of an induction stove, the densities remain well superior to those of battery system [4-6].

Some solar-hydrogen prototype systems have been disclosed to utilize hydrogen as an energy source [7-10]. However, these experimental models stored hydrogen in the form of gas whose gravimetric and volumetric densities are quite low. In addition, the safety issue should be taken into account as well. It is extremely hazardous to store and transport compressive hydrogen within canisters, which may explode in a dense populated district. Furthermore, compressing gaseous hydrogen into desired volume requires extra works and the process requires extra instruments such as compressors and special designed canisters to sustain the resulting high hydrogen pressure. Solid-state hydrogen storage, such as metal hydrides and chemical hydrides, is a viable solution for storing hydrogen in a compact form. The volumetric hydrogen capacity of metal hydride is around 4 times greater than the compressive hydrogen kept at ambient temperature and the pressure of 80 MPa [11]. However, the currently dominant and commercialized hydrogen storage alloys based on  $\text{LaNi}_5$  ( $\text{AB}_5$ ) system, have limited applications due to the soaring cost of the rare earth elements, which are the main constituent of this system. The relatively low hydrogen capacity (theoretically 1.6 wt%) is another factor that prompts the researches to investigate more affordable and advanced hydrogen storage materials. In this study, V-Ti-Cr BCC alloys and tubular carbon nitride materials have been selected as promising candidates for three different types of energy storage applications, according to different requirements of these applications. Based on their hydrogen storage characteristics and other properties, V-Ti-Cr BCC system was designed for stationary RAPS and Movable Power Supply (MPS) systems, and tubular carbon nitride material was aimed to meet the needs of automotive systems. While both materials have high theoretical hydrogen contents, but to date, neither of them achieves the requirements of these applications. In the present work, these two hydrogen storage media are discussed and studied to fulfil the requisites of RAPS, MPS and automotive systems.

## 1.2 Project Target

This project is targeted to develop suitable hydrogen storage materials to satisfy the requirements of three types of energy supply, RAPS, MPS and automotive system, as listed in the following Table 1.1. Since the requirements of MPS are stricter than that of RAPS, the hydrogen storage properties of V-Ti-Cr alloys designed for both applications are only compared with the demands of MPS system.

**Table 1.1:** The requirements of stationary RAPS, MPS and automotive system.

| Performance   | RAPS<br>[1]  | MPS<br>[12]   | Automotive<br>[13] |
|---|--|---|--------------------|
| Gravimetric H <sub>2</sub> capacity<br>(wt%) (Required H <sub>2</sub> quantity, kg) | >1   | 2 (1.2)   | 5.5 (5.6)          |
| Volumetric H <sub>2</sub> capacity<br>(g H <sub>2</sub> /L)                         | >15  | 40  | 40                 |
| Absorption temperature (°C)   | Ambient  | Ambient   | Ambient            |
| Desorption temperature (°C)   | Ambient  | 50  | Ambient            |
| Absorption pressure (MPa)   | 1  | 2   | 1.2                |
| Desorption pressure (MPa)   | 0.1  | 0.2   | 0.5                |
| Charging rate (min)   | Intermittent/continuous charging<br>over a few hours per day         |   | 3-5                |
| Discharging rate ((g/s)/kW)   | Daily or seasonal<br>variation                                       | 0.014   | 0.02               |
| Durability (cycle)  | Thousands of partial<br>absorption-desorption<br>sequences each year | >1500 (Most likely<br>deeply discharged every<br>cycle) |                    |

This research project consists of four stages. The first stage is to identify the applicable hydrogen carriers for the three energy storage systems. To meet the requirements enumerated in Table 1.1, V-Ti-Cr BCC alloys and tubular carbon nitride are selected as

the potential candidates. Therefore, the goal of the first step is to study the hydrogen storage characteristics of these two materials.

The theoretical hydrogen content of V-Ti-Cr based alloy approximates 3.85 wt% at ambient pressure and room temperature [14]. The cases with hydrogen capacity above 2.2 wt% have been reported [15-20]. Tubular carbon nitride is mainly employed in photocatalysis field; however, a theoretical hydrogen capacity of 5.45 wt% was predicted using first-principles calculations by Koh et al. [21]. Some works on hydrogen capacity of nitrogen-doped carbon nanotubes with low nitrogen content (1-5 at%) have been published [22-24], but to our best knowledge, there was no available literature on the hydrogen storage studies of tubular carbon nitride with high nitrogen content ( $> 40$  at%). The properties of both materials, including hydrogen absorption/desorption contents, thermodynamics, equilibrium pressure plateau, cycle life and kinetics, need to be further investigated. Thus, the aims of this stage can be briefed as the followings:

- A. To review the literature about the hydrogen storage in general and then the hydrogen storage characteristics of V-Ti-Cr based alloys and tubular carbon nitride.
- B. To spell out the detailed requirements of hydrogen storage requirements in different applications.
- C. To realize the effects of catalytic elements and substitution on the properties of the selected materials so as to determine the starting chemical composition.
- D. To decide the synthesis methods by investigating the correlation between the material preparation and the hydrogen storage capability; and to optimise the processing parameters.

- E. To identify the required instruments for sample characterization and understand how to interpret the collected data.

The second stage of this project is to prepare the designed materials and study their hydrogen storage properties. After the preliminary characterization, the chemical composition and physical structure of the materials are adjusted accordingly. The objective of this part is to improve the performance of V-Ti-Cr based alloys and tubular carbon nitride via compositional optimization and proper synthesis approaches. The objectives are described as below:

- A. To confirm the chemical composition of the as-made V-Ti-Cr based alloys and tubular carbon nitride.
- B. To measure the hydrogen storage performance of the starting materials and examine the effects of additives and substitution on the H<sub>2</sub> capacities.
- C. To identify the key points of enhancing hydrogen capacity by analysing preliminary outcomes, e.g., hydrogen uptake, micromorphology, chemical structure and crystal structure.
- D. To tune the compositions of materials and to optimize the synthesis procedure for improving the performance.
- E. To measure the hydrogen storage properties of the modified V-Ti-Cr based alloys and tubular carbon nitride.

In the third stage, the reaction mechanisms of V-Ti-Cr based alloys and tubular carbon nitride are expected to be discovered. In other words, this part tries to clarify the influence of composition change and physical morphology on the hydrogen storage properties. The targets of this stage are elucidated in the followings:

- A. To carry out a comprehensive examination on the specimens with various experimental parameters by using corresponding characterizations, such as SEM, EDS, XRD, BET and FTIR.
- B. To perform a data comparison between all the results, and compare the results with reported literature, thereby studying the mechanisms of hydrogen storage of these two materials.
- C. To work out a better solution to further ameliorate the hydrogen storage capacity.

The fourth stage is to repeat the three steps specified above. That is, the loop contains knowledge survey, experiment design, experiment operation, result analysis, and trouble shooting. The attempts in this stage are listed as below:

- A. To keep searching for useful information related to V-Ti-Cr based alloys and tubular carbon nitride. The knowledge is expected to apply to the improvement of the materials.
- B. To design and implement the experiments based on the updated information.
- C. To analyse the experiment results and try to find out the factors which affect the hydrogen storage features.
- D. To correct the experimental parameters or the synthesis procedure for a better performance by means of accumulated data and experience.

Based on the above objectives, this thesis is divided into six chapters accordingly. At the end of the thesis a summary has been given in Chapter 6, suggesting the future work to be performed in this field.

## **Chapter 2    Literature Review**

### **2.1      Framework of Remote Area Power Supply (RAPS) and Movable Power Supply (MPS)**

The expense for extending the electricity power grids to remote areas which are not in the scope of primary populated centre is really prohibitive. In order to provide sufficient available electricity in these distant regions, a self-sustainable building equipped with a renewable energy supply system may be a feasible solution. As shown in Figure 2.1, Gray et al. [1] have proposed a model of this system which harnesses solar energy as the major power input, coupling with electrolyzers to produce hydrogen, with metal hydride to store hydrogen and with fuel cells to supply electricity. The scale of this prototypical system can offer adequate electricity ranging from several hundred watts to industrial grade beyond hundreds of kilowatts. The concept has come to fruition in 2013 since an off-grid Sir Samuel Griffith Centre in Griffith University was completely constructed in Australia [25]. The building incorporates photovoltaic technologies and hydrogen storage materials to achieve self-sustainability. The similar concept was also demonstrated by Biemann et al. [4]. A self-sufficient living unit based on hydrogen energy was developed as shown in Figure 2.2. Another application of the solar-hydrogen technology was carried out on thermal storage systems [26, 27]. High-temperature metal hydrides with a high specific thermal capacity were exploited to accumulate the heat generated from sunlight. In addition to solar energy, the RAPS system can be charged by a variety of renewable resources, such as wind, hydro and geothermal energy. For example, Genc et al. [28] evaluated the potential of hydrogen production and the corresponding cost by utilising a



wind-power/hydrogen system in Pinarbasi-Kayseri, where wind power was harnessed as a primary energy source.

*Figure 2.1 has been removed due to Copyright restrictions*

**Figure 2.1:** Stand-alone remote area power supply with photovoltaic sources, which ensures the uninterrupted electricity output by hydrogen production from electrolysis, hydrogen storage, electricity supply via fuel cells [1].

*Figure 2.2 has been removed due to Copyright restrictions*

**Figure 2.2:** A self-powered living unit based on PV system. The roof was equipped with solar panels for energy generation [4].

A smaller and movable power supply (MPS) unit has been developed based on the fundamental idea of RAPS system, as displayed in Figure 2.3 [29, 30]. Similar to RAPS, this portable unit can as well harvest renewable energy by hydrogen evolution and storage, but the difference is the size of the portable system is manufactured as large as a trunk

which can be transported easily. The main merits of this technology over diesel generators are low thermal and acoustic signatures, light weight, low cost of maintenance, no dependence on petrol fuels and zero pollutant emissions. Since these traits are advantageous to the military use in battlefields, this project was funded by the Department of Defence's Capability Technology Demonstrator (CTD) program. In this project, RMIT university leads the design and fabrication of electrolyser and fuel cell systems, and University of New South Wales (UNSW) is responsible for the design and characterization of hydrogen storage materials.

Owing to the dimensional restriction of the portable unit and the different working pattern from RAPS, the hydrogen storage materials employed in this system should possess better capability than that for RAPS in every aspect, e.g., higher hydrogen content, flexibility to harsh operating conditions, faster kinetics and longer cycle life. The key challenge of this MPS system is the high gravimetric and volumetric hydrogen capacity required for transportable applications, where a reversible hydrogen uptake of 2 wt% or more is needed at 0.2-2 MPa of working pressure. By comparison, the hydrogen capacity of 1 wt% is enough for stationary RAPS. This suggests that a doubled hydrogen capacity is required for MPS system. Up to date, there is no appropriate solid-state metal hydride which can perfectly meet the requisites of this portable application. For instance, AB<sub>5</sub> type alloys, originated from LaNi<sub>5</sub>, have fast kinetics, reasonable working temperature and plateau pressure, and facile activation. However, the hydrogen capacity in mass % is relatively low (~1.4 wt%), which is suitable for RAPS, but not for MPS. Considering the restricted availability and growing price of rare earth metals, AB<sub>5</sub> type alloys may not be the top priority for MPS application. Compared to AB<sub>5</sub>-type alloys, AB<sub>2</sub> alloys, generally based on Ti and Zr, have higher overall hydrogen storage capacities (1.5-3 wt%) and rapid kinetics at the temperatures below 100 °C. However, their available hydrogen capacity

was decreased by a rather high absorption plateau pressure, where around 1 wt% of hydrogen uptake can be obtained at room temperature and 2 MPa [31]. In addition, they have some disadvantages, such as short cycle life, difficult activation and impurities vulnerability.

Hence, it is necessary to explore a proper hydrogen storage material which can satisfy the requirements of MPS system. Once a desirable material is successfully developed for MPS, it is promising to apply it to RAPS due to its superior hydrogen storage properties. In this project, V-Ti-Cr BCC solid solution alloy was chosen as the hydrogen carrier and its excellent performance demonstrates the unlimited future of this low signature, rechargeable and portable energy supply.

*Figure 2.3 has been removed due to Copyright restrictions*

**Figure 2.3:** A movable power supply which can be recharged by solar energy and store hydrogen with metal hydrides [30].

## **2.2 Framework of Hydrogen Storage in Automotive Field**

Global warming, air pollution and the run out of fossil fuel by the following several decades are the drivers to the use of renewable energy sources on automotive vehicles. Some Western European countries, as well as India, announced that within the next 20-30 years they will ban all cars with internal combustion engines, and pursue the vehicles driven by renewable energy. Mostly renewable energy vehicles were defined as the automotives powered by pure electricity, like the electric vehicles (EV) launched by Telsla Motors [32]. In fact, hybrid electric vehicles (HEV), plug-in hybrid electric vehicles (PHEV) and fuel cell electric vehicles (FCEV) are all in the scope of renewable energy vehicles. The main difference is that EV, HEV and PHEV are driven by the electricity which is directly supplied by rechargeable battery modules, but FCEV is powered by the electricity generated from hydrogen fuels. In the car market, it is generally believed that HEV and PHEV are the transition products from petrol vehicles converting to EV. Before EV technologies are fully developed or the infrastructures are widely established, these two types of vehicles could be the alternatives for the drivers. HEVs have a better fuel efficiency and accelerating performance than fuel vehicles by combining internal combustion engine with battery. However, its battery capacity is relatively low and there is no external charging port to recharge the battery. In contrast, the subsequently developed PHEVs not only have a higher battery capacity than HEVs, but have a charging port which allows the battery to be recharged by external power sources. This indicates the usage pattern of PHEVs seems more like EVs.

Although EVs can be driven by pure electricity without any gas emission, which is environmentally friendly, they have several drawbacks regarding the slow charging rate,

relatively short cruising distance, and self-discharge. FCEV may be a potential solution to the problems. Nowadays, many car manufacturers such as Honda, Toyota and Hyundai, are developing zero-emission fuel-cell cars to reduce the greenhouse gas emission. Hydrogen is used in the fuel cell and as an energy carrier it has high gravimetric energy density [33] and high energy efficiency [34]. However, the major hindrances to affordable fuel cell cars are the expensive hydrogen storage system and the infrastructure needed: there are presently two specially designed tanks in each fuel cell car to store total 5 kg of hydrogen under 70 MPa (Figure 2.4); and refuelling stations with still much higher pressure storage. Based on an annual production of 500,000 double-hydrogen tanks system, each hydrogen storage system is estimated to cost about US\$ 3,755, if 5 kg of hydrogen is to be stored inside the tanks [35]. At present, the cost of installing a single hydrogen refuelling station in Japan is about US\$ 3.7-4.7 million [36]. These present major potential safety hazards and an effective hydrogen storage technology is obviously needed.

*Figure 2.4 has been removed due to Copyright restrictions*

**Figure 2.4:** Toyota Mirai equipped with two high pressure tanks [37].

While there are many solid hydrogen storage systems available, not all of them are suitable for on-board systems. For example, alloys based on Li and Mg have a high hydrogen storage capability but the temperature for hydrogen release is too high to be used in the on-board system. AB<sub>5</sub> type alloys have moderate hydrogen storage properties with easy initial activation, low plateau pressure, low ambient working temperature, but the hydrogen capacity is too low (~1.4 wt%) to supply sufficient hydrogen. Chemical hydride systems have very high gravimetric hydrogen capacities but there is a lack of effective means of rehydrogenation. Other media may require very low temperatures for hydrogenation (metal organic frameworks and carbon nanotubes), which needs an extra cooling apparatus. In any case they are still in the research stage and, up to today, no reliable quantities of these materials have been adequately demonstrated as hydrogen storage materials. Here tubular carbon nitride (C<sub>3</sub>N<sub>4</sub>) is selected as a promising hydrogen storage medium to store hydrogen in solid form.

## 2.3 Hydrogen as an Energy Carrier

Hydrogen is the most plentiful and inexhaustible element in the universe [38]. Due to its abundance and high energy capacity compared to gasoline (Figure 2.5) [33, 39], hydrogen becomes an attractive candidate as the energy carrier for transportation and electricity generation. While hydrogen fuel possesses such great features as a promising energy supplier, hydrogen storage still remains an obstacle to the practicability of fuel cells. Mostly, hydrogen reacts with other chemical elements and exists as stable compounds in nature. For example, an enormous majority of hydrogen atoms is bonded to oxygen atoms to form water or hydroxides. To make use of hydrogen, these compounds have to undergo specific treatments to separate hydrogen from other chemical substances. After dissociation, hydrogen can be collected and stored in three different forms: (1) compressive gas, (2) low-temperature liquid, (3) solid state [40]. Each method has its unique characteristics for hydrogen storage. In this section, these three types of options are introduced respectively.

*Figure 2.5 has been removed due to Copyright restrictions*

**Figure 2.5:** Energy contents of different fuels [33].

### **2.3.1 Gaseous Hydrogen Storage**

Up to now, the most common way to store hydrogen with high purity is to compress it into steel cylinders. It is a very straightforward and easily-operated approach. However, the major uncertainty for gas-phase storage is the volatile nature of gaseous hydrogen, which gives rise to considerable safety concerns. First, to prevent explosion, a strict thermal management should be carried out during compression and operation. Hence, the pressurization of hydrogen gas must be executed under an anoxic environment and loaded by several stages. Second, the energy consumption for obtaining 80 MPa pressure requires about 2.21 kWh/kg [11], which causes a great expense, let alone the cost of maintaining the compressors. Third, because of the low physical density of hydrogen, gaseous hydrogen has a poor volumetric energy capacity which prohibits the feasibility of hydrogen economy. In order to store more hydrogen, the increase of the volumetric energy density will augment the pressure in the steel tank. In this way, it is significantly hazardous to employ such high-pressure energy carriers which is extremely sensitive to the ambient conditions. A slight impact or temperature variation may result in unexpected disasters. The cost and reliability pose main problems for the viability of compressive hydrogen gas.



### 2.3.2 Cryogenic Liquid Hydrogen Storage

Liquidized hydrogen possesses higher volumetric capacity ( $70.8 \text{ gH}_2/\text{L}$  at 20 K and 0.1 MPa) [41] than pressurized hydrogen gas ( $40.8 \text{ gH}_2/\text{L}$  at room temperature and 70 MPa) [37]. While it has attractive potential to offer sufficient energy output which is competitive with gasoline, liquid hydrogen has a serious demerit that it can only be liquefied at 20 K under atmospheric pressure. A great amount of energy is wasted to retain the ultra-low temperature for avoiding the evaporation, which is a reduction of energy efficiency. To stabilize hydrogen in a liquid form, an adiabatic environment is required to retard heat leakage into containers. Some advanced tank designs are able to lower the heat flow down to several watt per second, leading to a vast decrease in evaporation rate which is a few percent per day [42]. A double-wall structure is constructed in these hydrogen tanks to maintain cryogenic temperature. Figure 2.6 demonstrates the layout of liquid hydrogen storage systems [43].

Xu et al. [44] made a liquid hydrogen tank using a Multi Layer Insulation with an embedded spiral pipe and a Vapor-Cooled Shield (VCS) at high vacuum to reduce the heat input (Figure 2.7a). A newly designed point-contact insulating support structure was applied to minimize the heat leakage (Figure 2.7b). As per their results, more than 85 % of the heat leakage can be reduced by the novel insulation supports. The evaporation rate of liquefied hydrogen is decreased to 1.2 % per day. Recently, Mito et al. [41] developed a magnetically levitated liquid hydrogen storage device by using High Temperature Superconducting (HTS) coils (Figure 2.8). Basically, the heat leakage conducted by support structure can be reduced to zero due to the magnetic levitation. By this method, the evaporation of liquid hydrogen can be suppressed to 0.05 % per day.

*Figure 2.6 has been removed due to Copyright restrictions*

**Figure 2.6:** Liquefied hydrogen storage system [43].

*Figure 2.7 has been removed due to Copyright restrictions*

**Figure 2.7:** Schematic diagram of (a) cryogenic liquid hydrogen tank; (b) newly designed insulating supports [44].

*Figure 2.8 has been removed due to Copyright restrictions*

**Figure 2.8:** Liquid hydrogen storage system with magnetic levitation [41].

In spite of many efforts denoted into this technology, the performance is still far away from practical applications. The energy loss is still an impediment to long-term energy storage. In addition, a cryogenic cooler and a delicate storage structure are needed to produce and keep liquid hydrogen under low temperature. These requirements may limit its feasibility in self-sufficient and automotive systems. More investigations are expected to develop better thermal insulation approaches and liquefaction processes.

### 2.3.3 Solid-state Hydrogen Storage

The progress of solid-phase hydrogen storage is booming due to its safety and high volumetric energy density over gaseous and liquid hydrogen forms. Many researchers have attempted to develop new solid-state hydrogen storage media which can absorb and desorb hydrogen under atmospheric pressure and room temperature. These materials accumulate hydrogen mainly via physical adsorption (carbons) or chemical absorption (complex and chemical hydrides, and metals).

Physical adsorption has a better charging/discharging rate than chemical absorption because of the absence of strong chemical bonds. By contrast, chemisorption is capable to gather more hydrogen in the materials and form stable hydrides. However, the stability is a double-edged sword for the thermodynamic properties. That is, chemisorption requires extra energy input to liberate hydrogen [45].

Porous carbons are typical materials which have fantastic ability to physically adsorb gases. Due to this characteristic, intensive researches on carbon materials, including carbon nanotubes, graphite nanofibers and activated carbons, etc., have been extended to hydrogen storage. They have shown noticeable potentials to become promising hydrogen accumulators for automotive applications because of their light weight which results in very high gravimetric density. Dillon et al. [46] studied the hydrogen sorption behaviour of single-walled nanotubes (SWNTs) and found that SWNTs could store high contents of hydrogen by means of numerous micropores. However, the hydrogen capacities in carbon materials varied from 0.2 wt%~10 wt%, indicating the lack of reproducibility in different laboratories [47, 48]. In addition to the reproducibility, the temperature required for physisorption was very low (2.9 wt% at 77 K), and only minor hydrogen (0.5 wt%) could be stored at 298 K even under high pressure of 9 MPa [49]. In order to enhance the

hydrogen storage capacities of carbonaceous materials at room temperature, heterogeneous doping has been applied to create chemical bonding sites, leading to an increment of absorption heat. For example, the tubular carbon nitride selected in this present work is derived from carbon nanotubes doped by nitrogen atoms. More comprehensive literature review about hydrogen storage in carbons is elucidated in Chapter 4.

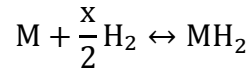
Generally, solid-state hydrides are categorized into three primary types: (1) complex metal hydrides, (2) chemical hydrides, (3) classical metal hydrides. Complex metals were firstly discovered by B. Bogdanovic and M. Schwickardi [50]. The reversibility of complex hydride such as  $\text{NaAlH}_4$  was developed via adding transition metal catalysts. While complex hydrides have superior gravimetric density, they still remain some critical problems, e.g. relatively high working temperature and pressure, low sorption rate, and inferior durability. Chemical hydrides, such as ammonia (15.1 wt%) and methanol (8.9 wt%), also possess excellent gravimetric capacities; however, chemical hydrides are generally irreversible and the reaction rate is rather sluggish [51]. In the present literature survey, classical metal hydrides are mainly discussed, including AB,  $\text{AB}_2$ ,  $\text{AB}_3$ ,  $\text{AB}_5$ ,  $\text{A}_2\text{B}$ ,  $\text{A}_2\text{B}_7$ , and solid-solution alloys, which are likely to become potential candidates in RAPS and MPS systems. Figure 2.9 shows the family tree of metal hydrides [52].

*Figure 2.9 has been removed due to Copyright restrictions*

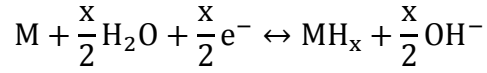
**Figure 2.9:** Family tree of metal hydrides [52].

Metal hydrides are the products from the chemical reaction between metal and hydrogen. The reasons that metal hydrides become such prospective are the safety as well as the high volumetric hydrogen capacity. For the former reason, metal hydrides form stable compounds by strong chemical bonds, which are far less perilous than explosive gaseous and cryogenic liquefied hydrogen. With respect to hydrogen capacity, metal hydrides own the hydrogen density of 6.5 H atoms/cm<sup>3</sup> for MgH<sub>2</sub> which is superior than hydrogen gas (0.99 H atoms/cm<sup>3</sup>) and liquid hydrogen (4.2 H atoms/cm<sup>3</sup>) [40]. Therefore, metal hydrides are more harmless and volume-advantageous to store hydrogen for hydrogen-fuelled applications. One possible pathway for the formation of metal hydrides is dissociative chemisorption; the other route is the electrochemical separation of water. These two reactions are shown as the following equations:

Equation 2.1: Dissociative chemisorption



Equation 2.2: Electrochemical separation of water



where M stands for the metal and x represents the value of valence.

Metal hydrides comprise matrix lattice of metals/alloys and hydrogen atoms. The thermodynamic properties of metal hydrides can be clearly illustrated by Pressure-Composition-Isotherms (PCI), where x-axis is the concentration of hydrogen and y-axis is the surrounding hydrogen pressure (Figure 2.10) [11]. Under a certain temperature, when high purity hydrogen gas is introduced into a container with hydrogen storage alloys loaded, the diatomic hydrogen molecules would dissociate into hydrogen atoms on the metal surface. Then the hydrogen atoms diffuse into the matrix and occupy the crystal lattices to form solid solution before the reaction with the metal atoms. This stage is usually referred as  $\alpha$ -phase. With the increase of hydrogen pressure in the vessel, more hydrogen atoms permeate over the material. In this stage, hydrogen atoms start to react with metal atoms, and  $\beta$ -phase hydrides are partially formed. The hydrogen pressure drops correspondingly and a plateau is observed in the isotherm owing to the coexistence of  $\alpha$  and  $\beta$ -phase. With the further formation of  $\beta$ -phase, the length of the plateau is extended, indicating the growth of usable hydrogen capacity. At the end of absorption, the solubility limit of hydrogen atoms in the metal is achieved. In this stage,  $\alpha$ -phase completely transforms to  $\beta$ -phase, the pressure increases sharply with the hydrogen concentration. The plateau pressure is a function of temperature in Van't Hoff equation, and is relevant to the difference of enthalpy ( $\Delta H$ ) and entropy ( $\Delta S$ ). Van't Hoff equation is shown as below:

Equation 2.3: Van't Hoff equation.

$$\ln\left(\frac{P_{eq}}{P_{eq}^0}\right) = \frac{\Delta H}{R} \cdot \frac{1}{T} - \frac{\Delta S}{R}$$

where  $P_{eq}$  and  $P_{eq}^0$  represent equilibrium pressure before and after hydrogenation, respectively. Because the change of entropy is mostly associated with the conversion from hydrogen molecules to solid solution, the standard value of  $\Delta S$  is around -130 J/K/mole  $H_2$  to all metal hydrides. The enthalpy change reflects the strength of the bond between metal and hydrogen. Given the equilibrium pressure of 0.1 MPa at 300 K, the value of  $\Delta H$  should be 39.2 kJ/mole  $H_2$  which is the heat generated from hydrogen absorption based on  $\Delta Q = T \cdot \Delta S$ , a derivation of Equation 2.3. To desorb hydrogen from hydrides, the same amount of heat needs to be supplied. For room-temperature operational metal hydrides, the heat can be provided by the ambience, but for high-temperature metal hydrides, such as  $MgH_2$ , the heat must be provided by external heat sources as the decomposition temperature of  $MgH_2$  is around 300 °C at 0.1 MPa. This may consume around 25 % of the energy produced from hydrogen [11].

The plateau pressure can be adjusted by heterogeneous element substitution due to the distortion of cell lattice. Figure 2.11 and Figure 2.12 illustrate that hydrogen storage alloys, such as  $AB_5$  [51] and Ti-V-Mn [53], have an inverse correlation between equilibrium pressure and lattice parameters .



*Figure 2.10 has been removed due to Copyright restrictions*

**Figure 2.10:** Pressure-composition isotherms for the hydrogenation of intermetallic compound are demonstrated. The left end of isotherm is solid solution called  $\alpha$ -phase, and the right end of isotherm is  $\beta$ -phase hydride. The region consisting of two different phases is designated. The Van't Hoff plot is shown on the right hand side. [11]

*Figure 2.11 has been removed due to Copyright restrictions*

**Figure 2.11:**  $\text{LaNi}_5$  with substitution of Ni by different elements with the effect on (a) cell volume and (b) equilibrium pressure [51].

*Figure 2.12 has been removed due to Copyright restrictions*

**Figure 2.12:** The correlation between equilibrium pressure and unit cell volume of the first plateau and second plateau in Ti–V–Mn BCC alloys [53].

### **AB<sub>5</sub> type alloys**

AB<sub>5</sub> alloys with CaCu<sub>5</sub> hexagonal structure are one of the most widely studied and well known hydrogen storage materials in both academic and industrial fields [54, 55]. This type of alloys, such as LaNi<sub>5</sub> and SmCo<sub>5</sub>, were firstly discovered in 1970 by Van Vucht et al. [56]. Many efforts have been dedicated to these alloys, especially LaNi<sub>5</sub> family, over the last 40 years as they are able to work at ambient pressure (around 0.3 MPa for major absorption and 0.1 MPa for desorption) and room temperature. The gas-solid reversible hydrogen capacity readily achieved 1.4 wt% by forming LaNi<sub>5</sub>H<sub>6</sub> [56] where H atoms prefer to occupy tetrahedral interstitial sites [55]. This gravimetric capacity is lower than that of ultrahigh-pressure gaseous and liquefied hydrogen, hence it is not enough for vehicle applications. Even so, it is still a promising candidate for stationary RAPS as the system weight is not a key concern.

To improve the performance of LaNi<sub>5</sub> alloy, researchers have started to alter the composition by elemental tuning. For example, rare earth metals, such as Nd, Pr, Ce, Ca

or Mm (misch metal, a cheaper mixture of La-rich rare earth metals), have been substituted or partially substituted for La at "A" site. The modification of lanthanum enhances the cycle life and also reduces the cost of raw materials [57]. Besides, nickel at "B" site can be replaced by various metals, including Al, Co, Cu, Fe, Sn, Mn and Ti, which serve as catalysts to lower the energy barrier and improve the hydrogen dissociation. Many studies have shown that these substitutions are able to ameliorate the alloy properties, such as hydrogen storage capacity and cycle stability [58-60]. In Ni-metal hydride (NiMH) battery application, better low-temperature working capability, high-rate discharging and lower equilibrium pressure were obtained by substitution [61-63]. Furthermore, the trend of inverse correlation between plateau pressure and cell volume allows people to adjust the operation pressure and temperature of the AB<sub>5</sub> alloy for matching their particular needs.

Because of the practical working condition, stable capacity, superior cycle life, higher tolerance of contamination, easy activation and flexibility of composition tuning, AB<sub>5</sub>-type alloy is selected as one of the hydrogen storage candidates for immovable RAPS application [1]. However, the relatively high cost of rare earth metals should be prudently taken into account.

## **AB<sub>2</sub> type alloys**

AB<sub>2</sub> alloys are typically derived from two sorts of Laves phase crystal systems: C14 (hexagonal) [64] and C15 (FCC) [65]. Among diversified AB<sub>2</sub> type alloys, the alloys based on Ti and Zr have better hydrogen storage performance and cost efficiency than AB<sub>5</sub> type alloys [52]. For instance, the maximum hydrogen storage capacity of (Ti<sub>0.65</sub>Zr<sub>0.35</sub>)<sub>1.1</sub>MnCr<sub>0.8</sub>Fe<sub>0.2</sub> alloy is about 2.2 wt% at 3.5 MPa and 32 °C [66]. The H<sub>2</sub> capacities of AB<sub>2</sub> alloys usually range from 1.5 to 3 wt% [67]. However, some BCC/C14 mixed phase alloys may suffer from the reduced hydrogen capacity which is trapped by the ultral-low desorption pressure plateau [68]. With regard to the cost, less amount of AB<sub>2</sub> alloys is required than that of AB<sub>5</sub> due to the higher hydrogen uptake, leading to a lower cost.

In order to tune the thermodynamic properties of AB<sub>2</sub> alloys, the elements at A and B sites can be replaced by various elements, which is analogous to AB<sub>5</sub> alloys [52]. For example, The Laves phase ZrCrMn alloys revealed an enhanced activation properties by substituting Zr by Sc [69]. Kumar et al. [70] found that the reversible hydrogen capacity of ZrMn<sub>2</sub> was improved by partially replacing Mn with Ni. In addition to elemental substitution, Wu et al. [71] prepared Zr(V<sub>0.95</sub>Ni<sub>0.05</sub>)<sub>2</sub>/MWCNTs composites by ball milling and reported that the kinetics, hydrogen capacity and thermodynamics of Zr(V<sub>0.95</sub>Ni<sub>0.05</sub>)<sub>2</sub> alloy were improved by the addition of multi-walled carbon nanotubes.

Although AB<sub>2</sub> alloys have higher hydrogen uptake, they are vulnerable to impurities, such as CO<sub>2</sub>, CO and O<sub>2</sub>. Hanada et al. [72] studied the CO<sub>2</sub> tolerance of Ti-Zr-Mn-Cr based alloys, and found that the additives of Fe and Co enhanced the CO<sub>2</sub> tolerance. On the other hand, Ni addition reduced the tolerance. In this case, the hydrogen purity plays a critical role on the cycle life of AB<sub>2</sub> type alloys.

## **AB<sub>3</sub> type alloys**

AB<sub>3</sub> alloys, generally based on CeNi<sub>3</sub> and PuNi<sub>3</sub>, have recently attracted much attention due to their interesting attributes of acting as a combination of long-developed AB<sub>5</sub> and AB<sub>2</sub> alloys. For instance, Dunlap et al. [73] indicated that the crystal structure of AB<sub>3</sub> alloys consisted of two third of AB<sub>2</sub> alloys and one third of AB<sub>5</sub> alloys with a long-range stacking arrangement. In addition to the crystal structure, PuNi<sub>3</sub>-type alloys, such as LaNi<sub>3</sub> and CaNi<sub>3</sub>, were investigated to have a higher hydrogen storage capacity (1.8 wt%) than AB<sub>5</sub> alloy and a better catalytic activity than AB<sub>2</sub> alloys [74]. Previous works done by Takeshita et al. [75, 76] also suggested that RT<sub>3</sub> alloys (R = Dy, Ho, Er, Tb, Gd; T = Fe or Co) had more surpassing hydrogen capacities than RCo<sub>5</sub> phase and the commercialized LaNi<sub>5</sub> alloys. Furthermore, Oesterreicher et al. [77, 78] reported that LaNi<sub>3</sub> and CaNi<sub>3</sub> alloys could absorb hydrogen rapidly at atmospheric conditions to form hydrides, LaNi<sub>3</sub>H<sub>5</sub> and CaNi<sub>3</sub>H<sub>4.6</sub>, while a significantly tilted pressure plateau of LaNi<sub>3</sub> was observed between 20-40 °C at 3.3 MPa [74].

Since AB<sub>3</sub> alloys contain both AB<sub>2</sub> and AB<sub>5</sub> units, they are expected to have high hydrogen storage capacities owing to the presence of AB<sub>2</sub> units, and enhanced kinetics and durability due to the existence of AB<sub>5</sub> units. Moreover, the special crystal structure of AB<sub>3</sub> phase enables the elements at A sites to be replaced by rare earths, Ca, Ti and Mg. For example, Kadir et al. [79-81] performed an investigation of crystal structure on RMg<sub>2</sub>Ni<sub>9</sub> (R = Ca, Y or rare earths) alloys, and the maximum reversible capacity of ~2 wt% was achieved by (Y<sub>0.5</sub>Ca<sub>0.5</sub>)(MgCa)Ni<sub>9</sub> at 263 K and 3.3 MPa. Lim et al. [82] studied the effect of partial substitution of both A and B sites by Ce and Al on the hydrogen storage properties of La<sub>(0.65-x)</sub>Ce<sub>x</sub>Ca<sub>1.03</sub>Mg<sub>1.32</sub>Ni<sub>(9-y)</sub>Al<sub>y</sub> alloys. The authors found that the reversibility of H<sub>2</sub> capacity was promoted, but the maximum capacity and kinetics were decreased by the additives. Xin et al. substituted Y for La in La<sub>(0.65-x)</sub>Y<sub>x</sub>Mg<sub>1.32</sub>Ca<sub>1.03</sub>Ni<sub>9</sub>

alloys and the results showed the Y substitution improved the available desorption capacity at 0.1 MPa below 80 °C.

As for the durability, the cycle life of AB<sub>3</sub> alloys is not remarkable enough for RAPS and MPS applications. According to Lim et al. [83, 84], the hydrogen capacity of La-Mg-Ni based alloys dropped by ~40 % after 500 cycles. However, the capacity retention could be enhanced by elemental substitution or composite method.

### **Other types of alloys**

Besides AB<sub>5</sub>, AB<sub>2</sub> and AB<sub>3</sub> alloys, other established hydrogen absorber alloys include AB, A<sub>2</sub>B, A<sub>2</sub>B<sub>7</sub> and solid solution. The typical AB type alloy is TiFe with a BCC CsCl crystal structure. This alloy is more weight- and cost-efficient than AB<sub>5</sub> alloys; however the major disadvantage is the difficult and slow activation [85, 86]. A<sub>2</sub>B alloys, such as Mg<sub>2</sub>Ni [87] and Ti<sub>2</sub>Ni [88], have hydrogen absorption content up to 3.6 wt% and 1.9 wt%, respectively. However, the impractically high reaction temperature (above 250 °C) of Mg<sub>2</sub>Ni limits its applications, and Ti<sub>2</sub>Ni is not a satisfactory hydrogen carrier because of the poor cycle stability and reversibility. A<sub>2</sub>B<sub>7</sub> alloys possess a super-stacking structure composed of AB<sub>5</sub> and AB<sub>2</sub> units, which has a different arrangement from AB<sub>3</sub> alloys [89]. Thus, A<sub>2</sub>B<sub>7</sub> alloys are always found to accompany with AB<sub>3</sub> phase [90]. A solid solution alloy based on V, Ti and Cr is selected as the potential candidates in the MPS application due to its high effective hydrogen capacity, rapid kinetics and long cycle life. More literature surveys are described in Chapter 3.

## Chapter 3 V-Ti-Cr based BCC Solid Solution

### 3.1 Introduction

One of the promising metal-based hydrogen storage materials is solid solution alloy mainly composed of vanadium, titanium and chromium, which are fused to form a BCC crystal structure. The alloy displays a high gravimetric hydrogen capacity and capability for the operation under ambient conditions, which makes it more suitable for on-land use. To achieve better performance, many researches have been studied on additive elements such as zinc, copper, nickel, cobalt, iron, manganese and zirconium. Other additives, including tungsten, hafnium, magnesium, yttrium, tantalum, molybdenum, boron, aluminium and rare earth elements, have been reported as well [15-20, 53, 91-101]. The amount of the modifiers can significantly affect the properties of V-Ti-Cr alloys. In these studies, substitution elements could improve the kinetics of the alloys. However, an excess of additives led to the deterioration of capacity and durability. Thus, in order to maintain the advantageous hydrogen capacity of the solid solution alloys, the sum of the addition elements is limited to 15 at% [14].

The most attractive characteristic of V-Ti-Cr BCC alloys is the high gravimetric energy density far superior to AB<sub>5</sub> and AB<sub>2</sub> commercial products. The theoretical H<sub>2</sub> capacity of this alloy group is about 3.85 wt%, but the reversible hydrogen capacity is only 1.8~2.4 wt% [15, 18-20, 91, 102]. The capacity loss mainly originates from four parts: (1) the hydrogen trapped in the BCC structure at room temperature, (2) broad hysteresis between absorption and desorption PCI curves, (3) the oblique equilibrium pressure, (4) relatively low dissociation pressure (below 0.1 MPa). These four parameters greatly influencing the hydrogen storage capacity of V-Ti-Cr alloys would be later discussed, respectively.

The V-Ti-Cr based alloys usually have two pressure plateaus in the pressure-composition isotherms, indicating two different phase regions. The first one is related to a solid solution hydride with BCC structure, where the octahedral sites are occupied by hydrogen. The second pressure plateau corresponds to a hydride with FCC structure, where hydrogen dwells in the tetrahedral vacancies, as shown in Figure 3.1. The less bonding number of hydrogen (four) in the tetrahedral sites gives rise to an instability of FCC hydride, allowing hydrogen to escape from the interstitial sites more easily compared to the octahedral sites in BCC hydride, where hydrogen atoms have eight bonding numbers [14, 103].

*Figure 3.1 has been removed due to Copyright restrictions*

**Figure 3.1:** Illustration of phase transformation of V-Ti-Cr alloys in a PCI curve at 25 °C, where the hydride transformed from BCC to FCC structure [14, 103].

Figure 3.1 reveals that the region of the BCC type hydride is below 0.1 psia, far lower than atmospheric pressure. The hydrogen trapped in this structure cannot be discharged unless the matrix alloy is heated above 250 °C, namely, the hydrogen residing in



octahedral sites is not available at ambient conditions. Generally, it is evaluated that about 1-1.3 wt% of hydrogen is irreversible under room temperature. The usable and reversible hydrogen at ambient temperature only exist in the FCC region, where the hydrogen atoms occupy the tetrahedral positions. In order to reduce the amount of hydrogen trapped in BCC interstitial sites, Okada et al. [95] studied the effect of vanadium content on the absorption behaviour at an ultra-low pressure. As illustrated in Figure 3.2, the stable vanadium mono-hydride ( $x=100$ ) at an extremely low pressure could be destabilized by the introduction of Ti and Cr, and commenced to become reversible in a dissociation pressure range. As the decrease of the vanadium content, the first plateau in the low-pressure region started to decline and disappeared, and the curve shifted to less protium concentration which permitted more hydrogen to be usable in ambient conditions.

*Figure 3.2 has been removed due to Copyright restrictions*

**Figure 3.2:** Schematic PCI curves of V-Ti-Cr alloys in the low-pressure range [95].

The hysteresis of V-Ti-Cr BCC solid solution alloys is relatively broad compared to that of AB<sub>5</sub>. This characteristic enormously affects the parameters of charging and discharging. On one hand, for the purpose of accumulating hydrogen under room temperature, the pressure of several MPa is required for hydrogen absorption, where extra pressurizers are necessary for compressing the gaseous hydrogen. On the other hand, the reversible hydrogen capacity may be reduced as the desorption pressure plateau is in the low pressure range. Thus, the extent of hysteresis should be minimized in order to absorb and liberate hydrogen at a close operation pressure. Nakamura et al. [53] studied the influence of composition change on the hysteresis for V-Ti-Mn hydrogen storage alloys, as depicted in Figure 3.3. The augmentation of Ti content or the reduction of Mn content decreased the hysteresis. Figure 3.4 shows the effect of V content on the hysteresis factor in xV-Ti-Cr alloys [104]. As the increment of vanadium, the hysteresis factor gradually rose and eventually kept stable. In addition, Aoki et al. [102] found that the milling treatment could effectively lower the hysteresis via the homogenization of the components and the refinement of the particle size.

*Figure 3.3 has been removed due to Copyright restrictions*

**Figure 3.3:** Correlation between Ti content and pressure plateau with different V contents: (a)  $\text{Ti}_x\text{V}_y\text{Mn}_{1.9-x}$ , (b)  $\text{Ti}_x\text{V}_y\text{Mn}_{1.7-x}$  [53]

*Figure 3.4 has been removed due to Copyright restrictions*

**Figure 3.4:** Schematic trend of V content versus hysteresis factor in xV-Ti-Cr alloys [104].

The flatness of the pressure plateau is an indication of the sorption stability for hydrogen storage materials. Oblique slopes of the equilibrium pressure at ambient conditions result in a significant loss of hydrogen capacity due to the need of high pressure charge or high vacuum discharge. Therefore, a flat pressure plateau could improve the stability and hydrogen capacity of V-Ti-Cr alloys. Generally, the V-rich solid solution alloys (above 50 at%) inherently have flatter equilibrium pressure than V-deficient alloys (Figure 3.5) [104]. For the alloys with vanadium content less than 50 at%, annealing treatment is a powerful method to flatten the pressure plateau. Akiba and Okada [16] discovered that  $\text{Ti}_{25}\text{Cr}_{35}\text{V}_{40}$  alloys with a heat treatment above 1573 K possessed flatter pressure plateau than as-cast parent alloys, as shown in Figure 3.6. Apart from heat treatment, some modifiers such as Al and Mn have been reported to ameliorate the flatness of V-Ti-Cr alloys [102].

*Figure 3.5 has been removed due to Copyright restrictions*

**Figure 3.5:** PCI curves of pure vanadium and Ti-Cr-xV alloys at 323 K [104].

*Figure 3.6 has been removed due to Copyright restrictions*

**Figure 3.6:** PCI curves of as-cast and heat-treated  $\text{Ti}_{25}\text{Cr}_{35}\text{V}_{40}$  alloys [16].

The relatively low dissociation pressure is one of the major drawbacks for V-Ti-Cr alloys. Similar to AB<sub>5</sub> type alloys, the adjustment of lattice constants can control the dissociation pressure, allowing desorption to take place at desired conditions. To change the lattice parameters, tuning of the chemical composition is a viable way. By reducing the Ti or V content and increasing the Cr content, the plateau pressure would be raised due to the shrinkage of the crystal lattice [15, 53, 95, 96, 102]. Figure 3.7 reveals the correlation between the quantity of Cr and the desorption pressure in V<sub>55</sub>Ti<sub>22.5-x</sub>Cr<sub>16.1+x</sub>Fe<sub>6.4</sub> alloys. As it can be seen, the dissociation pressure increased with the gain in Cr contents.

*Figure 3.7 has been removed due to Copyright restrictions*

**Figure 3.7:** PCI diagram of V<sub>55</sub>Ti<sub>22.5-x</sub>Cr<sub>16.1+x</sub>Fe<sub>6.4</sub> alloys with different Cr quantities [15].

Other properties such as durability and kinetics are also pretty critical to the applications based on V-Ti-Cr alloys. Generally, V-rich alloys are believed to have a better cycle life than V-scarce alloys [102, 105, 106]. For example, Kuriwa et al. [106] compared the cycle stability of two alloys with the same Cr/Ti ratio of 1.5, but with different V content of 60 at% and 80 at%, respectively (Figure 3.8). Obviously, the alloy with higher V content had a greater initial hydrogen uptake and capacity retention. However, an argument proposed by Young et al. [18] showed that the cycle life of low vanadium content (10 at%) alloys was superior than that with medium vanadium content (26 at%) alloys, as illustrated in Figure 3.9. The sample marked as 16 was  $V_{10}Ti_{40}Cr_{50}$  alloy which performed better durability than  $V_{26}Ti_{32.7}Cr_{25.9}Mn_{14.8}Mo_{0.6}$  alloy (sample 10). The increment in the ratio of Cr/Ti and the addition of other elements such as Al, Si and Fe could be the reasons to improve the cycle life of V-Ti-Cr alloys. Besides, the authors suggested that oxygen-free environment during alloy preparation was an efficacious approach for obtaining better sustainability. Fast kinetics can be achieved by quenching process which produces a finer grain size, and by annealing treatment which removes the voids in the materials [18].

*Figure 3.8 has been removed due to Copyright restrictions*

**Figure 3.8:** Cycle stability of  $V_{60}Ti_{16}Cr_{24}$  and  $V_{80}Ti_8Cr_{12}$  (Cr/Ti=1.5) [106].

*Figure 3.9 has been removed due to Copyright restrictions*

**Figure 3.9:** Schematic view of cycle life for  $V_{10}Ti_{40}Cr_{50}$  (sample 16) and  $V_{26}Ti_{32.7}Cr_{25.9}Mn_{14.8}Mo_{0.6}$  alloy (sample 10) [18].

Most of the current works for promoting the hydrogen storage properties of V-Ti-Cr alloys have concentrated on the chemical substitution. Only a few papers discussed about the influence of particle size on the  $H_2$  capacity of V-Ti-Cr alloys. Aoki et al. [102] suggested that the particle size of V-Ti-Cr alloys should be in the range from 0.1 mm to

10 mm. According to the statement, an immoderate reduction of the particle size for the alloy caused an increase of surface area, leading to the formation of oxide layers and the introduction of strain, which would decrease the hydrogen capacity. However, The explanations in this report were not distinct and the details were not specified. Luo et al. [107] studied the degradation behaviour of H<sub>2</sub>-embrittled V<sub>40</sub>(TiCr)<sub>51</sub>Fe<sub>8</sub>Mn alloy powder with particle size ranging from -60 to -400 mesh. It was found that the lattice micro-strain of V<sub>40</sub>(TiCr)<sub>51</sub>Fe<sub>8</sub>Mn alloy was lowered with the decrease of particle size, which led to a better hydrogen capacity and durability. Cho et al. [108] investigated the effect of ball milling and heat treatment on the microstructure and hydrogen storage performance of V<sub>25</sub>Ti<sub>32</sub>Cr<sub>43</sub> and V<sub>50</sub>Ti<sub>22</sub>Cr<sub>28</sub> alloys. The authors explored that the alloy after ball milled for 20 hours had a worse hydrogen capacity than the alloy without milling (particle size: 100-200 µm) due to the higher lattice strain induced by milling. Kwon et al. [109] compared the hydrogen capacities of V-Ti-Cr nano-powder synthesized by electric explosion of wire (EEW) and micro-powder made by mechanical grinding. The exploded sample was found to have inferior performance as the increase of surface area, resulting in a decreased interstitial sites. Up to date, the optimum particle treatment and particle size of V-Ti-Cr alloy have not yet been clearly determined. In the present work, V<sub>80</sub>Ti<sub>8</sub>Cr<sub>12</sub> alloys with different particle size from 7 mm to less than 100 µm would be studied regarding the hydrogen storage capacity, kinetics and cycle life. This research work is targeted to optimize the V<sub>80</sub>Ti<sub>8</sub>Cr<sub>12</sub> alloys with a suitable particle size to ultimately satisfy the requirements of MPS system.



## 3.2 Alloy Design

Itoh et al. have found that V-rich alloys have a better initial hydrogen capacity and durability than low V content alloys [105]. Kuriwa et al. also obtained the analogous results where the alloys containing 75 at% and 80 at% of vanadium possessed a higher capacity than 60 at% alloys by 0.6 wt%, and a longer service life (200-500 cycles) [106]. Moreover, the enhancement of durability caused by high content of V was discovered by Aoki et al. in a disclosed patent [102]. Therefore, the V-Ti-Cr alloys consisting of vanadium above 75 at% may be one of the promising alloys designs.

In addition to V contents, the ratio of Cr/Ti in this type of alloy plays a critical role in the performance. By tuning the ratio of Cr/Ti, the plateau pressure can be adjusted to a required range, 0.2 to 2 MPa, in MPS applications. Kuriwa et al. [106] concluded a schematic correlation between V, Cr/Ti and the desorption pressure under 273 K, which is exhibited in Figure 3.10. This can be a basic doctrine to optimize the composition. However, this diagram only shows the relationship at 273 K, which is not applicable in MPS system. The required discharging temperature in MPS is 323 K (50°C). Therefore, besides V contents and Cr/Ti, operation temperature should be taken into account. As revealed in Figure 3.11, similar to most of hydrogen storage alloys, higher temperatures raise the plateau pressure of V-Ti-Cr alloys. To determine the best composition for the suitable desorption pressure at 323 K (50°C), published data regarding the interaction between composition, temperature and desorption pressure were collected, organized and established in Figure 3.12 [94, 95, 104-106, 110-114]. As shown in this chart, the Cr/Ti ratio affects more significantly than V content on the desorption pressure. With an increment of Cr/Ti, the hydrogen desorption pressure increases dramatically. To liberate hydrogen at desired conditions, 0.2 MPa and 323 K, the desorption pressure plateau of

the alloy must be higher than 0.2 MPa. Thus, according to Figure 3.12, the value of Cr/Ti should be determined as equal to or higher than 1.5.

*Figure 3.10 has been removed due to Copyright restrictions*

**Figure 3.10:** Correlation between hydrogen desorption pressure and different proportion of V, Cr and Ti [106].

*Figure 3.11 has been removed due to Copyright restrictions*

**Figure 3.11:** Influence of temperature on the plateau pressure of  $V_{75}Ti_5Cr_{20}$  alloys [106].

*Figure 3.12 has been removed due to Copyright restrictions*

**Figure 3.12:** Relationship of composition, temperature and desorption pressure in V-Ti-Cr alloys.

Absorption pressure is also a key factor for the maximum hydrogen capacity in V-Ti-Cr alloys. However, as in Figure 3.13, the absorption pressure shows irregularity in the data collected from literatures due to its steep slope and insufficient experiment results [95, 104-106, 110, 112-117]. Although it is hard to precisely predict the absorption pressure, an approximate estimation should be achievable. Since the full scale of H<sub>2</sub> pressure that electrolyzers can supply is 2 MPa at room temperature, the absorption pressure plateau of V-Ti-Cr alloys must be lower than 2 MPa. In light of Figure 3.13, Cr/Ti=2 should be the top limit in order to control the absorption pressure within 2 MPa under 293 K (20 °C).

*Figure 3.13 has been removed due to Copyright restrictions*

**Figure 3.13:** Relationship of composition, temperature and absorption pressure in V-Ti-Cr alloys.

To ensure the rate of hydrogen discharge is fast enough to support the fuel cell in the MPS system, several researches were compared [18, 118, 119] and calculations were carried out to evaluate the desorption kinetics. It was found that, different from plateau pressure, kinetics of V-Ti-Cr alloy is greatly affected by V contents. The desorption rates of V<sub>75</sub> and V<sub>80</sub> alloys were worked out as 0.078 (gH<sub>2</sub>/s)/kW, and 0.058 (gH<sub>2</sub>/s)/kW., respectively. Both of them are higher than the requirement of kinetics, 0.014 (gH<sub>2</sub>/s)/kW, for the MPS application.

In conclusion, V-rich alloys have superior H<sub>2</sub> capacity and durability. To optimize the composition, the V content should be determined as 75 at% or 80 at%, together with Cr/Ti=1.5 or 2. The usable hydrogen capacity and cycle life are predicted to be around 2 wt% and several hundreds of cycles, respectively. The sorption pressure should be in the range of 0.2 MPa to 2 MPa, which is the operation standard for the MPS system. In this

work,  $V_{80}Ti_8Cr_{12}$  was chosen as the parent alloy for this application as it has a lower absorption pressure plateau at room temperature, leading to a higher storage capacity.

### **3.3 Materials and Experimental Procedure**

#### **3.3.1 Fabrication of Alloys**

The  $V_{80}Ti_8Cr_{12}$  alloys were prepared by arc melting under an Ar atmosphere to prevent serious oxidation. To improve the homogeneity and reduce the loss of alloying elements over casting, the melting process was repeated for two times. A combination of mechanical rolling, cutting and grinding was applied to control the size of the alloy. The dimension of as-cast  $V_{80}Ti_8Cr_{12}$  ingot was around 95 x 40 x 10 mm. In the process, the ingots were firstly rolled into 5-10 mm in thickness and then were crushed into lumps. The ingot fragments with 5 and 7 mm in three dimensions were selected as the samples ready for hydrogen storage and some of the fragments were further sectioned into 2 mm size. The rest of alloy pieces were crushed into particulates and then ground into fine powders. Following the pulverisation, the alloy powders with 3 ranges of particle size, 300-500  $\mu m$ , 100-300  $\mu m$ , and less than 100  $\mu m$ , were divided by stepwise sieving. Thus, in this study, the  $V_{80}Ti_8Cr_{12}$  alloy with six different sizes were obtained for hydrogen storage measurements and further characterizations.

### 3.3.2 Alloy Characterizations

The hydrogen storage and kinetics properties of the  $V_{80}Ti_8Cr_{12}$  alloys with different sample sizes were characterized using volumetric approach by Sievert instrument of which the accuracy was  $\pm 1.7\%$ . In the measurements, ultra-high purity hydrogen gas source (99.999 %) was applied to minimise the influence of impurities. In order to break down the oxide on the alloy surface and expose fresh surface to hydrogen environment, all the samples were firstly activated by heat treatment at 400 °C under vacuum for two hours and naturally cooled to room temperature. Following the activation, the samples were charged by 3.6 MPa of hydrogen at room temperature and the absorption kinetics was recorded. After the first hydrogenation, the samples were discharged under vacuum at 50 °C for one hour. This is to obtain a stable hydrogen capacity at desired conditions. That is, in this work, the hydrogen content which cannot be liberated at 50 °C is not taken into account as available capacity because the operation temperature in the MPS system is no more than 50 °C. In this case, to meet the working requirements of MPS application, the hydrogen absorption was carried out at room temperature and 2 MPa, and the desorption was performed at 50°C and 0.2 MPa. The hydrogen capacity within this limit is regarded as usable capacity.

Since the absorption rate is not a critical factor in this system (the electrolyser also takes time to build up the hydrogen pressure), except for the first cycle, the absorption behaviours of all the samples were measured based on the manner of pressure-composition-isotherm instead of kinetics tests. On the contrary, the desorption rate plays a significant role in this system to supply sufficient hydrogen gas to fuel cells within a short time. Thus, the desorption kinetics was recorded at 2<sup>nd</sup> and 30<sup>th</sup> cycle under 50 °C

with a starting pressure of 0.2 MPa which is the required pressure input for fuel cells. The desorption kinetics of the sample with 5 mm size was further investigated at 500<sup>th</sup> cycle.

Durability tests were accomplished by cyclically charging and discharging the V<sub>80</sub>Ti<sub>8</sub>Cr<sub>12</sub> alloys. In each cycle, the samples were charged with 2 MPa of hydrogen for 1 hour and discharged under vacuum for 1 hour. The usable hydrogen uptake of every sample was measured from 2<sup>nd</sup> to 30<sup>th</sup> cycle. To further study the performance of this alloy at higher cycle stage, the specimen with 5 mm size was selected to implement a long-term durability test for 500 cycles due to its highest hydrogen storage capacity among all the samples.

The composition of V<sub>80</sub>Ti<sub>8</sub>Cr<sub>12</sub> alloy was analysed by Inductively Coupled Plasma Optical Emission Spectroscopy (ICP-OES). The surface morphology and elemental distribution of the alloys were observed by using Hitachi 3400X scanning electron microscope (SEM) equipped with a secondary electron (SE) detector and an energy dispersive X-ray spectrometer (EDS). The lattice parameter and phase structure were investigated with a PANalytical Xpert Pro MPD X-ray diffractometer with Cu K $\alpha$  radiation at 45 kV and 40 mA. The analysis and refinement of the diffraction pattern were processed by using X'pert HighScore Plus software.



## 3.4 Alloy Composition, Morphology and Crystal Structure

### 3.4.1 Composition Analysis

The  $V_{80}Ti_8Cr_{12}$  alloy ingot was prepared by arc melting as described in Section 3.3.1. To ascertain that the chemical composition of  $V_{80}Ti_8Cr_{12}$  alloy is consistent with designed composition, Inductively Coupled Plasma Optical Emission Spectroscopy (ICP-OES) was applied to analyse the alloy. The composition results are tabulated in the following Table 3.1. The required  $V_{80}Ti_8Cr_{12}$  alloy should consist of 80.2 % of vanadium, 7.5 % of titanium and 12.3 % of chromium in weight percentage. In ICP-OES result, the as-received alloy have 79.3 wt% of vanadium, 7.4 wt% of titanium, 12.4 wt% of chromium and 0.09 wt% of iron, where Fe could be the impurity introduced by milling. If the iron impurity is excluded, the ratio of the elements turns out to be 80 wt% of vanadium, 7.5 wt% of titanium and 12.5 wt% of chromium, which is similar to the desired composition. The chemical difference is mainly in vanadium and chromium, where the variation is approximately 0.2 wt%.

**Table 3.1:** Composition analysis of as-received  $V_{80}Ti_8Cr_{12}$  alloy by ICP-OES.

|                                     | V (wt%) | Ti (wt%) | Cr (wt%) | Fe (wt%) |
|-------------------------------------|---------|----------|----------|----------|
| Desired alloy                       | 80.2    | 7.5      | 12.3     | 0        |
| As-received alloy                   | 79.3    | 7.4      | 12.4     | 0.09     |
| As-received alloy<br>(excluding Fe) | 80.0    | 7.5      | 12.5     | N/A      |

### 3.4.2 Element Distribution in Alloy Ingot

Scanning Electron Microscopy (SEM) and Energy Dispersive Spectrometer (EDS) were utilized to examine the homogeneity of  $V_{80}Ti_8Cr_{12}$  alloy. An as-cast ingot, of which the dimensions were 95 x 40 x 10 mm, was sectioned into several parts, and three of them were used as the subjects, as illustrated in Figure 3.14. The SEM coupled with EDS images with 2000 times of magnifications are shown in Figure 3.15 (a)-(c). The three major elements, vanadium, titanium and chromium, are well distributed in the matrix, indicating a homogenous solid solution phase.

*Figure 3.14 has been removed due to Copyright restrictions*

**Figure 3.14:** Three characterized parts of as-cast  $V_{80}Ti_8Cr_{12}$  alloy.

*Figure 3.15 has been removed due to Copyright restrictions*

**Figure 3.15:** EDS patterns of (a) Part 1, (b) Part 2, (c) Part 3 of as-cast  $V_{80}Ti_8Cr_{12}$  alloy with 2000 times of magnifications.

### 3.4.3 Morphology

The particle sizes of  $V_{80}Ti_8Cr_{12}$  samples were observed by SEM. Figure 3.16 (a) and (b) show the particle sizes of 5 mm and 2 mm samples, which were both embrittled by 30 cycles of hydrogen charge and discharge. Figure 3.16 (c)-(e) reveal the initial particle sizes of 300-500  $\mu m$ , 100-300  $\mu m$  and  $<100 \mu m$  samples, which were all pulverized by mechanical grinding. Figure 3.16 (f) displays the morphology of 5 mm sample subjected to 500 cycles.

As can be seen from Figure 3.16 (a) and (b), the particle size of 5 mm sample is smaller than that of 2 mm sample after 30 cycles, indicating a more difficult pulverization took place on 2 mm sample during hydrogen embrittlement. Both samples have dense cracks on the alloy surface, which allow hydrogen to diffuse into the internal matrices. Based on Figure 3.16 (c)-(e), sheet-like particle morphologies were observed for 300-500  $\mu m$ , 100-300  $\mu m$  and  $<100 \mu m$  samples. The particle size of 5 mm after 500 cycles (Figure 3.16f) was reduced to around 100-200  $\mu m$ , and similar to 5 mm and 2 mm samples, dense crack formed over the surface.

*Figure 3.16 has been removed due to Copyright restrictions*

**Figure 3.16:** SEM images of  $V_{80}Ti_8Cr_{12}$  alloys with different particle size: (a) 5 mm, (b) 2 mm, (c) 300-500  $\mu m$ , (d) 100-300  $\mu m$ , (e) <100  $\mu m$ , (f) 5 mm alloy after 500 cycles.

### 3.4.4 Phase Identification and Crystal Structure

The crystal structure and phase identification of  $V_{80}Ti_8Cr_{12}$  alloy with different particle sizes were studied by X-ray powder diffraction, as exhibited in Figure 3.17. Because the diffraction intensity for bulk samples is relatively weak, the alloy with powder form is required to obtain a higher intensity. To achieve this, prior to the X-ray scanning, the lumpish samples (5 mm and 2 mm) were pulverized by rehydrogenation at room temperature for 30 cycles. Following the pulverization, the samples were heat treated under vacuum at 400 °C for one hour to decompose the residual hydride. To avoid precipitate formation during cooling, the samples, which were loaded in a steel container for preventing contamination, were quenched to room temperature by water. After quenching, the samples were unloaded and then sieved by 500  $\mu m$  of mesh. The powder with particle size less than 500  $\mu m$  was collected and then measured by X-ray diffraction. To get rid of oxide, the samples with particle size of 300-500  $\mu m$ , 100-300  $\mu m$  and <100  $\mu m$  were all activated at 400 °C before X-ray diffraction measurement .

As can be seen in Figure 3.17, all of the samples have diffraction peaks corresponding to V-Ti-Cr BCC structure. In addition, the presence of vanadium oxide is observed in four of the samples except the 5 mm one. The oxide may hinder hydrogen from penetrating into the alloy, leading to a deterioration of the hydrogen uptake.

The refined crystal structure of  $V_{80}Ti_8Cr_{12}$  alloy with different particle sizes are presented in Table 3.2 and Figure 3.18. It is found that the lattice constants shrink with the reduction of particle size. The lattice parameters of 300-500  $\mu m$  and 100-300  $\mu m$  samples are similar as their particles sizes are not considerably different.

*Figure 3.17 has been removed due to Copyright restrictions*

**Figure 3.17:** XRD patterns of  $V_{80}Ti_8Cr_{12}$  alloy with different particle sizes.

The largest change of the lattice parameters between  $V_{80}Ti_8Cr_{12}$  samples is around 0.03%, which seems relatively small. This could be because the lattice contraction mostly occurred on the surface of alloy particles, leading to a small average lattice reduction. However, the lattice contraction on the surface could significantly restrict the hydrogen entry into the matrix. This inference could be further confirmed by Figure 3.16(a) and (b), where the particle size of 5 mm sample was smaller than that of 2 mm sample after 30 cycle rehydrogenation. In addition, large sheet-like alloy particles were found in 2 mm sample, indicating that the alloy surface was subjected to a severe distortion. Hence, the more mechanical treatments had been applied, the more the surface lattices were distorted, resulting in a difficulty for hydrogen diffusion.

**Table 3.2:** Results of phase identification of  $V_{80}Ti_8Cr_{12}$  alloy with different particle sizes.

*Table 3.2 has been removed due to Copyright restrictions*

*Figure 3.18 has been removed due to Copyright restrictions*

**Figure 3.18:** Correlation between lattice constants and particle sizes of  $V_{80}Ti_8Cr_{12}$  alloys.



## 3.5 Hydrogen Storage Properties

### 3.5.1 Absorption Kinetics

Figure 3.19 shows the absorption kinetics of  $V_{80}Ti_8Cr_{12}$  alloys with six different particle sizes, where all the samples were activated under 400 °C for 2 hours prior to the measurements at room temperature. As it can be seen, each kinetics curve consists of three steps of absorption as the reservoir volume of Sievert instrument was not large enough to fully charge the samples. This can be solved by applying a larger reservoir in the future. During the test, 3.6 MPa of  $H_2$  gas was introduced every 20 minutes to support the absorption, and the data points were dynamically recorded at intervals of one second. According to the kinetics curves plotted in Figure 3.19, the 7 mm sample gives very poor hydrogenation performance, which could be attributed to the insufficient reactive surface area and the difficult hydrogen diffusion into host alloys. To be fully activated, 7 mm sample might require multiple activation processes rather than one-off heat treatment to allow hydrogen to penetrate into the alloy lattices. The maximum hydrogen capacities of other five samples decline significantly with the reduction of sample size, suggesting that the mechanical cutting or milling may lead to a decrease of hydriding sites.

Despite the reduced total  $H_2$  capacities of the finely milled samples, higher absorption rate is achieved as the particle size decreases. This is believed that the refinement of alloy accelerates the hydrogenating reaction due to the enlarged surface area. Something of interest is that the 300-500  $\mu m$  and 100-300  $\mu m$  samples have a similar hydrogen storage capacity, but the latter has faster absorption kinetics. This indicates the milling process may create more hydriding routes because of higher surface area and hence the kinetics is improved. However, the overall amount of available hydriding sites is nearly the same

between these two samples, leading to a similar hydrogen uptake. The sample with particle size less than 100  $\mu\text{m}$  possesses the fastest absorption rate but the lowest hydrogen storage capacity, which is consistent with the previous trend. Compared to fine powder samples, the 5 mm and 2 mm specimens have 1-2 minutes of incubation time. After the incubation period, cracks form on the alloy surface owing to the lattice mismatch between alloys and hydrides, and hydrogen starts penetrating into the matrix. At this stage, the absorption rates become competitive with that of other mechanically pulverized samples.

To briefly summarize, mechanical pulverization leads to a deterioration of hydrogen storage capacity, which could be attributed to the formation of oxidation layer and residual strain over grinding process, which were confirmed by XRD. Luo et al. [107] reported a sluggish absorption rate was detected when a V-Ti-Cr based alloy was contaminated by extraneous gases such as carbon monoxide, oxygen and moisture. However, in this present study, all the samples reveal swift hydrogen absorption, indicating the small amount of vanadium oxide may not have a distinguishable impact upon the hydrogen storage performance. In this case, the residual strain may be the major determinant to the  $\text{H}_2$  capacity.

The absorption rates of milled samples are enhanced with the reduction of particle size. Surface area is believed to be the factor dominating this property. For the bulk samples (5 mm and 2 mm), their absorption rates, regardless of incubation period, are as good as the powder ones, supplying the cracks generated by hydrogen embrittlement also provide enormous surface area for hydriding reaction. When the sample size reaches 7 mm, which is expected to have less surface area, the hydrogenation is highly restrained because there are few pathways for hydrogen to diffuse into the alloy lattice.

*Figure 3.19 has been removed due to Copyright restrictions*

Figure 3.19: Absorption kinetics for the  $V_{80}Ti_8Cr_{12}$  alloy with different particle sizes.

### 3.5.2 Measurements for Usable Hydrogen Storage Capacity

Figure 3.20 shows the Pressure-Composition-Isotherm (PCI) curves for  $V_{80}Ti_8Cr_{12}$  alloys with different particle sizes. Before the characterization, all the samples were charged with 3.6 MPa of  $H_2$  at room temperature and then evacuated under vacuum at 50 °C to obtain an identical starting status for the following hydrogenation. This is to serve the real working conditions of the MPS system. Different from conventional PCI patterns, each curve in Figure 3.20 consists of two types of isotherms. The first isotherm is absorption at room temperature and the maximum gas pressure is 2 MPa, where the equilibrium pressure spots were recorded. The second isotherm is desorption at 50 °C and the ending pressure is 0.2 MPa, where the kinetics was recorded. Thus, the absorption isotherm can reflect the pressure plateau of the alloy, but the desorption isotherm can just give the total usable capacity supplied to fuel cells, and roughly reveal the lower limit of pressure plateau. The slight pressure increase between the last point of absorption and the first

point of desorption is because the samples were heated up from room temperature to 50 °C, leading to a volume expansion of hydrogen gas in a hermetic chamber. Furthermore, the elevated temperature made hydrogen atoms more active to escape out of the alloy, resulting in a partial dehydrogenation of hydride.

As shown in Figure 3.20, the absorption capacity is lowered with the decrease of the particle size, which is compatible with the observation in Figure 3.19. The result is similar with the P-C isotherm reported by Kwon et al. [109], where the authors stated that the interstitial sites for hydrogen accommodation are reduced due to the nanostructured particles and the augmented boundary area.

In addition to the absorption capacity, usable hydrogen capacity is a critical criterion to evaluate the feasibility of the alloy in the MPS system. Usable capacity represents the hydrogen amount which can be liberated at 50 °C until the chamber pressure is lower down to 0.2 MPa. This indicates a true capacity supplied to fuel cell systems. As depicted in Figure 3.21, the usable capacity declines with the reduction of particle size and lattice constants. The sample with 5 mm of particle size has the highest hydrogen uptake, 2.05 wt%, which achieves the MPS project target.

It is well known that the plateau pressure in P-C isotherm increases due to the contraction of interstitial sites in host hydrogen storage alloys [51, 53, 82, 109]. Because the maximum hydrogen pressure in the MPS system is limited to 2 MPa, the absorption capacity would be tremendously lowered if the alloy has a high plateau pressure induced by lattice shrinkage. Cho et al. [108] found that the hydrogen content of  $\text{Ti}_{0.22}\text{Cr}_{0.28}\text{V}_{0.5}$  and  $\text{Ti}_{0.32}\text{Cr}_{0.43}\text{V}_{0.25}$  alloys decreased with the increase of lattice strain after long-term ball milling, which supports our study. However, the result given by Luo et al. [107] showed that the hydrogen capacity of  $\text{H}_2$ -embrittled  $(\text{VFe})_{48}(\text{TiCrMn})_{52}$  alloy was improved by

the reduced particle size with lowered lattice strain. Although these two different pulverization methods provided opposite outcomes regarding lattice strain, one thing can be confirmed is that the lattice strain or lattice contraction are detrimental to the hydrogen capacity of V-Ti-Cr based alloys. As we can realise, while mechanical milling can efficiently break down alloy chunks, it may introduce severe strain into the lattice and probably some undesired impurities from grinding balls. A better way for minimising the lattice strain and securing a higher hydrogen uptake may be to pulverize the alloy by hydrogen embrittlement.

In this work, the crystal structures of  $V_{80}Ti_8Cr_{12}$  alloy pulverized by different means were investigated. The results confirm that the samples with fewer mechanical treatments have less cell contraction and hence possess a superior overall hydrogen storage performance to that of the samples subjected to more mechanical treatments.

*Figure 3.20 has been removed due to Copyright restrictions*

**Figure 3.20:** Pressure-Composition-Isotherm (PCI) graph for the  $V_{80}Ti_8Cr_{12}$  alloy with different particle sizes.

*Figure 3.21 has been removed due to Copyright restrictions*

**Figure 3.21:** Correlation between lattice parameters and usable capacity of  $V_{80}Ti_8Cr_{12}$  alloy with different particle sizes.

### 3.5.3 Cycle Stability

To confirm the reproducibility of the hydrogen capacities in Figure 3.20, the PCI measurement was repeated at 3<sup>rd</sup>, 4<sup>th</sup>, 5<sup>th</sup>, 10<sup>th</sup>, 20<sup>th</sup> and 30<sup>th</sup> cycles. The samples were evacuated at 50 °C under vacuum for 1 hour prior to PCI test to ensure the initial state of every measurement was the same. As shown in Figure 3.22, the usable hydrogen contents of all the samples within 30 cycles keep steady, indicating a good durability of V<sub>80</sub>Ti<sub>8</sub>Cr<sub>12</sub> alloy. Furthermore, the materials with particle size ranging from 300 to 500 µm and 100 to 300 µm have an analogous hydrogen uptake. The mechanical milling appears to have unnoticeable effects on the performance of these two samples.

*Figure 3.22 has been removed due to Copyright restrictions*

**Figure 3.22:** Usable hydrogen storage capacity of V<sub>80</sub>Ti<sub>8</sub>Cr<sub>12</sub> alloy with different particle sizes within 30 cycles .

Since V<sub>80</sub>Ti<sub>8</sub>Cr<sub>12</sub> alloy with 5 mm of particle size has been found to have predominant usable capacity among the specimens, it was selected to undergo a durability test for 500 cycles. As shown in Figure 3.23, the initial usable capacity between 0.2-2 MPa is 2.11

wt%. The capacity after 200 cycles, which is 2.01 wt%, can still meet the requirement of the MPS project. After 500 cycles, the available capacity decreases to 1.87wt%, which is around 89% of the initial capacity. The degeneration pattern is linear with 0.05 wt% per 100 cycles of dropping rate. This could be due to the accumulation of residual hydride, the formation of oxidation layer or the reduction of diffusion routes in fine powder.

The cycle test was performed at room temperature, except for 100<sup>th</sup>, 200<sup>th</sup>, 300<sup>th</sup> and other complete 100<sup>th</sup> cycles where the alloy absorbed H<sub>2</sub> at room temperature and desorbed H<sub>2</sub> at 50 °C. The results in actual working conditions are expected to be further improved as every desorption process in the MPS application is carried out at 50 °C, which helps to decompose more stable hydrides and thereby prolongs the cycle life. It is worth noting that the hydrogen capacity of 5 mm sample after 500 cycles is higher than that of 100-300 μm sample, while their particle sizes are similar, implying the mechanical milling indeed has negative effect on the H<sub>2</sub> capacity of V<sub>80</sub>Ti<sub>8</sub>Cr<sub>12</sub> alloys.

*Figure 3.23 has been removed due to Copyright restrictions*

**Figure 3.23:** Durability test for V<sub>80</sub>Ti<sub>8</sub>Cr<sub>12</sub> alloy with 5 mm particle size.



### 3.5.4 Desorption Kinetics

Apart from hydrogen storage capacity and cycle life, discharging rate is another crucial property to supply sufficient hydrogen to fuel cells in a desired period. Because the volume of the measuring system in Sievert-type instrument was not large enough to accommodate all the desorbed  $H_2$  gas, the desorption kinetics measurement was carried out in steps. This can be amended by replacing the reservoir with a larger one in the future. Each step of desorption started from 0.2 MPa and lasted for 20 minutes. The data points were recorded at intervals of one second, and the collected data were modified accordingly if the desorption pressure achieved equilibrium within 20 minutes. For example, when the desorption only took 15 minutes to reach equilibrium, the rest of 5 minutes of the data points were removed and not considered as valid desorption time. In this case, the rectified kinetics is able to demonstrate the desorption condition in the MPS system.

Figure 3.24 shows the desorption kinetics of  $V_{80}Ti_8Cr_{12}$  alloy with different particle sizes at 2<sup>nd</sup> cycle. Obviously the 5 mm sample has the highest desorption capacity and a reasonable desorption speed. The capacities of all the selected samples degrade as the particle size decreases, which is consistent with the previous results. However, there is no regularity in the rate of full desorption between various particle sizes. The fastest rate is given by the 2 mm sample, followed by the 5 mm and <100  $\mu m$  samples, while the 300-500  $\mu m$  and 100-300  $\mu m$  offer the slowest desorption rate.

*Figure 3.24 has been removed due to Copyright restrictions*

**Figure 3.24:** Desorption rates of  $V_{80}Ti_8Cr_{12}$  alloy with different particle sizes at 2<sup>nd</sup> cycle.

The desorption kinetics at 30<sup>th</sup> cycle were measured to investigate the storage performance of the alloy after recharging, as graphed in Figure 3.25. It is found that there is not much change in the desorption capacities, compared with the results in Figure 3.24, indicating a stable discharging property. The correlation between particle size and full desorption time at 30<sup>th</sup> cycle is shown in Figure 3.26. According to the outcomes, one may infer that, for the mechanically milled samples, the reduction of particle size can accelerate the desorption, but lower the  $H_2$  capacity. For the bulk samples (5 and 2 mm), the pulverization induced by hydrogen embrittlement can highly enhance the desorption without a significant drop of hydrogen capacity. Specifically, the 2 mm sample is superior to the 5 mm sample in desorption rate.

A calculation based on the data of 30<sup>th</sup> cycle shows that the hydrogen amount supplied by 5 mm, 2 mm, 300-500  $\mu m$ , 100-300  $\mu m$  and <100  $\mu m$  samples are 0.119, 0.118, 0.093, 0.089 and 0.092 (g/s)/kW, respectively. These are around 6-9 times faster than 0.014 (g/s)/kW which is required by the project. It is worth noting that in real conditions the

kinetics should be further faster as the desorption doesn't take place stepwise and there is no need to wait for equilibrium. Thus, the  $V_{80}Ti_8Cr_{12}$  alloy, regardless of the particle size, is proved to be capable to offer plenty hydrogen for the MPS system.

*Figure 3.25 has been removed due to Copyright restrictions*

**Figure 3.25:** Desorption rates of  $V_{80}Ti_8Cr_{12}$  alloy with various particle sizes at 30<sup>th</sup> cycle.

*Figure 3.26 has been removed due to Copyright restrictions*

**Figure 3.26:** Full desorption time of  $V_{80}Ti_8Cr_{12}$  alloy with different particle sizes at 2<sup>nd</sup> and 30<sup>th</sup> cycle.

The desorption kinetics of the 5 mm sample at 2<sup>nd</sup> and 500<sup>th</sup> cycle are compared in Figure 3.27. The desorption capacity after 500 cycles is around 10% lowered than the initial capacity. However, the desorption rate is enhanced from 0.129 (g/s)/kW to 0.167 (g/s)/kW after long-term cycling, which could be associated with the particle refinement induced by hydrogen embrittlement. This occurs because the alloy cells are subjected to volume expansion and lattice mismatch during hydrogenation. The hydrogen embrittlement keeps decreasing the particle size and exposing more fresh surfaces to hydrogen environment, hence the kinetics is improved because of the amplified surface area.

*Figure 3.27 has been removed due to Copyright restrictions*

**Figure 3.27:** Desorption kinetics of  $V_{80}Ti_8Cr_{12}$  alloy with 5 mm of particle sizes at 2<sup>nd</sup> and 500<sup>th</sup> cycle.

### 3.6 Conclusion

In this study,  $V_{80}Ti_8Cr_{12}$  alloy has been selected and designed as a potential hydrogen storage alloys to meet the requirements of the MPS system. The influence of particle size on the hydrogen storage properties of  $V_{80}Ti_8Cr_{12}$  alloy is investigated. The results show that the 7 mm sample cannot absorb hydrogen because of the insufficient surface area. Except for the 7 mm sample, the samples with particle sizes from 5 mm to less than 100  $\mu m$  have descending usable capacities as well as absorption capacities with the reduction of particle size. In addition to the capacities, the lattice constants are lowered as the decrease of particle size. A conclusion can be drawn accordingly that the more the lattice is distorted, the lower the effective hydrogen storage capacity is.

The absorption kinetics can be improved by reducing the particle size, though it is not a vital factor to MPS system. The desorption kinetics is basically enhanced with the decrease of particle size; however, the mechanically milled samples have more extended desorption time and lowered total desorption rate than  $H_2$ -embrittled samples. All of the  $V_{80}Ti_8Cr_{12}$  samples exhibit outstanding charge-discharge durability after 30 cycles. The 5 mm sample has only 10 % of capacity loss after 500 cycles.

In sum, the  $V_{80}Ti_8Cr_{12}$  alloy with 5 mm of particle size has around 2 wt% of usable hydrogen storage capacity under 20-50  $^{\circ}C$  and 0.2-2 MPa, which perfectly satisfies the capacity need of MPS application. Besides, the alloy is able to provide a rapid hydrogen supply rate which is 9 times faster than the requirement of MPS system. The alloy also has an excellent cycle life up to 500 cycles with a reasonable capacity retention. Therefore, the 5 mm  $V_{80}Ti_8Cr_{12}$  alloy shows a promising candidature for the hydrogen storage in MPS application.

# **Chapter 4    Synthesis of Tubular Carbon Nitrides**

## **4.1    Introduction**

Recently, nanostructural carbon materials have attracted a lot of attention to be an effective approach for the capture of greenhouse gases, such as CH<sub>4</sub>, CO<sub>2</sub> [120-124]. The characteristics of the high surface area and porosity make carbon-based materials capable to adsorb gases via physisorption. Since hydrogen is recognized as one of the most potential energy carriers, the feasibility of storing hydrogen in various carbon materials, including activated carbons, carbon nanofibers, and single/multi-walled carbon nanotubes, etc., has been widely studied [125]. In these porous materials, hydrogen molecules are physisorbed on the pore surface, and the hydrogen uptake is primarily affected by the operating temperature, working pressure, surface area and pore volume. Generally, owing to the low binding energy and weak van der Waals forces between hydrogen and solid surface, most of the reasonable adsorption capacities can only be achieved under cryogenic temperature (77 K) and high pressure, while the capacities tremendously decline to less than 1 wt% at room temperature [126]. Nevertheless, rapid kinetics and superior reversibility are offered due to the low interaction energy during physisorption. Since there is no phase transformation or lattice distortion induced by physical adsorption, the material durability over repeated hydrogen recharging can be considerably enhanced [127]. Despite the foregoing merits of physisorption, the cryogenic working temperature is still a hindrance to its practicability as a large amount of liquid nitrogen may be required to maintain the extremely low temperature. There is therefore a need to devote more efforts to improving the hydrogen capacity under ambient conditions. In addition to

temperature and pressure, pore attributes, such as surface area, pore volume and pore size, are the crucial factors in the hydrogen storage capacity of carbon-based materials. Adeniran et al. reported that activated carbon nanotubes with mesopore structure, higher surface area and pore volume had better hydrogen uptake at 77 K than that of the sample with micropores, lower surface area and pore volume [128].

Typically, it is an effective approach to improve the hydrogen storage content by tuning the pore structure to enlarge the surface area and pore volume [129, 130]. However, this could merely benefit the hydrogen capacity under cryogenic temperature and could have some limitations. Frost et al. [131] constructed Grand Canonical Monte Carlo (GCMC) simulations to investigate the influence of adsorption heat, surface area and free volume on the hydrogen uptake of metal-organic frameworks (MOFs), which is another porous material storing hydrogen majorly based on physisorption, under 77 K with different hydrogen loadings. The results gave three adsorption regions: the hydrogen capacity is associated with adsorption heat at low pressure, with surface area under intermediate pressure (up to 3 MPa), and with free volume at high pressure (12 MPa). The authors further studied the correlations at room temperature and found that the interdependence of each determinant at 77 K is not applicable at 298 K due to the poorer binding energy between H<sub>2</sub> and MOFs [132]. Suh et al. [133] collected plenty experimental data of MOFs and discovered that the hydrogen uptake of MOFs at 77 K and low pressure (0.1 MPa) is directly proportional to the surface areas ranging from 100 to 2000 m<sup>2</sup>/g, but is no more related to surface areas exceeding 2000 m<sup>2</sup>/g. This is because at low pressure hydrogen molecules will selectively attach on the sites having strong affinity with H<sub>2</sub> and hence are unable to reach a complete coverage on the surface areas above 2000 m<sup>2</sup>/g. At room temperature the material surface would be expected to have less coverage by hydrogen molecules than that under 77 K. Given a surface area beyond 2000 m<sup>2</sup>/g, a porous material

may have limited further improvement of hydrogen uptake which is gained from the surface area over 2000 m<sup>2</sup>/g.

It is believed that high surface area and pore volume are preferable to make hydrogen saturate active sites under high pressure and low temperature so as to enhance the H<sub>2</sub> storage capacity [126]. However, to store hydrogen at ambient conditions, a potential solution may be the strengthening of binding energy (adsorption enthalpy) between hydrogen and the surface of carbonaceous materials. For physisorption-based materials, the enthalpy is too low (4-10 kJ/mole) to stabilize hydrogen molecules on the surface at ambient temperature and pressure, and thus inferior hydrogen uptake can be envisaged. On the other hand, if the adsorption enthalpy is too high to easily release hydrogen, as in some cases of chemisorption, the exothermic reaction will be very severe and externally supplied energy is required to liberate hydrogen, leading to a sluggish kinetics and unfavourable reversibility. Suh et al. [133] had collected reported data regarding the correlations of hydrogen capacity against adsorption enthalpy of MOFs. The data indicated that at 77 K the H<sub>2</sub> storage contents were not markedly increased with the escalated adsorption enthalpy from 4 to 12 kJ/mole. In contrast, at 298 K and high pressure, it showed an uptrend of hydrogen uptake with the increment of adsorption heat. Hence it is indispensable to strengthen the binding energy of H<sub>2</sub> to allow porous materials to absorb/desorb hydrogen at ambient temperature for the sake of real applications.

According to the theoretical calculation done by Bhatia et al. [134], the optimum binding energy for porous materials could be obtained by Equation 4.1.

**Equation 4.1: Binding energy for porous materials**

$$\Delta H_{opt}^0 = T\Delta S^0 + \frac{RT}{2} \ln \left( \frac{P_1 P_2}{P_0^2} \right)$$



In Equation 4.1, the change of constant enthalpy  $\Delta H^\circ$  stands for the average or overall adsorption heat in the range of  $P_1$  and  $P_2$ , where  $P_1$  and  $P_2$  represent the equilibrium storage pressure and desorption pressure, respectively. The absolute value of  $\Delta H^\circ$  is determined as the isosteric heat at the selected temperature (T).  $\Delta S^\circ$  means the entropy change, generally equal to  $-8R$  for diversified adsorbents for the purpose of hydrogen adsorption, and it is associated with the standard pressure  $P_0$  (0.1 MPa).  $R$  is the ideal gas constant. To simulate the practical hydrogen adsorption,  $P_1$ ,  $P_2$  and  $T$  could be set as 0.15 MPa, 3 MPa and 298K, respectively. Then the optimum enthalpy change ( $\Delta H^\circ_{\text{opt}}$ ) = -15.1 kJ/mole can be derived from Equation 4.1 with the substitution of the parameters. Consequently, the binding enthalpy of 15.1 kJ/mole for porous hydrogen storage materials is favourable under 298 K between the pressure range of 0.15 MPa and 3 MPa. Some studies suggested that an ideal adsorption energy for a hydrogen storage application at ambient temperature is around 20-30 kJ/mole [135-137]. This can be supported by the experimental outcome performed by Muthukumar et al. [138], where the thermodynamic properties of several hydrogen storage alloys were analysed, as shown in Table 4.1. It is well known that La-based  $AB_5$  type and Ti-V-Cr-based alloys have the capability to store and release hydrogen under room temperature. As it is revealed in Table 4.1, the reaction enthalpies of these low-temperature alloys are between 20-50 kJ/mole, which is consistent with the ideal binding energy proposed in the aforementioned literatures.

**Table 4.1:** Reaction enthalpy of given hydrogen storage alloys at 298 K.

| Hydrogen storage alloys   | Absorption enthalpy<br>(kJ/mole H <sub>2</sub> ) | Desorption enthalpy<br>(kJ/mole H <sub>2</sub> ) |
|---|--|--|
| LaNi <sub>5</sub>   | -29.43   | 30.12  |
| LaNi <sub>4.7</sub> Al <sub>0.3</sub>   | -33.75   | 41.54  |
| LaNi <sub>4.91</sub> Sn <sub>0.15</sub>   | -29.96   | 32.23  |
| Ti <sub>0.99</sub> Zr <sub>0.01</sub> V <sub>0.43</sub> Fe <sub>0.09</sub> Cr <sub>0.05</sub> Mn <sub>1.5</sub> | -21.41   | 26.15  |
| MmCo <sub>0.72</sub> Al <sub>0.87</sub> Fe <sub>0.04</sub> Ni <sub>3.91</sub>                                   | -42.32   | 48.92  |

To increase the binding energy, a renowned approach is to incorporate or decorate carbon frameworks with heterogeneous elements, such transition metals, oxygen functional groups, boron and nitrogen. The additives of transition metals can induce a mechanism called “spillover” by which hydrogen dissociation and migration will take place in porous materials. The phenomenon of hydrogen spillover has been discovered for decades and studied a lot in catalysis scope. Many researchers gave extensive reports about spillover in miscellaneous catalysis [139-143]. In hydrogen storage fields, the earliest idea of spillover for the improvement of H<sub>2</sub> capacity was recorded in a patent done by Schwarz [144]. In this patent, the metal catalysts, Pt and Pd, were doped on activated carbon to generate spillover effect. Thereafter, comprehensive researches have been performed to investigate the hydrogen storage properties of different porous materials by applying the spillover concept. The doped materials include graphite [145-147], templated carbons [148], activated carbons [149-151], carbon fibres [152-155], carbon nanotubes [156-158], COFs [159], MOFs [160-162], metal oxide [163-165], silica [166-168] and polymer [169].

Hydrogen spillover can be divided into three major steps. First, the dissociation of molecular hydrogen occurs due to the catalysis induced by transition metals, such as Ru,

Pd, Pt and Ni, and then hydrogen atoms are created and bound to the surface of transition metals. Second, the dissociated hydrogen atoms migrate from metal catalysts onto the matrix materials. Third, the hydrogen atoms form chemical C-H bonds with matrix materials by surface diffusion [170]. The increased adsorption enthalpy, along with the formation of chemical bonding, is an attractive characteristic of hydrogen spillover to manipulate hydrogen storage devices at ambient temperature instead of unfavourable low temperature (77 K). However, it should be noted that molecular hydrogen was found to decompose swiftly on metal catalysts and diffuse sluggishly along the substrate materials [171]. Thus, more efforts are needed to enhance the charging kinetics. Pyle et al. [170] suggested that hexagonal carbons with high surface area could be the most promising candidates of which the  $\pi$ -conjugation is influenced by lattice dopants or oxygen functional groups.

In contrast with transition metals, the doping of oxygen functional groups, boron and nitrogen can change the electronic structure of carbon or provide active sites for chemical bonding with hydrogen. It is relatively facile to add oxygen groups to the surface of carbon materials as this modification can be achieved by several methods, such as direct synthesis, acid oxidation, anodic oxidation, ozone oxidation, gas-phase air and oxygen plasma. Schwarz et al. [172] studied the hydrogen adsorption properties of activated carbons oxidized by gas-phase approach. The adsorption test was carried out at 78 K and 4 MPa, and the result showed the hydrogen capacity was improved with the increment of oxygen content as well as the surface acidity. A similar result was obtained by Comisso et al. [173] who measured the H<sub>2</sub> capacity of carbon nano-horns subjected to thermal oxidation and they found that the hydrogen capacity at 77 K was increased due to the enlarged surface area and pore volume. Wang et al. [174] utilized oxygen plasma to generate oxygen functional groups mainly in the form of semiquinone (C=O) while most

of the functional groups produced by air oxidation were hydroxyl (C-OH). After this treatment, the hydrogen uptake of Pt-doped templated carbon at 298 K under 10 MPa was enhanced from 1.17 wt % (pristine sample) to 1.74 wt % (treated by oxygen plasma).

Due to the small atomic size of carbon, the carbon atoms in graphite materials are arranged in a compact lattice structure with a bond length of 1.42 Å. Since boron and nitrogen atoms have similar size as carbon, the substitution of B and N for C atom is able to change the electronic properties of host materials without a significant alteration to its lattice structure. However, the altered electronic structure can bring about different adsorption behaviours and hence influence the hydrogen storage capacity. For example, Jeong et al. [175] investigated the hydrogen storage performance of boron-doped super-activated carbons which were synthesized from the polycondensation between phenyl diacetylene and BCl<sub>3</sub>. The hydrogen capacities of a BC<sub>6</sub> product were enhanced to be 3.5 wt% and 0.5 wt% per 500 m<sup>2</sup>/g of surface area at 77 K and 293 K, respectively, with the pressure below 10 MPa. These values were over three times better than the capacities in other corresponding carbon-based materials. This could be attributed to the increased adsorption energy, 10-20 kJ/mole, which is induced by the electron deficiency of an out-of-planar boron moiety. While the surface area was decreased by boron doping, the hydrogen uptake was improved due to the high binding energy. Ariharan et al. [176] obtained an analogous result by preparing boron substituted carbons with resorcinol and triethylborate as carbon and boron sources, respectively. The hydrogen storage capacity at 298 K and 10 MPa pressure was remarkably enhanced by the introduction of boron heteroatom into carbon materials. More theoretical and experimental reports are the supportive evidence to the mechanism [177-181].

Nitrogen doping in carbons has great impact on the hydrogen storage capacity, which has been confirmed by computational and experimental studies. The effects of nitrogen substitution on hydrogen adsorption for various carbonaceous materials, such as activated carbons [182], microporous carbons [183-187], templated carbons [188-192], graphite [193, 194], graphene [195-205], carbon nanotubes [23, 24, 206, 207], carbon xerogel [208], carbon spheres [209], have been comprehensively investigated. Among these nitrogen-containing carbons, the highest hydrogen uptake at room temperature was achieved as 4.3 wt% under 4 MPa on N-doped graphene with decorated palladium nanoparticle [201].

Current studies show that doped nitrogen has several benefits to the hydrogen storage properties of carbon materials, as outlined in the followings. First, it can increase the binding energy between hydrogen and carbon frameworks by electronic modification or polarization [183, 184, 190, 194, 201, 208]. For instance, Jiang et al. [209] synthesized nitrogen-doped hollow carbon spheres via template method and found that the hydrogen capacity could reach 2.21 wt% under 298 K at 8 MPa. The nitrogen atoms doped in carbon spheres improved the adsorption heat up to 21.7 kJ/mole, which has fallen in the suitable range for operating hydrogen sorption at ambient conditions. The N-doping also generated more reaction sites to chemically absorb hydrogen, leading to a possible combined reaction of physisorption and chemisorption. Second, the theoretical calculation performed by Sankaran et al. [206] indicated that nitrogen atoms could be the activation centres initiating hydrogen adsorption/absorption due to the decreased dissociation energy of hydrogen molecules and the preferable formation of N–H bond over C–H bond. Similar calculation result done by Zhang et al. [207] also suggested nitrogen substitution enhanced the hydrogen dissociation and adsorption on CNTs. Third, Badzian et al. [193] claimed that graphitic carbons containing 1 at% of nitrogen had 0.7-

0.8 wt% of hydrogen content at room temperature under 7 MPa. This could be ascribed to the implantation of nitrogen atoms into graphite, which creates binding sites for the adsorption of hydrogen molecules. Fourth, nitrogen doping can strengthen the adhesion between transition metals/catalysts and support carbon materials, and hence facilitate the spillover effect [190, 195, 196, 198, 203, 205]. Kong et al. [185] attributed this phenomenon to the elevated electrostatic attraction between the interface. By DFT calculation, Lee et al. [200] found that a well distribution of lithium atoms on two types of graphene layers was obtained without aggregation because the bonding of Li to these N-doped graphene sheets is stronger than that between the bulk Li. This could also enhance the spillover effect.

Although nitrogen substitution is beneficial to the room-temperature hydrogen storage of carbon networks, under cryogenic temperature (77 K), the N-doping is less effective than the enhanced surface area and pore volume [187-189]. Some reports exhibited that, under 77 K, the nitrogen incorporation could be advantageous to hydrogen storage at low hydrogen uptake (low hydrogen coverage) but be unfavourable at high hydrogen uptake (high hydrogen coverage) because of the reduced adsorption heat with the growing hydrogen capacity [24, 187, 189].

Due to the merits brought by nitrogen doping, another type of N-rich carbonaceous materials, so-called carbon nitride, has been intensively studied for hydrogen storage applications. Various configurations of carbon nitride, including graphitic [210-218], mesoporous [219], film [220-222], nanobell [223] and nanotube [21, 224, 225] carbon nitride, have been theoretically and experimentally investigated. Among these studies, the highest hydrogen uptake explored by experiments reached 8 wt% at 573 K and 0.1

MPa on carbon nitride nanobells, which was reported by Bai et al. [223]. However, this has not yet been ascertained by other literature.

Up to date, few experimental researches regarding hydrogen storage properties on carbon nitride nanotubes have been reported. Most of the studies focus on theoretical calculations. Koh et al. [21] performed first-principles calculations using density functional theory to examine the hydrogen uptake of graphitic carbon nitride nanotubes. The authors stated that the well-distributed pores on carbon nitride nanotube walls enable hydrogen to easily diffuse into/out of the nanotube interior, and the substituted nitrogen atoms at the edges of pores offer reaction sites for both chemical and physical sorption of hydrogen. The calculations predicted that a single nanotube and a bundle of nanotubes can store 4.66 wt% and 5.45 wt% of hydrogen amount respectively by simultaneous chemisorption and physisorption. The average overall adsorption energy was proposed to be around 0.29 eV per H atom (27.98 kJ/mole) as a function of tube diameter ranging from 9.5 to 18 Å. This moderate adsorption heat allows the nanotubes to work under room temperature. The theoretical findings disclosed a possibility that graphitic carbon nitride nanotubes could be a potential hydrogen storage medium due to its fast kinetics, high capacity and excellent operating capability at ambient conditions. Hence, in our work, tubular carbon nitride was synthesized and its hydrogen storage performance was studied via systematic experiments.

Except for hydrogen storage, carbon nitride nanotubes have been developed in diversified applications, such as photocatalyst (hydrogen production and photocatalytic degradation) [226-230], electrochemical transducer [231], electrooxidation [232, 233], field emission device [234-236], nanoparticle or catalyst supporter [237-240], photoluminescence [241, 242], lithium batteries [243] and solar cells [244]. However, many synthesis approaches

required sophisticated facilities (chemical vapor deposition and sputtering), catalysts, substrates/templates, strong acid/base, toxic solvent, etc. These requirements may lead to complex and costly production processes which are not applicable for commercialization. In order to simplify the production, reduce the harm upon the environment and increase the yield of carbon nitride nanotubes, syntheses without the employment of templates and hazardous chemicals have been intensively studied in the past five years. The methods include simple reaction between chemical mixtures [245-252] and the curliness of carbon nitride nanosheets [244, 253-256]. In our study, an environmentally friendly synthesis approach based on the condensation of sole melamine using hydrothermal treatment and calcination was applied to produce tubular carbon nitride. Similar methods were reported by some research groups for photocatalysis [257-260]. However, the carbon nitride tubes shown in those reports were somewhat morphologically different from the observation in the present work. Detailed characterizations were performed and the hydrogen storage properties of carbon nitride tubes were investigated for the first time in Chapter 4 and 5 in this work.



## **4.2 Materials and Experimental Procedure**

### **4.2.1 Preparation of Carbon Nitride Micro/Nano Tubes**

The synthesis method of carbon nitride ( $C_3N_4$ ) micro/nano tubes consists of the following two-step condensation process. The first step was a hydrothermal decomposition of melamine in an airtight autoclave. In a typical treatment [257, 259], 5 g of melamine was loaded into a container made of polyphenylene (PPL) with 50 mL of tank volume. Then 50 mL of deionized water was added into the container. The solution was sonicated for 15 minutes and stirred for 30 minutes to evenly disperse the melamine powder. Following the dispersion, the polyphenylene-made vessel containing the homogenized solution was transferred to a stainless steel autoclave and sealed. The autoclave was heated at 200 °C for 24 hours and cooled down naturally. During the hydrothermal treatment, the melamine sample was condensed at an autogenic pressure. The white product was filtered off from the solution and was washed for five times with deionized water. Then the obtained product was dried at 40 °C for 12 hours.

The second step is the calcination of hydrothermally treated melamine. In this part, different parameters of calcination, such as sample amount, sample grinding, crucible airtightness, furnace type, protective gas, partition, heating rate, heating duration and heating temperature, were applied to investigate the influence of calcination conditions on the properties of final product. After calcination, a light yellowish material was collected and it was ascertained by X-ray diffraction to be  $C_3N_4$ . The parameters that gave the best yield and the highest surface area as measured by Brunauer-Emmett-Teller (BET) analysis, have been determined. These parameters were: 1.8 g of as-made hydrothermally treated melamine contained in a sealed crucible; with alumina balls as partition;

calcination in air at 560 °C for 4 hours with 5 °C/minute of heating rate. This specimen, denoted as H<sub>200</sub>-C<sub>560</sub>-C<sub>3</sub>N<sub>4</sub> (H<sub>x</sub>-C<sub>y</sub>-C<sub>3</sub>N<sub>4</sub>: x: hydrothermal temperature; y: calcination temperature), was chosen as one of the candidates for hydrogen storage tests. To further increase the production of tube-like carbon nitride, a series of trials upon hydrothermal treatment was carried out to adjust the morphology of crystalline melamine. In these trials, a polyphenylene-lined autoclave with 70 mL of inner volume was used. The melamine/deionized water solution was prepared in different proportions, and the solutions were added into polyphenylene-lined autoclave with different filling ratios. The specimens were dispersed by sonication for 15 minutes and stirring for 30 minutes. Then the samples were hydrothermally treated with different temperatures ranging from 180 °C to 220 °C for 24 hours and cooled down naturally. The hydrothermally treated melamine was filtered, washed and dried before calcination. The shapes of these melamine samples were observed by SEM, which showed that the condensed samples possessed the optimum bar-like melamine cyanurate formation and highest yield when the weight ratio of melamine/deionized water was 10 %, the filling ratio was 85 % and the heating temperature was 205 °C. This melamine cyanurate sample was calcined in a sealed crucible with alumina balls as partition under 560 °C in air for 4 hours. As a comparison, another batch of this sample was loaded into a boat alumina crucible which was placed in a semi-closed quartz tube and was calcined at 600 °C under Ar atmosphere for 4 hours. These two carbon nitride tube materials were denoted as H<sub>205</sub>-C<sub>560</sub>-C<sub>3</sub>N<sub>4</sub> and H<sub>205</sub>-C<sub>600</sub>-C<sub>3</sub>N<sub>4</sub>, respectively. Bulk graphitic carbon nitride (g-C<sub>3</sub>N<sub>4</sub>) was synthesized by the calcination of pure melamine powder at 600 °C for 4 hours in a semi-closed quartz tube under Ar gas protected.

## **4.2.2 Characterizations**

The morphology of the carbon nitride materials were observed by using Hitachi 3400X scanning electron microscope (SEM) equipped with a secondary electron (SE) detector at an operating voltage of 20 kV. Detailed morphology was characterized by transmission electron microscope (TEM, Phillips CM200). The TEM specimens were prepared via dispersing the powder in ethanol and the dispersed samples were collected by copper grids. The specimens were then dried at 40 °C for a day prior to TEM characterization. The crystal structure and phase identification were investigated with a PANalytical Xpert Pro MPD X-ray diffractometer with Cu K $\alpha$  radiation ( $\lambda=1.5406$  Å) with an operating voltage at 45 kV and current at 40 mA. The analysis of the diffraction pattern was completed by using X'pert HighScore Plus software. Fourier transform infrared spectrometer (Spectrum 100, PerkinElmer) was employed to study the functional group vibrations, scanning from 600-4000 cm<sup>-1</sup> in UATR mode.

## **4.3. Results and Discussion**

### **4.3.1 Hydrothermal Treatment Studies**

The morphologies of melamine samples observed by SEM are shown in Figure 4.1. Pure melamine has an irregular structure (Figure 4.1a) and it transformed to different configurations after hydrothermal treatments (Figure 4.1b-r). A crystal-like structure intermingled with branch-like melamine was formed by means of a typical hydrothermal treatment, where 5 g of pure melamine plus 50 mL of deionized water were heated in an autoclave having 50 mL of volume at 200 °C for 24 hours (Figure 4.1b). The SEM images give a discrepant observation compared to the sheet-like melamine prepared by two-step condensation treatment reported by Jin et al [257].

The branch-like or bar-like melamine were expected to convert to carbon nitride tubes after subjected to calcination. Hence, a series of experiments in hydrothermal treatment were designed and performed to increase the amount of bar-like melamine, as tabulated in Table 4.2. Three dominant factors, including heating temperatures (top row), weight ratio of melamine/deionized water (left column) and filling ratio (right column), were altered to shape the melamine samples. A polyphenylene-lined autoclave with 70 mL of volume was used in this study.

To investigate the impact of these factors on the morphology of treated melamine, the microstructures of different samples were compared. As it can be seen from the samples synthesized at various heating temperatures with fixed solution concentration and filling ratio, the formation of bar-like melamine is enhanced as the temperature increases, while the yield of product is largely decreased. This could be attributed to the increased solubility of melamine in water with the elevated temperature [261, 262], leading to a more concentrated alkaline solution caused by the generation of ammonia from melamine condensation. The alkaline environment facilitates the hydrolysis of melamine and converts it to cyanuric acid by the substitution of hydroxyl functional groups for amino groups, as reported by Bann et al. [263]. Melamine and cyanuric acid can bind together via hydrogen bond to form melamine cyanurate [264], which has large molecule and is prone to precipitate because of the reduced solubility [265]. Son et al. and Nagai et al. have observed needle-like melamine cyanurate by mixing melamine with cyanuric acid [262, 266], which is analogous to our finding. Thus the white product obtained in our research is hypothesized as melamine cyanurate. The reduced amount of product could be related to the boosted autogenous pressure in hydrothermal process with the growing temperature, which may induce a more serious vessel deformation and force the dissolved

melamine cyanurate to escape through the pressurized vapor. This can be supported by the white solid residual stuck on the interior wall of stainless steel autoclave.

By comparing Figure 4.1f and p, Figure 4.1k and q, Figure 4.1n and o, and Figure 4.1m and r, respectively, one can find that the lower the ratio of melamine to deionized water is, the more the bar-like melamine cyanurate are created. It is believed that a more completed hydrolysis and cross-binding reaction can be achieved as less melamine reactant is used at a low solution concentration.

The effect of filling ratio is explored by checking the sample morphologies at 10 % of melamine/deionized water under 200 °C of heating temperature. A low filling ratio is found to have better gain in bar-like melamine cyanurate. This is because less melamine amount is loaded at a low filling ratio under a fixed solution concentration, and hence a more completed hydrothermal reaction is expected. Another reason could be the lower autogenic pressure generated under a low filling ratio, which results in a spontaneous reaction to produce more  $\text{NH}_3$  gas so as to improve the formation of cyanuric acid as well as the yield of melamine cyanurate.

The samples with well conversion to bar-like melamine cyanurate are shown in the enlarged images: Figure 4.1d1, f1, i1, l1 and m1. The length and diameter of melamine cyanurate bars are listed in Table 4.3. The results show that the samples have reasonable dimensions, several tens  $\mu\text{m}$  of length and 1-3  $\mu\text{m}$  of diameter, when they are synthesized under higher temperatures and lower filling ratios. However, the yield of the product is relatively low. Considering that a larger sample amount is required for calcination process and hydrogen storage measurement, the parameters applied to preparing the sample Figure 4.1l were chosen as the optimum method for the hydrothermal treatment in this study because it has a better production of bar-like melamine cyanurate.

**Table 4.2:** Experimental parameters and yields of product in hydrothermal treatment.

*Table 4.2 has been removed due to Copyright restrictions*

**Table 4.3:** Dimension of bar-like melamine cyanurate with different synthesis conditions.

*Table 4.3 has been removed due to Copyright restrictions*

**10% concentration and 30% filled:**

**10% concentration and 50% filled:**

**10% concentration and 65% filled:**

**10% concentration and 70% filled:**

**10% concentration and 85% filled:**



**10% concentration and 85% filled:**

**10% concentration and 100% filled:      25% concentration and 100% filled:**

**30% concentration and 50% filled:      34% concentration and 85% filled:**

### **34% concentration and 85% filled:**

*Figure 4.1 has been removed due to Copyright restrictions*

**Figure 4.1:** SEM images of (a) pure melamine and (b-r) hydrothermally treated melamine cyanurate under different synthesis conditions.

To reconfirm whether the result can be reproduced with a larger vessel, a PPL-lined autoclave with 100 mL of volume was applied in an additional experiment. The parameters of preparing the sample 4.11 were implemented to synthesize bar-like melamine cyanurate. However, a large proportion of bulk melamine cyanurate with the dimension of several tens micron was found in the specimen, indicating a poor transformation, as shown in Figure 4.2a. A Teflon-made solid cylinder with 30 mL of volume was then placed in the vessel to occupy the inner volume so as to simulate the identical condition as used in the preparation of sample Figure 4.11. As illustrated in Figure 4.2b, the treated sample still contained considerable bulk melamine cyanurate. The 100 mL autoclave was then placed horizontally in the oven in order to increase the reaction surface of melamine with water. The SEM image (Figure 4.2c) exhibits a high transformation into bar-like melamine cyanurate with around 3  $\mu\text{m}$  of diameter, suggesting the reactive surface area is very important for bar-like sample formation. This could be also beneficial to an upscale synthesis.

*Figure 4.2 has been removed due to Copyright restrictions*

**Figure 4.2:** SEM images of melamine cyanurate treated hydrothermally with the autoclave which has (a) 100 mL of volume, (b) the reduced volume from 100 mL to 70 mL and (c) 100mL of volume but horizontally placed in an oven.

The crystal structures of as-received melamine and melamine cyanurate condensed at different hydrothermal processes are reflected in X-ray diffraction patterns (Figure 4.3). The samples denoted as (a) to (r) in Figure 4.3 correspond to the samples shown in Table 4.2 and Figure 4.1. A change of peak distribution indicates a new arrangement in melamine structure after hydrothermal reaction. The appearance of three peaks at around

10.9°, 18.4° and 21.96°, indexed as (100), (110), and (200), is an evidence of in-planar packing in melamine-cyanuric acid complex. Moreover, an intense peak observed at around 28°, which can be indexed as (002), is an indicator of the lamellar stacking of melamine cyanurate [267, 268]. Owing to the variations of sample morphologies under different synthesis conditions, the intensity of the peaks is changed accordingly by distinct growth directions and preferred orientations. For example, the samples predominantly containing bulk or sheet-like melamine cyanurate have very high intensity in (002) peak, such as 4.3(b), (c), (e), (g), (n), (o), (p) and (r). On the contrary, the samples with highly transformation of bar-like melamine cyanurate reveal an enormous reduction of (002) peak. The absence of above-mentioned peaks in Figure 4.3(q) suggests an incomplete formation of melamine cyanurate.

*Figure 4.3 has been removed due to Copyright restrictions*

**Figure 4.3:** XRD patterns of (a) pure melamine and (b-r) hydrothermal treated melamine.

In addition to XRD, the formation of melamine cyanurate was further confirmed by conducting Fourier transform infrared (FT-IR) spectrum, as shown in Figure 4.4. The samples chosen for FT-IR analysis were pure melamine, typical HT melamine (hydrothermally treated by the typical method) and optimized HT melamine (hydrothermally treated with the optimized parameters: 4.11 in Table 4.2). The appearance of two new peaks at 1729 and 1780  $\text{cm}^{-1}$  underpins the existence of C=O stretching vibration of melamine cyanurate [268]. Furthermore, due to the hydrogen bonding between cyanuric acid and melamine, the triazine ring vibration of melamine is moved to a lower frequency from 810 to 764  $\text{cm}^{-1}$  [267].

Based on the results of XRD and FT-IR, the hydrothermally treated samples in this study can be asserted to be melamine cyanurate compound.

*Figure 4.4 has been removed due to Copyright restrictions*

**Figure 4.4:** FT-IR spectrum of pure melamine and hydrothermally treated melamine.

### 4.3.2 Calcination Studies for Carbon Nitride Tubes

The calcination parameters and results for the preparation of carbon nitride materials are enumerated in Table 4.4 and Table 4.5. Pure  $C_3N_4$  was synthesized by loading pure melamine powder in a  $Al_2O_3$  boat crucible, which was placed in the middle of a quartz tube, and being heated at 600 °C under Ar for 4 hours. To investigate the optimum calcination conditions for  $C_3N_4$  tubes, the melamine cyanurate samples used in this pyrolysis study were prepared following the typical method (Figure 4.1b) as more yields per treatment could be obtained. According to the results, several factors can significantly influence the calcination outcome. First, if the amount of melamine is not plenty enough, the sample quantity will considerably reduce during calcination due to a severe sublimation. Second, a better result can be obtained by using tube furnace other than muffle furnace under the same heating conditions because of the system structure of tube furnace is relatively easy to keep the gas pressure within the chamber so as to suppress the sublimation of carbon nitride. The inert gas, Ar or  $N_2$ , introduced in the tube furnace has imperceptible influence on the calcination results. However, the limited chamber size of tube furnace makes it unsuitable for mass production. Hence, a method is reported here to increase the product yield using muffle furnace. A cup crucible holding melamine samples was placed on a  $Al_2O_3$  plate and covered with another inverted bigger cup crucible. The gap between the plate and the fringe of the bigger crucible was sealed by a high-temperature sealant, aluminium phosphate monobasic. In this case, the sublimation of carbon nitride was suppressed by the pressure generated from the condensation of carbon nitride. Third, the heating temperature below 600 °C is better for the synthesis of tubular carbon nitride. Excessively high temperature and long heating time brings about a substantial reduction of the product yield. However, a low temperature may lead to an

incomplete pyrolysis. For instance, the surface area of carbon nitride tubes obtained at 500 °C is lower than that given under 560 °C, which will be discussed later in the section of BET surface area analysis in Chapter 5. On the other hand, the effect of heating rate on the result may be negligible.

The Al<sub>2</sub>O<sub>3</sub> balls partition can provide more space for gas diffusion and enhance the pyrolysis, increasing the surface area of C<sub>3</sub>N<sub>4</sub> tubes. More details will be studied in the section of BET surface area analysis in Chapter 5. The grinding of melamine samples damaged the tubular structure of carbon nitride tubes. Thus it is not suggested to apply grinding to the preparation of bar-like melamine cyanurate. Evidence will be shown in the SEM images. In short, the optimum pyrolysis parameters for synthesizing carbon nitride tubes are advised to be a large quantity of as-made melamine cyanurate contained in a sealed crucible; with alumina balls as partition; calcination in air at 560 °C for 4 hours with 5 °C/minute of heating rate.

**Table 4.4:**     **Calcination conditions for pure melamine and as-made melamine cyanurate.**

*Table 4.4 has been removed due to Copyright restrictions*



**Table 4.5:**     **Calcination conditions for ground melamine cyanurate.**

*Table 4.5 has been removed due to Copyright restrictions*

*Table 4.5 has been removed due to Copyright restrictions*

To study the effects of calcination conditions on the morphology of carbon nitride tubes, some selected samples prepared under various pyrolysis states (Table 4.6) were observed by Scanning Electron Microscope (SEM), as shown in Figure 4.5. The heating rates for the calcinations are not shown in Table 4.6 as they are all fixed at 5 °C/min.

According to the observations based on Table 4.6 and Figure 4.5, some conclusions can be drawn as the followings. First, the pyrolysis using boat crucible and tube furnace is able to convert the as-made baculiform melamine cyanurate into tubular carbon nitride under air or inert gas (Figure 4.5g-j). While the heating period was doubly prolonged for the pyrolysis in tube furnace, the C<sub>3</sub>N<sub>4</sub> tubes could still form (Figure 4.5h). Second, in contrast to the heat treatment with tube furnace, the approach using muffle furnace coupled with semi-closed cup crucible burns away C<sub>3</sub>N<sub>4</sub> tubes and only sheet-like C<sub>3</sub>N<sub>4</sub> remains (Figure 4.5a). However, if the cup crucible is sealed to keep the sublimated C<sub>3</sub>N<sub>4</sub> within the crucible as protective surroundings, the same tube formation as given by tube furnace can be achieved by muffle furnace (Figure 4.5b-f). The advantages of this method over tube furnace are that the facility is easier to access and it can produce a larger quantity of the materials. Third, the influence of partitions on the morphology is hard to tell from the SEM images (Figure 4.5b and d), but some differences are revealed in surface area, which will be discussed in Chapter 5. Fourth, the rod structure of melamine cyanurate is destroyed by the grinding, and only some porous frameworks remain after calcination (Figure 4.5k).

**Table 4.6:** Pyrolysis conditions for C<sub>3</sub>N<sub>4</sub> tubes preparation.

*Table 4.6 has been removed due to Copyright restrictions*

*Figure 4.5 has been removed due to Copyright restrictions*

**Figure 4.5:** SEM images of  $C_3N_4$  prepared at different pyrolysis conditions corresponding to Table 4.6.

Since the parameters for hydrothermal treatment and calcination have been comprehensively discussed, four carbon nitride candidates were selected for further characterizations and hydrogen storage measurements. Figure 4.6 shows the SEM images

of these four sample: (a) Bulk g-C<sub>3</sub>N<sub>4</sub>: pure carbon nitride synthesized by the calcination of pure melamine powder at 600 °C for 4 hours in a semi-closed quartz tube under Ar gas protected; (b) H<sub>200</sub>-C<sub>560</sub>-C<sub>3</sub>N<sub>4</sub>: typical hydrothermally treated melamine cyanurate was loaded in a sealed crucible, with alumina balls as partition, and pyrolyzed in air at 560 °C for 4 hours with 5 °C/minute of heating rate; (c) H<sub>205</sub>-C<sub>560</sub>-C<sub>3</sub>N<sub>4</sub>: optimum hydrothermally treated melamine cyanurate was calcined in a sealed crucible with alumina balls as partition under 560 °C in air for 4 hours. (d) H<sub>205</sub>-C<sub>600</sub>-C<sub>3</sub>N<sub>4</sub>: optimum hydrothermally treated melamine cyanurate was contained in a boat crucible, which was placed in a semi-closed quartz tube and was calcined at 600 °C under Ar atmosphere for 4 hours.

As clearly seen in Figure 4.6, Bulk g-C<sub>3</sub>N<sub>4</sub> shows irregular structure which is quite dissimilar from other three specimens. H<sub>200</sub>-C<sub>560</sub>-C<sub>3</sub>N<sub>4</sub>, H<sub>205</sub>-C<sub>560</sub>-C<sub>3</sub>N<sub>4</sub>, and H<sub>205</sub>-C<sub>600</sub>-C<sub>3</sub>N<sub>4</sub> all have tubular structures with several microns of tube diameter, which are generally larger and less uniform than the carbon nitride nanotubes synthesized by chemical vapor deposition or other methods with the utilization of template and substrate for dimension control [229, 231, 234, 235, 237]. The sizes of carbon nitride tubes in this study are similar to that in prior arts based on the chemical reaction of C-N-constituted materials with various solvents and catalysts [233, 242, 245, 247, 249, 258].

In addition to the tubular structure, H<sub>200</sub>-C<sub>560</sub>-C<sub>3</sub>N<sub>4</sub> has cotton-like frameworks due to its relatively lower content of bar-like melamine cyanurate formed in the hydrothermal treatment. The cotton-like frameworks may be converted from bulk melamine cyanurate in the pristine samples. Both H<sub>205</sub>-C<sub>560</sub>-C<sub>3</sub>N<sub>4</sub> and H<sub>205</sub>-C<sub>600</sub>-C<sub>3</sub>N<sub>4</sub> were synthesized from optimum melamine cyanurate with a high proportion of rod structure. However, with different calcination methods, the morphologies of the carbon nitride products vary. H<sub>205</sub>-C<sub>560</sub>-C<sub>3</sub>N<sub>4</sub> possesses a high ratio of C<sub>3</sub>N<sub>4</sub> tubes with several tens micron of length, but

H<sub>205</sub>-C<sub>600</sub>-C<sub>3</sub>N<sub>4</sub> shows a shorter C<sub>3</sub>N<sub>4</sub> tube length. This indicates that an excessively high calcination temperature may induce a serious destruction of the tubular texture in the H<sub>205</sub>-C<sub>600</sub>-C<sub>3</sub>N<sub>4</sub> sample, even though it was protectively heat treated under argon atmosphere. This may support that a thermal condensation carried out in an isolated chamber with the sublimated C<sub>3</sub>N<sub>4</sub> as protective gas could be a feasible way for the synthesis of C<sub>3</sub>N<sub>4</sub> tubes.

*Figure 4.6 has been removed due to Copyright restrictions*

**Figure 4.6:** SEM images of selected C<sub>3</sub>N<sub>4</sub> materials: (a) Bulk g-C<sub>3</sub>N<sub>4</sub>; (b) H<sub>200</sub>-C<sub>560</sub>-C<sub>3</sub>N<sub>4</sub>; (c) H<sub>205</sub>-C<sub>560</sub>-C<sub>3</sub>N<sub>4</sub>; (d) H<sub>205</sub>-C<sub>600</sub>-C<sub>3</sub>N<sub>4</sub>.

Figure 4.7 shows the TEM images of the (a) microtube and (b) nanotube of  $\text{H}_{205}\text{-C}_{560}\text{-C}_3\text{N}_4$ . The outer tube diameter of nanotubes is around 200 nm and the thickness of tube wall is about 30 nm. In addition to the individual nanotubes (Figure 4.7b), nanotubes were also found along the interior wall of microtubes (Figure 4.7a).

*Figure 4.7 has been removed due to Copyright restrictions*

**Figure 4.7:** TEM images of  $\text{H}_{205}\text{-C}_{560}\text{-C}_3\text{N}_4$ : (a) microtube; (b) nanotube.

## 4.4 Conclusion

A facile synthesis approach comprising hydrothermal treatment and pyrolysis of sole melamine is investigated to prepare tubular carbon nitrides without any template, substrate, catalyst, acid and alkaline. Optimized parameters for preparing a large quantity of rod-like melamine cyanurate by hydrothermal treatment are determined as the concentration of melamine solution: 10 %, the filling ratio: 85 %, the heating temperature: 205 °C and the heating duration: 24 hours. Following the hydrothermal treatment, the optimum pyrolysis conditions are worked out to be as-made hydrothermally treated melamine contained in a sealed crucible; with alumina balls as partition; calcination in air at 560 °C for 4 hours with 5 °C/minute of heating rate. By these methods, a large amount of carbon nitride tubes with a long tube length and micro-/nano- scale of tube diameters can be obtained.



# **Chapter 5    Characterizations and Hydrogen Storage Properties of Tubular Carbon Nitrides**

## **5.1    Introduction**

Hydrogen storage is the bottleneck to the realization of hydrogen economy. Presently for fuel cell vehicles, hydrogen is stored in highly pressurized tanks of 70 MPa, which is a potential hazard to drivers. To reduce the storage pressure, in this work, carbon nitride ( $C_3N_4$ ) micro- or nano-tubes are selected and designed to store hydrogen by a combination of physisorption and chemisorption. Compared with carbon nanotubes,  $C_3N_4$  tube walls are highly porous caused by nitrogen doping to facilitate hydrogen access to the interior of the tubes, and the doubly bonded nitrogen provides active sites for chemisorption, leading to a higher absorption heat. This results in a higher hydrogen storage capacity of this material (5.45 wt% in theory) than that of carbon nanotubes at room temperature [21]. This theoretical hydrogen capacity is approaching the target of U.S. Department of Energy by 2025 (5.5 wt%) [13]. More comprehensive literature reviews about carbon materials and carbon nitrides have been elucidated in Chapter 4.

Another benefit of tubular  $C_3N_4$  is that the raw material is inexpensive and the fabrication method is simple. It is expected to have potential to replace the pressurized hydrogen storage as it is more economical, a lot safer with much lower storage pressure of 10 MPa or below. The total weight of the hydrogen storage system may be similar or lower. A fast hydrogen refueling and release speed are expected due to the physisorption characteristic— a distinct advantage over the battery driven electric vehicles.

## **5.2 Experimental Procedure**

### **5.2.1 Characterizations**

The elemental distribution was determined by an energy dispersive X-ray spectrometer (EDS) at 15 kV. The crystal structure and phase identification were investigated with a PANalytical Xpert Pro MPD X-ray diffractometer with Cu K $\alpha$  radiation ( $\lambda=1.5406$  Å) with an operating voltage at 45 kV and current at 40 mA. The analysis of the diffraction pattern was completed by using X'pert HighScore Plus software. The surface area and internal pore characteristics were measured at 77 K by Micromeritics TriStar 3000 Analyzer applying Brunauer-Emmett-Teller (BET) manner and Barrett-Joyner-Halenda (BJH) desorption method, after degassing at 150 °C for 3 hours to remove moisture. Fourier transform infrared spectrometer (Spectrum 100, PerkinElmer) was employed to study the functional group vibrations, scanning from 600-4000 cm<sup>-1</sup> in UATR mode.

### **5.2.2 Hydrogen Storage Properties**

Hydrogen storage and kinetics measurements were conducted using volumetric method by Sievert instrument where ultra-high purity hydrogen gas (99.999%) was utilized to avoid undesired toxic gas. The dead volumes of the system chambers were precisely calibrated by introducing 0.1-0.5 MPa of hydrogen gas at different temperatures, which is on the basis of Japanese Industrial Standard H 7201 (JIS H 7201) [269]. Prior to the hydrogen storage investigation, the carbon nitride samples were degassed at 150 °C for 4 hours under vacuum (10<sup>-3</sup> torr) to eliminate moisture and residual gases, followed by a cooling down to room temperature.

The activated samples were stepwisely charged with pure hydrogen gas at room temperature and then the equilibrium values at different pressures were recorded. The desorption studies were established by reducing the hydrogen pressure in the system chamber isothermally. The operations were repeated to measure the hydrogen storage capacity of all the samples at 0, 50 °C and 100 °C, respectively. Before each measurement, the samples were evacuated at 150 °C under vacuum for 4 hours. Based on the calculation of pressure drops, the hydrogen storage capacities can be obtained in weight percentage and be plotted in the form of pressure-composition-isotherm (PCI).

Because the sample was found to possess a low hydrogen absorption rate and very high desorption rate at/above 50 °C, the hydrogen absorption/desorption kinetics of the samples were studied at room temperature only. Here the absorption rate was measured under a sudden exposure to 3.6 MPa of pure hydrogen gas; while the desorption rate was measured under vacuum condition. The pressure decrease as a function of time was recorded over the reaction.

The chemisorption of hydrogen was further measured by ChemiSorb 2750 (Micromeritics) from room temperature to 500 °C. Before chemisorption studies, the samples were charged with 10% H<sub>2</sub>+Ar flowing gas at 20 °C, 50 °C and 100 °C, respectively.

## **5.3 Surface Properties and Structure Analysis**

### **5.3.1 Composition Analysis**

The composition analysis of carbon nitride materials was done by using energy dispersive X-ray spectrometer (EDS). Figure 5.1 shows there are three dominant elements: carbon, nitrogen and oxygen in all the samples and the quantitative results are exhibited in Table 5.1. As shown in the results, the samples are all nitrogen-enriched, while the C/N ratios are higher than the theoretical value of pristine  $C_3N_4$  (0.75). Their nitrogen contents are beyond or close to 50 at%, which are much higher than the nitrogen contents reported in various N-doped carbonaceous materials prepared by different approaches, including chemical vapor deposition [24, 188-192], nitrogen plasma treatment [196, 198], chemical pyrolysis [23, 182, 201, 208, 209] and hydrothermal treatment [187, 204].

*Figure 5.1 has been removed due to Copyright restrictions*

*Figure 5.1 has been removed due to Copyright restrictions*

**Figure 5.1:** EDS images of selected  $C_3N_4$  materials: (a) Bulk g- $C_3N_4$ ; (b)  $H_{200}-C_{560}-C_3N_4$ ; (c)  $H_{205}-C_{560}-C_3N_4$ ; (d)  $H_{205}-C_{600}-C_3N_4$ .

**Table 5.1:** Composition distribution of selected  $C_3N_4$  materials.

*Table 5.1 has been removed due to Copyright restrictions*

### 5.3.2 Surface Area Analysis

Comprehensive reports about the pore texture of the chosen carbon nitride materials were conducted by nitrogen sorption measured under 77 K. The pore characteristics, such as surface area, pore volume and average pore size, are enumerated in Table 5.2 and the nitrogen adsorption-desorption isotherm is shown in Figure 5.2. In addition to the four candidate materials for hydrogen storage, two more samples were also examined by BET surface area analysis to investigate the effects of partition and pyrolysis temperature on the pore structure. The two samples are: (1)  $H_{200}-C_{560}-C_3N_4$  without partition (Figure 4.5b), which was synthesized by the same method as applied to  $H_{200}-C_{560}-C_3N_4$ , but no partition was loaded in the crucible, and (2)  $H_{200}-C_{500}-C_3N_4$  (Figure 4.5c), where the same melamine cyanurate used for preparing  $H_{200}-C_{560}-C_3N_4$  was thermally decomposed at 500 °C.

Based on IUPAC classification, all of the  $N_2$  adsorption-desorption isotherms can be identified as type IV isotherms and type H3 hysteresis loops, indicating the existence of mesopores and the occurrence of capillary condensation in the pores [270]. As it can be realized in Table 5.2, among the selected samples,  $H_{205}-C_{560}-C_3N_4$  has the highest surface area, 148.69  $m^2/g$ , which is about 7 times higher than Bulk  $g-C_3N_4$  (21.38  $m^2/g$ ). This value is also the highest in the current researches of carbon nitride nanotubes with a similar nitrogen content. Further higher surface area was only achieved by chemical vapor deposition (CVD) method and the nitrogen amount of the  $C_3N_4$  tubes was only around 3 at% [240, 271]. The superior surface area could be ascribed to the high proportion of tube-like  $C_3N_4$  and its porous structure. It is of interest that  $H_{205}-C_{600}-C_3N_4$  has relatively low surface area (51.54  $m^2/g$ ) and a large average pore size (34.85 nm) despite the employment of the same melamine cyanurate used in  $H_{205}-C_{560}-C_3N_4$  synthesis. This may

suggest that the excessively high pyrolysis temperature (600 °C) could result in a loss of C<sub>3</sub>N<sub>4</sub> tubes because the high reaction surface of tubes is very vulnerable to sublimation, which is consistent with the SEM image displayed in Figure 4.6d.

H<sub>200</sub>-C<sub>560</sub>-C<sub>3</sub>N<sub>4</sub> has a reasonable surface area (105.98 m<sup>2</sup>/g) and a small pore size (5.88 nm). However, if there is no partition (Al<sub>2</sub>O<sub>3</sub> balls) loaded in the crucible during calcination, the surface area is significantly reduced by 24 % to 80.33 m<sup>2</sup>/g (H<sub>200</sub>-C<sub>560</sub>-C<sub>3</sub>N<sub>4</sub> without partition). If the pyrolysis temperature is lowered to 500 °C, the surface area is considerably decreased by 49 % to 54.27 m<sup>2</sup>/g (H<sub>200</sub>-C<sub>500</sub>-C<sub>3</sub>N<sub>4</sub>) and the pore volume (0.098 cm<sup>3</sup>/g) is even lower than that of Bulk g-C<sub>3</sub>N<sub>4</sub> (0.176 cm<sup>3</sup>/g), indicating an unfulfilled conversion into porous texture.

The pore size distribution of the selected C<sub>3</sub>N<sub>4</sub> materials is shown in Figure 5.3. As it can be clearly observed, two samples, Bulk g-C<sub>3</sub>N<sub>4</sub> and H<sub>205</sub>-C<sub>600</sub>-C<sub>3</sub>N<sub>4</sub> which were both calcined at 600 °C under Ar, possess broad pore size regions above 30 nm due to the deficiency of tubular C<sub>3</sub>N<sub>4</sub>. On the contrary, other samples, which were calcined at 560 °C in an isolated environment, have a narrow pore size range centred at 4 nm. This supports that the smaller diameter can lead to the higher surface area as more exposed surface is created in a given specimen weight.

In conclusion, the unfavourably high or low heating temperature decreases the surface area of carbon nitride materials as a result of C<sub>3</sub>N<sub>4</sub> tubes reduction or incomplete thermal decomposition, even though the pyrolysis is carried out under Ar protection. On the other hand, a moderate temperature (560 °C) is suitable for the preparation of carbon nitride tubes with a high surface area. In addition, the synthesis performed with a sealed and partitioned crucible in a muffle furnace is an ideal way to produce a large quantity of tubular C<sub>3</sub>N<sub>4</sub> samples.



*Figure 5.2 has been removed due to Copyright restrictions*

**Figure 5.2:** Nitrogen adsorption-desorption isotherms of selected C<sub>3</sub>N<sub>4</sub> materials at 77 K.

*Figure 5.3 has been removed due to Copyright restrictions*

**Figure 5.3:** Pore size distribution of selected C<sub>3</sub>N<sub>4</sub> materials.

**Table 5.2:** BET surface area characteristics of carbon nitride materials.

*Table 5.2 has been removed due to Copyright restrictions*

### 5.3.3 Phase Identification and Crystal Structure

The crystal structures of the selected carbon nitride materials were studied by X-ray diffraction (XRD), as plotted in Figure 5.4. All of the treated samples have two major diffraction peaks, which is in good accordance with bulk g-C<sub>3</sub>N<sub>4</sub>. This indicates the crystal structure of carbon nitride tubes remains unchanged as that of bulk g-C<sub>3</sub>N<sub>4</sub> after subjected to different thermal condensation treatments. The peak at 12.76°, which has been indexed as the (210) plane in an orthorhombic geometry, corresponds to the intralayer of tri-s-triazine units [272]. The intensive peak at 27.7°, identified as the (002) plane, reflects the inter-planar distance between the graphitic layers of the stacking of the conjugated aromatic system [272, 273]. As observed in XRD of selected C<sub>3</sub>N<sub>4</sub> materials: (a) Bulk g-C<sub>3</sub>N<sub>4</sub>; (b) H<sub>200</sub>-C<sub>560</sub>-C<sub>3</sub>N<sub>4</sub>; (c) H<sub>205</sub>-C<sub>560</sub>-C<sub>3</sub>N<sub>4</sub>; (d) H<sub>205</sub>-C<sub>600</sub>-C<sub>3</sub>N<sub>4</sub>., the low-

angle (210) peak intensity of the samples containing tubular  $C_3N_4$  (Figure 5.4b-d) is less pronounced, compared with the intensity given by bulk g- $C_3N_4$ . This could be due to the reduced planar size in carbon nitride tubes [274]. Furthermore, the weaker intensity of high-angle (002) peak provided by tube-like samples could be attributed to the smaller size and loose stacking of graphitic  $C_3N_4$  layers [275-277]. The layer distance of these samples is around 0.321-0.323 nm, which is determined by the d-spacing of (002) plane. This layer spacing is smaller than that of multi-walled carbon nanotubes (MWCNTs), 0.34 nm, demonstrating that the introduction of nitrogen atoms into graphite structure may induce the shrinkage of layer distance. This could be considered as the distortion caused by the substitution of smaller nitrogen (atomic radius: 65 pm) for carbon (atomic radius: 70 pm).

*Figure 5.4 has been removed due to Copyright restrictions*

**Figure 5.4:** XRD of selected  $C_3N_4$  materials: (a) Bulk g- $C_3N_4$ ; (b)  $H_{200}-C_{560}-C_3N_4$ ; (c)  $H_{205}-C_{560}-C_3N_4$ ; (d)  $H_{205}-C_{600}-C_3N_4$ .

### 5.3.4 Chemical Structure

The structures of functional groups in four selected carbon nitride materials were further investigated by Fourier transform infrared (FTIR) spectroscopy, as shown in Figure 5.5. The features of IR spectrum for these four samples are nearly identical, indicating the chemical structures of carbon nitride tubes are almost the same as that of Bulk g-C<sub>3</sub>N<sub>4</sub>. That is, the hydrothermal treatment merely alters the physical structure of g-C<sub>3</sub>N<sub>4</sub> other than the chemical structure. The band at 806 cm<sup>-1</sup> represents the breathing mode of the tri-s-triazine ring units [278]. The peaks at 1230, 1313 and 1396 cm<sup>-1</sup> correspond to aromatic C–N stretching, and the peaks at around 1568 and 1627 cm<sup>-1</sup> could be assigned to the existence of CN double bonds [279]. The broad absorption band in the region of 3000-3500 cm<sup>-1</sup> could be related to the N–H stretching and O–H bonds of the adsorbed water molecules [278, 279].

*Figure 5.5 has been removed due to Copyright restrictions*

**Figure 5.5:** FT-IR of selected C<sub>3</sub>N<sub>4</sub> materials: (a) Bulk g-C<sub>3</sub>N<sub>4</sub>; (b) H<sub>200</sub>-C<sub>560</sub>-C<sub>3</sub>N<sub>4</sub>; (c) H<sub>205</sub>-C<sub>560</sub>-C<sub>3</sub>N<sub>4</sub>; (d) H<sub>205</sub>-C<sub>600</sub>-C<sub>3</sub>N<sub>4</sub>.

## 5.4 Hydrogen Storage Properties

### 5.4.1 Absorption Hydrogen Capacity

The hydrogen storage capacities of four selected  $C_3N_4$  materials were investigated through volumetric manner under room temperature and up to 3.6 MPa of  $H_2$  pressure, as depicted in Figure 5.6. This is the first time that  $C_3N_4$  tubes were tested for hydrogen storage purpose. The maximum hydrogen uptake of Bulk g- $C_3N_4$ ,  $H_{200}-C_{560}-C_3N_4$ ,  $H_{205}-C_{560}-C_3N_4$  and  $H_{205}-C_{600}-C_3N_4$  were 0.19, 0.31, 0.62 and 0.28 wt%, respectively. Among these specimens,  $H_{205}-C_{560}-C_3N_4$  provided the most superior hydrogen capacity of 0.62 wt%, which may be due to its highest surface area. This can be supported by comparing the surface area and hydrogen capacity of different samples. As observed in Figure 5.7, the hydrogen storage capacities of the  $C_3N_4$  samples are in good accordance with the variation of surface area. Since the results of EDS, XRD and FTIR didn't show much contrast between the samples in the elemental distribution, crystal structure and chemical structure, the difference in the BET surface area could be a critical determinant for the hydrogen storage performance of the  $C_3N_4$  materials.

Based on the absorption capacity characterized at 20 °C, the  $H_2$  capacity of  $H_{205}-C_{560}-C_3N_4$  up to 10 MPa was estimated by extrapolation, as exhibited in Figure 5.8. The graph shows that tubular carbon nitride material is expected to absorb 2.62 wt% of hydrogen at 10 MPa. This hypothetical capacity is about 48 % of the theoretical  $H_2$  capacity (5.45 wt%) calculated by Koh et al [21]. In the future, the capacity may be further enhanced if a higher surface area is created by tube diameter reduction or a doping of catalyst is applied to facilitate the dissociation of  $H_2$  molecules into H atoms.

*Figure 5.6 has been removed due to Copyright restrictions*

**Figure 5.6:** Pressure-composition-isotherms for the hydrogen absorption capacities of selected  $C_3N_4$  materials at 20 °C.

*Figure 5.7 has been removed due to Copyright restrictions*

**Figure 5.7:** Correlation between surface area and  $H_2$  uptake of selected  $C_3N_4$  materials.

*Figure 5.8 has been removed due to Copyright restrictions*

**Figure 5.8:** Estimation of hydrogen storage capacity of  $\text{H}_{205}\text{-C}_{560}\text{-C}_3\text{N}_4$  up to 10 MPa.

### 5.4.2 Hydrogen Capacity at Various Temperatures

In addition to the measurement under 20 °C, the hydrogen storage capacity of  $\text{H}_{205}\text{-C}_{560}\text{-C}_3\text{N}_4$  was further characterized at 0, 50 and 100 °C, as displayed in Figure 5.9. The hydrogen storage capacity under 0 °C is a bit less than under 20 °C, which may be due to the reduction of chemisorption at lower temperature. The absorption/desorption capacities of  $\text{H}_{205}\text{-C}_{560}\text{-C}_3\text{N}_4$  are quite limited at 50 °C and 100 °C, indicating that at higher temperatures it is hard to physisorb hydrogen molecules on  $\text{C}_3\text{N}_4$  surface and chemisorb hydrogen atoms to form chemical bonds. Moreover, most of the hydrogen absorbed at 20 °C is able to be released at room temperature, which reveals an outstanding storage reversibility.

*Figure 5.9 has been removed due to Copyright restrictions*

**Figure 5.9:** Pressure-composition-isotherms of  $\text{H}_{205}\text{-C}_{560}\text{-C}_3\text{N}_4$  at 0, 20, 50 and 100 °C.

### 5.4.3 Chemisorption Measurement

The PCI outcome can be further confirmed by chemisorption test (Figure 5.10), where  $\text{H}_{205}\text{-C}_{560}\text{-C}_3\text{N}_4$  was firstly charged with 10%  $\text{H}_2$ +Ar at 20 °C, 50 °C and 100 °C and then dynamically discharged by heating from room temperature to 500 °C. The sample charged at 20 °C shows a significant desorption peak at around 25 °C and a lower peak at 60 °C, suggesting that the major desorption took place at room temperature and the complete desorption happened at 60 °C. The samples charged at 50 °C and 100 °C both give desorption peaks at about 40 °C, which are lower than their absorption temperatures, indicating that these desorption behaviours may originate from the residual hydrogen adsorbed on the material surface and the hydrogen is relatively easy to escape from the surface at near room temperature. The results of chemisorption are consistent with the hydrogen storage capacities measured by volumetric method in Figure 5.9, which evidences that  $\text{H}_{205}\text{-C}_{560}\text{-C}_3\text{N}_4$  can be a promising room-temperature operational material.



*Figure 5.10 has been removed due to Copyright restrictions*

**Figure 5.10:** Chemisorption measurements of  $\text{H}_{205}\text{-C}_{560}\text{-C}_3\text{N}_4$  from 20 °C to 500 °C, where the sample was pre-charged with 10%  $\text{H}_2\text{+Ar}$  gas at 20, 50 and 100 °C.

#### **5.4.4 Absorption and Desorption Kinetics**

The absorption and desorption kinetics of  $\text{H}_{205}\text{-C}_{560}\text{-C}_3\text{N}_4$  were performed by a sudden exposure of the sample to 3.6 MPa of pure hydrogen and a vacuum condition, respectively. As depicted in Figure 5.11,  $\text{H}_{205}\text{-C}_{560}\text{-C}_3\text{N}_4$  can absorb and desorb hydrogen completely within 1 minute and 2.5 minutes, respectively, implying a swift kinetics. This could be ascribed to the porous structure of  $\text{C}_3\text{N}_4$  tubes, where the reaction sites are saturated by  $\text{H}_2$  and vacated promptly as hydrogen molecules can easily diffuse through the  $\text{C}_3\text{N}_4$  tube walls. The combination of physisorption and chemisorption also contribute to the rapid sorption.

*Figure 5.11 has been removed due to Copyright restrictions*

**Figure 5.11:** Absorption and desorption kinetics of H<sub>2</sub>-C<sub>560</sub>-C<sub>3</sub>N<sub>4</sub>.

## 5.5 Conclusion

In this work, the hydrogen storage properties of N-rich C<sub>3</sub>N<sub>4</sub> tubes have been measured for the first time. The EDS confirmed that the nitrogen content of tubular C<sub>3</sub>N<sub>4</sub> is near or beyond 50 at%. The XRD and FTIR results indicate that the crystal and chemical structure of C<sub>3</sub>N<sub>4</sub> tubes are not changed by the hydrothermal treatment. The hydrogen storage capacities of C<sub>3</sub>N<sub>4</sub> vary with the alternation of surface area. Among all the samples, H<sub>205</sub>-C<sub>560</sub>-C<sub>3</sub>N<sub>4</sub> has the highest reversible H<sub>2</sub> capacity (0.62 wt% at 20 °C) and the highest surface area (148.69 m<sup>2</sup>/g) which is reported as the highest in the up-to date N-rich C<sub>3</sub>N<sub>4</sub> tubes. Based on the extrapolation of absorption capacity at 20 °C, the H<sub>2</sub> capacity can achieve 2.62 wt% under 10 MPa. The absorbed hydrogen can be mostly released at 25 °C and exhausted at 60 °C. The absorption and desorption processes of tubular C<sub>3</sub>N<sub>4</sub> can be completed within several minutes, suggesting a fast refuelling rate which is competitive to that of petrol.

## Chapter 6 Final Remarks and Future Work

### 6.1 Conclusion

This study aims to identify, design, fabricate and test two promising hydrogen storage materials, so as to fulfil different hydrogen storage requirements of Remote Area Power Supply (RAPS), Movable Power Supply (MPS) and automotive applications.  $V_{80}Ti_8Cr_{12}$  alloy was designed as a hydrogen carrier for RAPS and MPS systems. In this work, the chemical compositions of the synthesized alloy were confirmed to be approximate to the design values by inductively coupled plasma spectroscopy, and the homogeneous elemental distribution was supported by energy dispersive X-ray spectroscopy. The hydrogen storage properties of  $V_{80}Ti_8Cr_{12}$  alloys with six different particle sizes were investigated. The alloys with the particle size below 7 mm exhibited descending hydrogen capacities with the reduction of particle sizes. This could be due to the lattice shrinkage and the increased boundary area caused by mechanical treatment, leading to a decreased number of interstitial sites. In addition, the absorption and desorption kinetics were improved with the particle refinement, while the hydrogen-embrittled samples have a better performance than the milled samples. All of the  $V_{80}Ti_8Cr_{12}$  samples have shown impressive stability in terms of cycle life, where only 10 % capacity loss was detected after 500 cycles of hydrogenation and dehydrogenation. Among the selected specimens, the alloy with 5 mm particle size has the highest usable hydrogen storage capacity of 2.05 wt% (maximum capacity: 3.5 wt%), under the conditions: temperature = 20~50 °C, and pressure 0.2-2 MPa. These conditions satisfied the operation requirements of RAPS and MPS systems. Furthermore, the hydrogen desorption rate of 5 mm  $V_{80}Ti_8Cr_{12}$  alloy (0.129 (g/s)/kW) is nine times faster than that required by the fuel cell (0.014 (g/s)/kW), and it

increases to 12 times faster after 500 cycles (0.167 (g/s)/kW) because of the particle pulverization.

C<sub>3</sub>N<sub>4</sub> tubes were selected as the hydrogen storage materials for automotive applications. They were synthesized by a facile method adopting the hydrothermal treatment and pyrolysis of sole melamine. In the hydrothermal process, the formation of rod-like melamine cyanurate was promoted by higher temperature and reaction surface, and lower solution concentration and filling ratio. The crystal and chemical structures of melamine cyanurate were confirmed by X-ray diffraction and Fourier transform infrared spectrum. With respect to the pyrolysis, it was affected by many factors, including sample amount, sample grinding, crucible airtightness, furnace type, partition, heating duration and heating temperature. The optimum parameters of hydrothermal treatment and pyrolysis are concluded as the followings. 10 % of melamine solution with 85 % of filling ratio was heated at 205 °C for 24 hours, followed by a pyrolysis in a sealed crucible with alumina partitions under 560 °C in air for 4 hours with 5 °C/minute of ramping rate. Under these conditions, the purity of C<sub>3</sub>N<sub>4</sub> tubes was estimated to reach ~80% out of the total product.

The hydrogen storage performance of C<sub>3</sub>N<sub>4</sub> tubes was studied for the first time and other related properties were examined. The energy dispersive X-ray ascertained the tubular carbon nitrides were rich in nitrogen up to around 50 at%. The crystal and chemical structures of C<sub>3</sub>N<sub>4</sub> tubes were characterized to be the same as graphitic carbon nitrides, suggesting the treatments only changed the morphology of the materials. The hydrogen storage capacities of tubular carbon nitrides were much improved with the increase of surface area. Even though the purity of C<sub>3</sub>N<sub>4</sub> tubes still needed to be improve, the optimized hydrogen capacity achieved in this work was 0.62 wt% at 3.6 MPa. This value corresponded to a surface area of 148.69 m<sup>2</sup>/g, which is by far the highest record for N-

rich  $C_3N_4$  tubes. The hydrogen capacity was predicted to reach 2.62 wt% at 10 MPa. Moreover,  $C_3N_4$  tubes have a swift charge and discharge speed, which allows the refuelling to be completed within 2-3 minutes. Last but not least, the special thermal dynamics enables  $C_3N_4$  tubes to absorb and desorb hydrogen at ambient conditions.

The outcomes of this work offer two highly promising hydrogen materials for used in different areas of hydrogen storage for fuel cells. In RAPS and MPS systems, V-based alloy can be an ideal hydrogen carrier because of its low operating pressure, which is easy to be charged by electrolyzers, and reasonable capacity (2 wt%). As for the automotive field, a much higher  $H_2$  capacity (5.5 wt%) is required, so tubular  $C_3N_4$  could be a promising candidate to achieve the  $H_2$  capacity target within a low pressure range (a few MPa) compared to that of high-pressure tank (70 MPa). In addition to the researches on the hydrogen storage materials, a novel approach was developed to precisely measure the hydrogen capacity at various absorption/desorption temperatures. It is more time-saving than the traditional pressure-composition-isotherm.

## 6.2 Future Work

Although  $V_{80}Ti_8Cr_{12}$  alloy has already met the requirements of RAPS and MPS in terms of hydrogen storage capacity and hydrogen supply rate, there are still rooms to improve its performance, as the followings. First, more charge-discharge cycles can be carried out to investigate the durability of  $V_{80}Ti_8Cr_{12}$  alloy under long-term cycles. Second, a working environment, which approximates to a real MPS system, should be constructed to study the cycle stability of  $V_{80}Ti_8Cr_{12}$  alloy under actual service conditions. Third, due to the soaring price of pure vanadium (500 US\$/kg), ferro vanadium (40 US\$/kg) may be applied as a parent alloy in an attempt to lower the cost of  $V_{80}Ti_8Cr_{12}$  alloy. The role of iron in the final product needs to be studied and efforts have to be made to maintain the

superior hydrogen storage performance obtained in this study. Additives and heat/mechanical treatments may be the solutions for maintaining the hydrogen capacity. Fourth, a systematic investigation could be carried out on the hydrogen storage properties of  $V_{80}Ti_8Cr_{12}$  alloy with sample sizes between 5 mm and 7 mm to elucidate the detail performance change in this range. This will include the application of multiple activation processes, surface area measurements and hydrogen absorption kinetic studies. Last but not least, the crystal structures of the  $V_{80}Ti_8Cr_{12}$  samples may be measured in a hydrogen-charging condition using in-situ XRD or neutron diffraction, so as to study the lattice difference before and after hydrogen absorption.

Since  $C_3N_4$  tubes so far cannot perfectly satisfy the requirements of automotive applications (5.5 wt% of  $H_2$  capacity at 0.5-1.2 MPa), more efforts are needed for the development of this material, as suggested in the followings. First, instead of only 4 MPa at the moment, a higher  $H_2$  pressure, e.g. 10-20 MPa, should be implemented to study the hydrogenation behaviours of  $C_3N_4$  tubes at this higher  $H_2$  loading. It could be expected that the hydrogen storage capacity could increase with increasing hydrogenation pressure. Second, the reduction of  $C_3N_4$  tube diameter should be considered to enhance the surface area of tubes. Third, the doping of catalysts on  $C_3N_4$  tubes could be a useful approach to induce spillover effect, and thereby improves the hydrogen capacity under ambient conditions. Fourth, the mass production of  $C_3N_4$  tubes should be developed to fulfil the large material quantity required in automotive hydrogen tanks. Fifth, the cycle stability of  $C_3N_4$  tubes should be tested to ensure it is capable to sustain the repeated hydrogen charge and discharge. Sixth, the sorption mechanism (chemisorption or physisorption) needs to be studied to determine the optimum operating conditions.

It is believed that these two hydrogen storage materials, V-Ti-Cr alloys and  $C_3N_4$  tubes, are the promising hydrogen carriers to break the bottleneck of hydrogen economy as long as the restraints are all well resolved.

## References

- [1] Gray EM, Webb CJ, Andrews J, Shabani B, Tsai PJ, Chan SLI. Hydrogen storage for off-grid power supply. *Int J Hydrogen Energy*. 2011;36:654-63.
- [2] Morton O. Solar energy: A new day dawning?: Silicon Valley sunrise. *Nature*. 2006;443:19-22.
- [3] Dell RM, Rand DAJ. Energy storage - a key technology for global energy sustainability. *J Power Sources*. 2001;100:2-17.
- [4] Bielman M, Vogt UF, Zimmermann M, Züttel A. Seasonal energy storage system based on hydrogen for self sufficient living. *J Power Sources*. 2011;196:4054-60.
- [5] López González E, Isorna Llerena F, Silva Pérez M, Rosa Iglesias F, Guerra Macho J. Energy evaluation of a solar hydrogen storage facility: Comparison with other electrical energy storage technologies. *Int J Hydrogen Energy*. 2015;40:5518-25.
- [6] Luo X, Wang J, Dooner M, Clarke J. Overview of current development in electrical energy storage technologies and the application potential in power system operation. *Applied Energy*. 2015;137:511-36.
- [7] Ural Z, Gencoglu MT. Design and simulation of a solar-hydrogen system for different situations. *Int J Hydrogen Energy*. 2014;39:8833-40.
- [8] Hosseini M, Dincer I, Rosen MA. Hybrid solar–fuel cell combined heat and power systems for residential applications: Energy and exergy analyses. *J Power Sources*. 2013;221:372-80.
- [9] Richards BS, Conibeer GJ. A comparison of hydrogen storage technologies for solar-powered stand-alone power supplies: A photovoltaic system sizing approach. *Int J Hydrogen Energy*. 2007;32:2712-8.
- [10] Nasri S, Sami BS, Cherif A. Power management strategy for hybrid autonomous power system using hydrogen storage. *Int J Hydrogen Energy*. 2016;41:857-65.
- [11] Züttel A. Materials for hydrogen storage. *Materials Today*. 2003;6:24-33.
- [12] A collaboration with RMIT University to develop and demonstrate a low signature, rechargeable and portable energy supply using a reversible hydrogen fuel cell, <https://www.rmit.edu.au/news/all-news/2014/may/silent-renewable-hydrogen-power-for-defence> [accessed 11.03.2018].
- [13] US department of energy. DOE Targets for onboard hydrogen storage for light-duty fuel cell vehicles by 2025, <https://www.energy.gov/eere/fuelcells/doe-technical-targets-onboard-hydrogen-storage-light-duty-vehicles> [accessed 11.03.2018].
- [14] Klebanoff L. Hydrogen Storage Technology: Materials and Applications. CRC



Press; 2012. p. 123-6.

- [15] Yan Y, Chen Y, Liang H, Zhou X, Wu C, Tao M, et al. Hydrogen storage properties of V–Ti–Cr–Fe alloys. *J Alloys Compd.* 2008;454:427-31.
- [16] Akiba E, Okada M. Metallic Hydrides III: Body-Centered-Cubic Solid-Solution Alloys. *MRS Bulletin.* 2002;27:699-703.
- [17] Akiba E, Iba H. Hydrogen absorption by Laves phase related BCC solid solution. *Intermetallics.* 1998;6:461-70.
- [18] Young K, Fetcenko MA, Ouchi T, Im J, Ovshinsky SR, Li F, et al. Hydrogen storage materials having excellent kinetics, capacity, and cycle stability. 2008;US 7344676 B2(Patent).
- [19] Huang B, Ovshinsky SR. Hydrogen storage alloys providing for the reversible storage of hydrogen at low temperatures. 2006;US 7108757 B2(Patent).
- [20] Sapru K, Tan Z, Bazzi M, Ramachandran S, Ovshinsky SR. High capacity transition metal based hydrogen storage materials for the reversible storage of hydrogen. 2003;US 6616891 B1(Patent).
- [21] Koh G, Zhang Y-W, Pan H. First-principles study on hydrogen storage by graphitic carbon nitride nanotubes. *Int J Hydrogen Energy.* 2012;37:4170-8.
- [22] Sankaran M, Viswanathan B. Nitrogen-containing carbon nanotubes as a possible hydrogen storage medium. *Indian Journal of Chemistry.* 2008;47A:808-14.
- [23] Chen L, Xia K, Huang L, Li L, Pei L, Fei S. Facile synthesis and hydrogen storage application of nitrogen-doped carbon nanotubes with bamboo-like structure. *Int J Hydrogen Energy.* 2013;38:3297-303.
- [24] Sharma A, Dasgupta K, Banerjee S, Patwardhan A, Srivastava D, Joshi JB. In-situ nitrogen doping in carbon nanotubes using a fluidized bed reactor and hydrogen storage behavior of the doped nanotubes. *Int J Hydrogen Energy.* 2017;42:10047-56.
- [25] Sir Samuel Griffith Centre. <http://www.griffith.edu.au/about-griffith/campuses/nathan-campus/facilities/sir-samuel-griffith-building> [accessed 12.03.2018].
- [26] Harries DN, Paskevicius M, Sheppard DA, Price TEC, Buckley CE. Concentrating Solar Thermal Heat Storage Using Metal Hydrides. *Proceedings of the IEEE.* 2012;100:539-49.
- [27] Corgnale C, Hardy B, Motyka T, Zidan R, Teprovich J, Peters B. Screening analysis of metal hydride based thermal energy storage systems for concentrating solar power plants. *Renewable and Sustainable Energy Reviews.* 2014;38:821-33.
- [28] Genç G, Çelik M, Serdar Genç M. Cost analysis of wind-electrolyzer-fuel cell system for energy demand in Pınarbaşı-Kayseri. *Int J Hydrogen Energy.* 2012;37:12158-66.
- [29] University R. Silent renewable hydrogen power for defence,

<https://www.rmit.edu.au/news/all-news/2014/may/silent-renewable-hydrogen-power-for-defence> [accessed 12.03.2018].

- [30] Andrews J. The poster of "Development and demonstration of a low signature, rechargeable and portable energy supply using a reversible hydrogen fuel cells" from RMIT University.
- [31] Ulmer U, Dieterich M, Pohl A, Dittmeyer R, Linder M, Fichtner M. Study of the structural, thermodynamic and cyclic effects of vanadium and titanium substitution in laves-phase AB<sub>2</sub> hydrogen storage alloys. *Int J Hydrogen Energy*. 2017;42:20103-10.
- [32] Tesla Motors, [https://www.tesla.com/en\\_AU/?redirect=no](https://www.tesla.com/en_AU/?redirect=no) [accessed 13.03.2018].
- [33] Ni M, Leung MKH, Sumathy K, Leung DY. Potential of renewable hydrogen production for energy supply in Hong Kong. *Int J Hydrogen Energy*. 2006;31:1401-12.
- [34] Wilberforce T, Alaswad A, Palumbo A, Dassisti M, Olabi AG. Advances in stationary and portable fuel cell applications. *Int J Hydrogen Energy*. 2016;41:16509-22.
- [35] James BD, Moton JM, Colella WG. Hydrogen Storage Cost Analysis. US Department of Energy's (DOE's) 2013 Annual Merit Review and Peer Evaluation Meeting (AMR) for the Hydrogen and Fuel Cell Technologies (FCT) Program. 2013.
- [36] Harada M, Ichikawa T, Takagi H, Uchida H. Building a hydrogen infrastructure in Japan. In: Basile A, Veziroğlu TN, editors. *Compendium of Hydrogen Energy*. Oxford: Woodhead Publishing; 2016. p. 321-35.
- [37] Toyota Mirai Hydrogen Fuel Cell Vehicle, <https://ssl.toyota.com/mirai/fcv.html> [accessed 14.03.2018].
- [38] Schlapbach L, Züttel A. Hydrogen-storage materials for mobile applications. *Nature*. 2001;414:353-8.
- [39] Dutta S. A review on production, storage of hydrogen and its utilization as an energy resource. *Journal of Industrial and Engineering Chemistry*. 2014;20:1148-56.
- [40] Sakintuna B, Lamari-Darkrim F, Hirscher M. Metal hydride materials for solid hydrogen storage: A review. *Int J Hydrogen Energy*. 2007;32:1121-40.
- [41] Mito T, Kawagoe A, Yanagi N, Hamaguchi S, Takada S, Hirano N, et al. Highly Efficient Liquid Hydrogen Storage System by Magnetic Levitation Using HTS Coils. *IEEE Transactions on Applied Superconductivity*. 2017;27:1-5.
- [42] Mori D, Hirose K. Recent challenges of hydrogen storage technologies for fuel cell vehicles. *Int J Hydrogen Energy*. 2009;34:4569-74.
- [43] Krainz G, Hodl P, Hofmeister F. Automotive Production of Liquid Hydrogen

Storage Systems. The International German Hydrogen Energy Congress. Essen2004.

- [44] Xu W, Li Q, Huang M. Design and analysis of liquid hydrogen storage tank for high-altitude long-endurance remotely-operated aircraft. *Int J Hydrogen Energy*. 2015;40:16578-86.
- [45] Lim KL, Kazemian H, Yaakob Z, Daud WRW. Solid-state Materials and Methods for Hydrogen Storage: A Critical Review. *Chem Eng Technol*. 2010;33:213-26.
- [46] Dillon AC, Jones KM, Bekkedahl TA, Kiang CH, Bethune DS, Heben MJ. Storage of hydrogen in single-walled carbon nanotubes. *Nature*. 1997;386:377-9.
- [47] Hirscher M, Becher M, Haluska M, von Zeppelin F, Chen X, Dettlaff-Weglikowska U, et al. Are carbon nanostructures an efficient hydrogen storage medium? *J Alloys Compd*. 2003;356–357:433-7.
- [48] Darkrim FL, Malbrunot P, Tartaglia GP. Review of hydrogen storage by adsorption in carbon nanotubes. *Int J Hydrogen Energy*. 2002;27:193-202.
- [49] Zubizarreta L, Gomez EI, Arenillas A, Ania CO, Parra JB, Pis JJ. H<sub>2</sub> storage in carbon materials. *Adsorption*. 2008;14:557-66.
- [50] Bogdanović B, Schwickardi M. Ti-doped alkali metal aluminium hydrides as potential novel reversible hydrogen storage materials. *J Alloys Compd*. 1997;253–254:1-9.
- [51] Chandra D. Intermetallics for hydrogen storage. In: Walker G, editor. *Solid-State Hydrogen Storage*. Woodhead Publishing; 2008. p. 315-56.
- [52] Sandrock G. A panoramic overview of hydrogen storage alloys from a gas reaction point of view. *J Alloys Compd*. 1999;293–295:877-88.
- [53] Nakamura Y, Akiba E. Hydriding properties and crystal structure of NaCl-type mono-hydrides formed from Ti–V–Mn BCC solid solutions. *J Alloys Compd*. 2002;345:175-82.
- [54] Rusman NAA, Dahari M. A review on the current progress of metal hydrides material for solid-state hydrogen storage applications. *Int J Hydrogen Energy*. 2016;41:12108-26.
- [55] Cuevas F, Joubert J-M, Latroche M, Percheron-Guégan A. Intermetallic compounds as negative electrodes of Ni/MH batteries. *Appl Phys A*. 2001;72:225-38.
- [56] Van Vucht JHN, Kuijpers FA, Bruning HCAM. Reversible room-temperature absorption of large quantities of hydrogen by intermetallic compounds. *Philips Research Reports*. 1970;25:133-40.
- [57] Adzic GD, Johnson JR, Reilly JJ, McBreen J, Mukerjee S, Sridhar Kumar MP, et al. Cerium Content and Cycle Life of Multicomponent AB<sub>5</sub> Hydride Electrodes. *Journal of The Electrochemical Society*. 1995;142:3429-33.

- [58] Maurel F, Leblanc P, Knosp B, Backhaus-Ricoult M. Effect of yttrium on the corrosion of AB<sub>5</sub>-type alloys for nickel–metal hydride batteries. *J Alloys Compd.* 2000;309:88-94.
- [59] Valøen LO, Zaluska A, Zaluski L, Tanaka H, Kuriyama N, Ström-Olsen JO, et al. Structure and related properties of (La,Ce,Nd,Pr)Ni<sub>5</sub> alloys. *J Alloys Compd.* 2000;306:235-44.
- [60] Wang LB, Yuan HT, Wang YJ, Yang HB, Li QD, Lin YN, et al. Effect of Zn on the hydrogen storage characteristics of multi-component AB<sub>5</sub>-type alloys. *J Alloys Compd.* 2001;319:242-6.
- [61] Hara T, Yasuda N, Takeuchi Y, Sakai T, Uchiyama A, Miyamura H, et al. New Binding Materials for Metal Hydride Electrodes which Permit Good Recycleability. *Journal of The Electrochemical Society.* 1993;140:2450-4.
- [62] Notten PHL, Einerhand REF, Daams JLC. On the nature of the electrochemical cycling stability of non-stoichiometric LaNi<sub>5</sub>-based hydride-forming compounds Part I. crystallography and electrochemistry. *J Alloys Compd.* 1994;210:221-32.
- [63] Choi J, Park C-N. Performance of metal hydride electrodes with organosilicon as a binder. *J Alloys Compd.* 1995;217:25-8.
- [64] Chen L, Wu F, Tong M, Chen DM, Long RB, Shang ZQ, et al. Advanced nanocrystalline Zr-based AB<sub>2</sub> hydrogen storage electrode materials for NiMH EV batteries. *J Alloys Compd.* 1999;293-295:508-20.
- [65] Young K, Ouchi T, Huang B, Chao B, Fetcenko MA, Bendersky LA, et al. The correlation of C14/C15 phase abundance and electrochemical properties in the AB<sub>2</sub> alloys. *J Alloys Compd.* 2010;506:841-8.
- [66] Manickam K, Grant DM, Walker GS. Optimization of AB<sub>2</sub> type alloy composition with superior hydrogen storage properties for stationary applications. *Int J Hydrogen Energy.* 2015;40:16288-96.
- [67] US Department of Energy. Hydrogen Storage Materials Database, <http://hydrogenmaterialssearchgovtoolsus/HistoricalSearchResults.aspx> [accessed 17.03. 2018].
- [68] Young K, Wong DF, Wang L. Effect of Ti/Cr content on the microstructures and hydrogen storage properties of Laves phase-related body-centered-cubic solid solution alloys. *J Alloys Compd.* 2015;622:885-93.
- [69] Wu E, Li W, Li J. Extraordinary catalytic effect of Laves phase Cr and Mn alloys on hydrogen dissociation and absorption. *Int J Hydrogen Energy.* 2012;37:1509-17.
- [70] Kumar V, Pukazhselvan D, Tyagi AK, Singh SK. Effect of Ni concentration on the structural and hydrogen storage characteristics of Zr–Mn based laves phase system. *Materials for Renewable and Sustainable Energy.* 2013;2:12.

- [71] Wu T, Xue X, Zhang T, Hu R, Kou H, Li J. Effect of MWCNTs on hydrogen storage properties of a Zr-based Laves phase alloy. *Int J Hydrogen Energy*. 2016;41:4168-76.
- [72] Hanada N, Asada H, Nakagawa T, Higa H, Ishida M, Heshiki D, et al. Effect of CO<sub>2</sub> on hydrogen absorption in Ti-Zr-Mn-Cr based AB<sub>2</sub> type alloys. *J Alloys Compd*. 2017;705:507-16.
- [73] Dunlap BD, Viccaro PJ, Shenoy GK. Structural relationships in rare earth-transition metal hydrides. *Journal of the Less Common Metals*. 1980;74:75-9.
- [74] Chen J, Takeshita HT, Tanaka H, Kuriyama N, Sakai T, Uehara I, et al. Hydriding properties of LaNi<sub>3</sub> and CaNi<sub>3</sub> and their substitutes with PuNi<sub>3</sub>-type structure. *J Alloys Compd*. 2000;302:304-13.
- [75] Takeshita T, Wallace WE, Craig RS. Hydrogen solubility in 1:5 compounds between yttrium or thorium and nickel or cobalt. *Inorg Chem*. 1974;13:2282-3.
- [76] Bechman CA, Goudy A, Takeshita T, Wallace WE, Craig RS. Solubility of hydrogen in intermetallics containing rare earth and 3d transition metals. *Inorg Chem*. 1976;15:2184-7.
- [77] Oesterreicher H, Clinton J, Bittner H. Hydrides of La-Ni compounds. *Materials Research Bulletin*. 1976;11:1241-7.
- [78] Oesterreicher H, Ensslen K, Kerlin A, Bucher E. Hydriding behavior in Ca/1bMg/1bNi/1bB. *Materials Research Bulletin*. 1980;15:275-83.
- [79] Kadir K, Kuriyama N, Sakai T, Uehara I, Eriksson L. Structural investigation and hydrogen capacity of CaMg<sub>2</sub>Ni<sub>9</sub>: a new phase in the AB<sub>2</sub>C<sub>9</sub> system isostructural with LaMg<sub>2</sub>Ni<sub>9</sub>. *J Alloys Compd*. 1999;284:145-54.
- [80] Kadir K, Sakai T, Uehara I. Structural investigation and hydrogen capacity of YMg<sub>2</sub>Ni<sub>9</sub> and (Y<sub>0.5</sub>Ca<sub>0.5</sub>)(MgCa)Ni<sub>9</sub>: new phases in the AB<sub>2</sub>C<sub>9</sub> system isostructural with LaMg<sub>2</sub>Ni<sub>9</sub>. *J Alloys Compd*. 1999;287:264-70.
- [81] Kadir K, Sakai T, Uehara I. Structural investigation and hydrogen storage capacity of LaMg<sub>2</sub>Ni<sub>9</sub> and (La<sub>0.65</sub>Ca<sub>0.35</sub>)(Mg<sub>1.32</sub>Ca<sub>0.68</sub>)Ni<sub>9</sub> of the AB<sub>2</sub>C<sub>9</sub> type structure. *J Alloys Compd*. 2000;302:112-7.
- [82] Lim KL, Liu YN, Zhang QA, Chan SLI. Effects of partial substitutions of cerium and aluminum on the hydrogenation properties of La<sub>(0.65-x)</sub>Ce<sub>x</sub>Ca<sub>1.03</sub>Mg<sub>1.32</sub>Ni<sub>(9-y)</sub>Al<sub>y</sub> alloy. *Int J Hydrogen Energy*. 2014;39:10537-45.
- [83] Lim KL, Liu Y, Zhang Q-A, Lin K-S, Chan SLI. Cycle stability of La-Mg-Ni based hydrogen storage alloys in a gas-solid reaction. *Int J Hydrogen Energy*. 2017;42:23737-45.
- [84] Lim KL, Liu Y, Zhang Q-A, Lin K-S, Chan SLI. Cycle stability improvement of La-Mg-Ni based alloys via composite method. *J Alloys Compd*. 2016;661:274-81.

- [85] Leng H, Yu Z, Yin J, Li Q, Wu Z, Chou K-C. Effects of Ce on the hydrogen storage properties of  $\text{TiFe}_{0.9}\text{Mn}_{0.1}$  alloy. *Int J Hydrogen Energy*. 2017;42:23731-6.
- [86] Zadorozhnyy VY, Milovzorov GS, Klyamkin SN, Zadorozhnyy MY, Strugova DV, Gorshenkov MV, et al. Preparation and hydrogen storage properties of nanocrystalline TiFe synthesized by mechanical alloying. *Progress in Natural Science: Materials International*. 2017;27:149-55.
- [87] Révész Á, Gajdics M, Schafler E, Calizzi M, Pasquini L. Dehydrogenation-hydrogenation characteristics of nanocrystalline  $\text{Mg}_2\text{Ni}$  powders compacted by high-pressure torsion. *J Alloys Compd*. 2017;702:84-91.
- [88] Balcerzak M, Jakubowicz J, Kachlicki T, Jurczyk M. Hydrogenation properties of nanostructured  $\text{Ti}_2\text{Ni}$ -based alloys and nanocomposites. *J Power Sources*. 2015;280:435-45.
- [89] Liu J, Han S, Li Y, Zhang J, Zhao Y, Che L. Effect of crystal transformation on electrochemical characteristics of La–Mg–Ni-based alloys with  $\text{A}_2\text{B}_7$ -type super-stacking structures. *Int J Hydrogen Energy*. 2013;38:14903-11.
- [90] Liang G, Schulz R. Phase structures and hydrogen storage properties of Ca–Mg–Ni alloys prepared by mechanical alloying. *J Alloys Compd*. 2003;356-357:612-6.
- [91] Wu C, Zheng X, Chen Y, Tao M, Tong G, Zhou J. Hydrogen storage and cyclic properties of  $\text{V}_{60}\text{Ti}_{(21.4+x)}\text{Cr}_{(6.6-x)}\text{Fe}_{12}(0 \leq x \leq 3)$  alloys. *Int J Hydrogen Energy*. 2010;35:8130-5.
- [92] Lototsky MV, Yartys VA, Zavaliy IY. Vanadium-based BCC alloys: phase-structural characteristics and hydrogen sorption properties. *J Alloys Compd*. 2005;404–406:421-6.
- [93] Reilly JJ, Wiswall RH. Higher hydrides of vanadium and niobium. *Inorg Chem*. 1970;9:1678-82.
- [94] Tamura T, Kazumi T, Kamegawa A, Takamura H, Okada M. Protium absorption properties and protide formations of Ti–Cr–V alloys. *J Alloys Compd*. 2003;356–357:505-9.
- [95] Okada M, Kuriwa T, Tamura T, Takamura H, Kamegawa A. Ti–V–Cr b.c.c. alloys with high protium content. *J Alloys Compd*. 2002;330–332:511-6.
- [96] Cho S-W, Han C-S, Park C-N, Akiba E. The hydrogen storage characteristics of Ti–Cr–V alloys. *J Alloys Compd*. 1999;288:294-8.
- [97] Tsukahara M, Takahashi K, Mishima T, Isomura A, Sakai T. Heat-treatment effects of V-based solid solution alloy with TiNi-based network structure on hydrogen storage and electrode properties. *J Alloys Compd*. 1996;243:133-8.
- [98] Maeland AJ, Libowitz GG, Lynch JF, Rak G. Hydride formation rates of B.C.C. group V metals. *Journal of the Less Common Metals*. 1984;104:133-9.

- [99] Ono S, Nomura K, Ikeda Y. The reaction of hydrogen with alloys of vanadium and titanium. *Journal of the Less Common Metals*. 1980;72:159-65.
- [100] Iba H, Akiba E. Hydrogen absorption and modulated structure in Ti–V–Mn alloys. *J Alloys Compd*. 1997;253–254:21-4.
- [101] Iba H, Akiba E. The relation between microstructure and hydrogen absorbing property in Laves phase-solid solution multiphase alloys. *J Alloys Compd*. 1995;231:508-12.
- [102] Aoki M, Towata S, Noritake T, Itoh A, Washio K, Ishikiriya M. Hydrogen storage alloy, preparation process thereof, and hydrogen storage device. 2010;US 2010/0230299 A1(Patent).
- [103] Chao B, Huang B, Gingl F. TARDEC-AES/ECD milestone reports. October 2008, March and September 2009.
- [104] Tamura T, Kazumi T, Kamegawa A, Takamura H, Okada M. Effects of protide structures on hysteresis in Ti–Cr–V protium absorption alloys. *Materials Transactions*. 2002;43:2753-6.
- [105] Itoh H, Arashima H, Kubo K, Kabutomori T, Ohnishi K. Improvement of cyclic durability of BCC structured Ti–Cr–V alloys. *J Alloys Compd*. 2005;404–406:417-20.
- [106] Kuriwa T, Maruyama T, Kamegawa A, Okada M. Effects of V content on hydrogen storage properties of V–Ti–Cr alloys with high desorption pressure. *Int J Hydrogen Energy*. 2010;35:9082-7.
- [107] Luo L, Wu C, Yang S, Zhou J, Chen Y, Yang F, et al. Decaying behaviors of  $V_{40}(TiCr)_{51}Fe_8Mn$  hydrogen storage alloys with different particle sizes. *J Alloys Compd*. 2015;645:S178-S83.
- [108] Cho S-W, Yoo J-H, Chang H-K, Kim W-B, Kil D-S, Ahn J-G. Changes in the microstructure and hydrogen storage properties of Ti–Cr–V alloys by ball milling and heat treatment. *J Alloys Compd*. 2011;509:5545-50.
- [109] Kwon H, Yoo JH, Roh KM, Suh CY, Kim WB, Cho SW. Effect of particle size and microstructure on the hydrogen storage property in a V–Ti–Cr solid solution system. *J Alloys Compd*. 2012;535:87-90.
- [110] Shirasaki K, Tamura T, Kuriwa T, Goto T, Kamegawa A, Takamura H, et al. Cyclic properties of protium absorption-desorption in Ti–Cr–V alloys. *Materials Transactions*. 2002;43:1115-9.
- [111] Aoki M, Noritake T, Ito A, Ishikiriya M, Towata S. Improvement of cyclic durability of Ti–Cr–V alloy by Fe substitution. *Int J Hydrogen Energy*. 2011;36:12329-32.
- [112] Yoo JH, Shim G, Cho SW, Park CN. Effects of desorption temperature and substitution of Fe for Cr on the hydrogen storage properties of  $Ti_{0.32}Cr_{0.43}V_{0.25}$

- alloy. *Int J Hydrogen Energy*. 2007;32:2977-81.
- [113] Zhou HY, Wang F, Wang J, Wang ZM, Yao QR, Deng JQ, et al. Hydrogen storage properties and thermal stability of  $V_{35}Ti_{20}Cr_{45}$  alloy by heat treatment. *Int J Hydrogen Energy*. 2014;39:14887-95.
  - [114] Shen CC, Li HC. Passivation and reactivation of  $Ti_{25}V_{35}Cr_{40}$  hydrides by cycling with impure hydrogen gas. *Int J Hydrogen Energy*. 2015;40:3277-82.
  - [115] Tamura T, Kamegawa A, Takamura H, Okada M. Protium absorption properties of Ti-Cr-V alloys in low hydrogen pressure regions. *Materials Transactions*. 2001;42:1862-5.
  - [116] Tamura T, Kamegawa A, Takamura H, Okada M. Effects of compositions on formation of 1,2 protorides in Ti-Cr-V alloys. *Materials Transactions*. 2002;43:410-3.
  - [117] Cho SW, Shim G, Choi GS, Park CN, Yoo JH, Choi J. Hydrogen absorption-desorption properties of  $Ti_{0.32}Cr_{0.43}V_{0.25}$  alloy. *J Alloys Compd*. 2007;430:136-41.
  - [118] Liu XP, Cuevas F, Jiang LJ, Latroche M, Li ZN, Wang SM. Improvement of the hydrogen storage properties of Ti-Cr-V-Fe BCC alloy by Ce addition. *J Alloys Compd*. 2009;476:403-7.
  - [119] Yoo J-H, Shim G, Park C-N, Kim W-B, Cho S-W. Influence of Mn or Mn plus Fe on the hydrogen storage properties of the Ti-Cr-V alloy. *Int J Hydrogen Energy*. 2009;34:9116-21.
  - [120] González AS, Plaza MG, Rubiera F, Pevida C. Sustainable biomass-based carbon adsorbents for post-combustion  $CO_2$  capture. *Chemical Engineering Journal*. 2013;230:456-65.
  - [121] Yuan B, Wu X, Chen Y, Huang J, Luo H, Deng S. Adsorption of  $CO_2$ ,  $CH_4$ , and  $N_2$  on Ordered Mesoporous Carbon: Approach for Greenhouse Gases Capture and Biogas Upgrading. *Environmental Science & Technology*. 2013;47:5474-80.
  - [122] Gil MV, Álvarez-Gutiérrez N, Martínez M, Rubiera F, Pevida C, Morán A. Carbon adsorbents for  $CO_2$  capture from bio-hydrogen and biogas streams: Breakthrough adsorption study. *Chemical Engineering Journal*. 2015;269:148-58.
  - [123] Sethupathi S, Bashir MJ, Akbar ZA, Mohamed AR. Biomass-based palm shell activated carbon and palm shell carbon molecular sieve as gas separation adsorbents. *Waste Management & Research*. 2015;33:303-12.
  - [124] Wu Y-J, Yang Y, Kong X-M, Li P, Yu J-G, Ribeiro AM, et al. Adsorption of Pure and Binary  $CO_2$ ,  $CH_4$ , and  $N_2$  Gas Components on Activated Carbon Beads. *Journal of Chemical & Engineering Data*. 2015;60:2684-93.
  - [125] Zhang T, Fan LT, Walawender WP, Fan M, Bland AE, Zuo T, et al. Chapter 7 - Hydrogen Storage on Carbon Adsorbents: A Review. *Environanotechnology*. Amsterdam: Elsevier; 2010. p. 137-63.



- [126] Ren J, Musyoka NM, Langmi HW, Mathe M, Liao S. Current research trends and perspectives on materials-based hydrogen storage solutions: A critical review. *Int J Hydrogen Energy*. 2017;42:289-311.
- [127] Broom DP, Webb CJ, Hurst KE, Parilla PA, Gennett T, Brown CM, et al. Outlook and challenges for hydrogen storage in nanoporous materials. *Appl Phys A*. 2016;122:151.
- [128] Adeniran B, Mokaya R. Low temperature synthesized carbon nanotube superstructures with superior CO<sub>2</sub> and hydrogen storage capacity. *Journal of Materials Chemistry A*. 2015;3:5148-61.
- [129] Yang SJ, Jung H, Kim T, Park CR. Recent advances in hydrogen storage technologies based on nanoporous carbon materials. *Progress in Natural Science: Materials International*. 2012;22:631-8.
- [130] Su DS, Centi G. A perspective on carbon materials for future energy application. *Journal of Energy Chemistry*. 2013;22:151-73.
- [131] Frost H, Düren T, Snurr RQ. Effects of Surface Area, Free Volume, and Heat of Adsorption on Hydrogen Uptake in Metal–Organic Frameworks. *The Journal of Physical Chemistry B*. 2006;110:9565-70.
- [132] Frost H, Snurr RQ. Design Requirements for Metal-Organic Frameworks as Hydrogen Storage Materials. *The Journal of Physical Chemistry C*. 2007;111:18794-803.
- [133] Suh MP, Park HJ, Prasad TK, Lim D-W. Hydrogen Storage in Metal–Organic Frameworks. *Chemical Reviews*. 2012;112:782-835.
- [134] Bhatia SK, Myers AL. Optimum Conditions for Adsorptive Storage. *Langmuir*. 2006;22:1688-700.
- [135] Rowsell JLC, Yaghi OM. Strategies for Hydrogen Storage in Metal–Organic Frameworks. *Angewandte Chemie International Edition*. 2005;44:4670-9.
- [136] Zhou W, Wu H, Hartman MR, Yildirim T. Hydrogen and Methane Adsorption in Metal–Organic Frameworks: A High-Pressure Volumetric Study. *The Journal of Physical Chemistry C*. 2007;111:16131-7.
- [137] Hu X, Skadtchenko BO, Trudeau M, Antonelli DM. Hydrogen Storage in Chemically Reducible Mesoporous and Microporous Ti Oxides. *Journal of the American Chemical Society*. 2006;128:11740-1.
- [138] Muthukumar P, Linder M, Mertz R, Laurien E. Measurement of thermodynamic properties of some hydrogen absorbing alloys. *Int J Hydrogen Energy*. 2009;34:1873-9.
- [139] Robell AJ, Ballou EV, Boudart M. Surface Diffusion of Hydrogen on Carbon. *The Journal of Physical Chemistry*. 1964;68:2748-53.
- [140] Curtis Conner W, Pajonk GM, Teichner SJ. Spillover of Sorbed Species. In: Eley

- DD, Pines H, Weisz PB, editors. *Advances in Catalysis*: Academic Press; 1986. p. 1-79.
- [141] Teichner SJ. Recent studies in hydrogen and oxygen spillover and their impact on catalysis. *Applied Catalysis*. 1990;62:1-10.
  - [142] Pajonk GM. Contribution of spillover effects to heterogeneous catalysis. *Applied Catalysis A: General*. 2000;202:157-69.
  - [143] Conner WC, Falconer JL. Spillover in Heterogeneous Catalysis. *Chemical Reviews*. 1995;95:759-88.
  - [144] Schwarz JA. Metal assisted carbon cold storage of hydrogen. 1988;US 4716736(Patent).
  - [145] Psogianakakis GM, Froudakis GE. DFT Study of the Hydrogen Spillover Mechanism on Pt-Doped Graphite. *The Journal of Physical Chemistry C*. 2009;113:14908-15.
  - [146] Jain P, Fonseca DA, Schaible E, Lueking AD. Hydrogen Uptake of Platinum-Doped Graphite Nanofibers and Stochastic Analysis of Hydrogen Spillover. *The Journal of Physical Chemistry C*. 2007;111:1788-800.
  - [147] Nechaev YS, Veziroglu TN. Mechanism and Energetics of the Unique Spillover Effect Manifestation, Relevance to the Efficient Hydrogen Storage in Graphite Nanofibers. 2015. 2015;7.
  - [148] Nishihara H, Ittisanronnachai S, Itoi H, Li L-X, Suzuki K, Nagashima U, et al. Experimental and Theoretical Studies of Hydrogen/Deuterium Spillover on Pt-Loaded Zeolite-Templated Carbon. *The Journal of Physical Chemistry C*. 2014;118:9551-9.
  - [149] Wang Y, Wang K, Guan C, He Z, Lu Z, Chen T, et al. Surface functionalization-enhanced spillover effect on hydrogen storage of Ni-B nanoalloy-doped activated carbon. *Int J Hydrogen Energy*. 2011;36:13663-8.
  - [150] Geng Z, Wang D, Zhang C, Zhou X, Xin H, Liu X, et al. Spillover enhanced hydrogen uptake of Pt/Pd doped corn-cob-derived activated carbon with ultra-high surface area at high pressure. *Int J Hydrogen Energy*. 2014;39:13643-9.
  - [151] Chung T-Y, Tsao C-S, Tseng H-P, Chen C-H, Yu M-S. Effects of oxygen functional groups on the enhancement of the hydrogen spillover of Pd-doped activated carbon. *Journal of Colloid and Interface Science*. 2015;441:98-105.
  - [152] Back C-K, Sandí G, Prakash J, Hranisavljevic J. Hydrogen Sorption on Palladium-Doped Sepiolite-Derived Carbon Nanofibers. *The Journal of Physical Chemistry B*. 2006;110:16225-31.
  - [153] Contescu CI, Brown CM, Liu Y, Bhat VV, Gallego NC. Detection of Hydrogen Spillover in Palladium-Modified Activated Carbon Fibers during Hydrogen Adsorption. *The Journal of Physical Chemistry C*. 2009;113:5886-90.

- [154] Im JS, Park S-J, Kim T, Lee Y-S. Hydrogen storage evaluation based on investigations of the catalytic properties of metal/metal oxides in electrospun carbon fibers. *Int J Hydrogen Energy*. 2009;34:3382-8.
- [155] Díaz E, León M, Ordóñez S. Hydrogen adsorption on Pd-modified carbon nanofibres: Influence of CNF surface chemistry and impregnation procedure. *Int J Hydrogen Energy*. 2010;35:4576-81.
- [156] Chen C-H, Huang C-C. Enhancement of hydrogen spillover onto carbon nanotubes with defect feature. *Microporous and Mesoporous Materials*. 2008;109:549-59.
- [157] Chen C-Y, Chang J-K, Tsai W-T. Improved hydrogen storage performance of defected carbon nanotubes with Pd spillover catalysts dispersed using supercritical CO<sub>2</sub> fluid. *Int J Hydrogen Energy*. 2012;37:3305-12.
- [158] Juarez-Mosqueda R, Mavrandonakis A, Kuc AB, Pettersson LGM, Heine T. Theoretical analysis of hydrogen spillover mechanism on carbon nanotubes. *Frontiers in Chemistry*. 2015;3:2.
- [159] Li Y, Yang RT. Hydrogen storage in metal-organic and covalent-organic frameworks by spillover. *AIChE Journal*. 2008;54:269-79.
- [160] Zhou H, Zhang J, Zhang J, Yan X-F, Shen X-P, Yuan A-H. Spillover enhanced hydrogen storage in Pt-doped MOF/graphene oxide composite produced via an impregnation method. *Inorganic Chemistry Communications*. 2015;54:54-6.
- [161] Adhikari AK, Lin K-S, Chang C-S. Improved hydrogen storage capacity by hydrogen spillover and fine structural characterization of MIL-100 metal organic frameworks. *Res Chem Intermediat*. 2015;41:7655-67.
- [162] Choi S, Jeong K-j, Park JY, Lee YS. Computational Study of Hydrogen Chemisorption on a Multi-Phenyl Organic Linker as a Model of Hydrogen Spillover on Metal-Organic Frameworks#. *Bulletin of the Korean Chemical Society*. 2015;36:777-83.
- [163] Berlouis LEA, Jubin C, McMillan BG, Morrow J, Spicer MD, Tang LP, et al. Enhanced hydrogen storage in Ni/Ce composite oxides. *Physical Chemistry Chemical Physics*. 2007;9:6032-9.
- [164] Triwahyono S, Jalil AA, Timmiati SN, Ruslan NN, Hattori H. Kinetics study of hydrogen adsorption over Pt/MoO<sub>3</sub>. *Applied Catalysis A: General*. 2010;372:103-7.
- [165] Sun X, Hwang J-Y, Shi S. Hydrogen Storage in Mesoporous Metal Oxides with Catalyst and External Electric Field. *The Journal of Physical Chemistry C*. 2010;114:7178-84.
- [166] Li Y, Yang RT. Hydrogen Storage in Low Silica Type X Zeolites. *The Journal of Physical Chemistry B*. 2006;110:17175-81.

- [167] Jung JH, Rim JA, Lee SJ, Cho SJ, Kim SY, Kang JK, et al. Pd-Doped Double-Walled Silica Nanotubes as Hydrogen Storage Material at Room Temperature. *The Journal of Physical Chemistry C*. 2007;111:2679-82.
- [168] Wang L, Yang RT. Hydrogen Storage Properties of Low-Silica Type X Zeolites. *Industrial & Engineering Chemistry Research*. 2010;49:3634-41.
- [169] Hasell T, Wood CD, Clowes R, Jones JTA, Khimyak YZ, Adams DJ, et al. Palladium Nanoparticle Incorporation in Conjugated Microporous Polymers by Supercritical Fluid Processing. *Chemistry of Materials*. 2010;22:557-64.
- [170] Pyle DS, Gray EM, Webb CJ. Hydrogen storage in carbon nanostructures via spillover. *Int J Hydrogen Energy*. 2016;41:19098-113.
- [171] Wang L, Yang RT. Hydrogen Storage on Carbon-Based Adsorbents and Storage at Ambient Temperature by Hydrogen Spillover. *Catalysis Reviews*. 2010;52:411-61.
- [172] Agarwal RK, Noh JS, Schwarz JA, Davini P. Effect of surface acidity of activated carbon on hydrogen storage. *Carbon*. 1987;25:219-26.
- [173] Comisso N, Berlouis LEA, Morrow J, Pagura C. Changes in hydrogen storage properties of carbon nano-horns submitted to thermal oxidation. *Int J Hydrogen Energy*. 2010;35:9070-81.
- [174] Wang Z, Yang FH, Yang RT. Enhanced Hydrogen Spillover on Carbon Surfaces Modified by Oxygen Plasma. *The Journal of Physical Chemistry C*. 2010;114:1601-9.
- [175] Jeong Y, Mike Chung TC. The synthesis and characterization of a super-activated carbon containing substitutional boron (BC<sub>x</sub>) and its applications in hydrogen storage. *Carbon*. 2010;48:2526-37.
- [176] Ariharan A, Viswanathan B, Nandhakumar V. Hydrogen storage on boron substituted carbon materials. *Int J Hydrogen Energy*. 2016;41:3527-36.
- [177] Mousavipour SH, Chitsazi R. A theoretical study on the effect of intercalating sulfur atom and doping boron atom on the adsorption of hydrogen molecule on (10,0) single-walled carbon nanotubes. *Journal of the Iranian Chemical Society*. 2010;7:S92-S102.
- [178] Lee H. Enhancement of H<sub>2</sub> adsorption on a boron-doped carbon system for hydrogen storage. *Solid State Communications*. 2010;150:1959-62.
- [179] Jeong Y, Chung TCM. Mono-dispersed transition metal nanoparticles on boron-substituted carbon support and applications in hydrogen storage. *Carbon*. 2011;49:140-6.
- [180] Bult JB, Lee J, O'Neill K, Engtrakul C, Hurst KE, Zhao Y, et al. Manipulation of Hydrogen Binding Energy and Desorption Kinetics by Boron Doping of High Surface Area Carbon. *The Journal of Physical Chemistry C*. 2012;116:26138-43.

- [181] Qajar A, Holbrook BM, Peer M, Rajagopalan R, Foley HC, Davis M, et al. Synthesis and characterization of boron substituted carbon deposits on PFA-derived carbon substrates for hydrogen adsorption. *Carbon*. 2015;89:392-403.
- [182] Sethia G, Sayari A. Activated carbon with optimum pore size distribution for hydrogen storage. *Carbon*. 2016;99:289-94.
- [183] Zhu ZH, Hatori H, Wang SB, Lu GQ. Insights into Hydrogen Atom Adsorption on and the Electrochemical Properties of Nitrogen-Substituted Carbon Materials. *The Journal of Physical Chemistry B*. 2005;109:16744-9.
- [184] Wang L, Yang FH, Yang RT. Hydrogen storage properties of B- and N-doped microporous carbon. *AIChE Journal*. 2009;55:1823-33.
- [185] Kong X-K, Chen Q-W, Lun Z-Y. The Influence of N-doped Carbon Materials on Supported Pd: Enhanced Hydrogen Storage and Oxygen Reduction Performance. *ChemPhysChem*. 2014;15:344-50.
- [186] Lin IH, Tong Y-J, Hsieh H-J, Huang H-W, Chen H-T. Hydrogen adsorption and storage in boron-substituted and nitrogen-substituted nano-carbon materials decorated with alkaline earth metals. *Int J Energ Res*. 2016;40:230-40.
- [187] Wang Z, Sun L, Xu F, Zhou H, Peng X, Sun D, et al. Nitrogen-doped porous carbons with high performance for hydrogen storage. *Int J Hydrogen Energy*. 2016;41:8489-97.
- [188] Yang Z, Xia Y, Sun X, Mokaya R. Preparation and Hydrogen Storage Properties of Zeolite-Templated Carbon Materials Nanocast via Chemical Vapor Deposition: Effect of the Zeolite Template and Nitrogen Doping. *The Journal of Physical Chemistry B*. 2006;110:18424-31.
- [189] Xia Y, Walker GS, Grant DM, Mokaya R. Hydrogen Storage in High Surface Area Carbons: Experimental Demonstration of the Effects of Nitrogen Doping. *Journal of the American Chemical Society*. 2009;131:16493-9.
- [190] Wang L, Yang RT. Hydrogen Storage Properties of N-Doped Microporous Carbon. *The Journal of Physical Chemistry C*. 2009;113:21883-8.
- [191] Giraudet S, Zhu Z, Yao X, Lu G. Ordered Mesoporous Carbons Enriched with Nitrogen: Application to Hydrogen Storage. *The Journal of Physical Chemistry C*. 2010;114:8639-45.
- [192] Xia Y, Mokaya R, Grant DM, Walker GS. A simplified synthesis of N-doped zeolite-templated carbons, the control of the level of zeolite-like ordering and its effect on hydrogen storage properties. *Carbon*. 2011;49:844-53.
- [193] Badzian A, Badzian T, Breval E, Piotrowski A. Nanostructured, nitrogen-doped carbon materials for hydrogen storage. *Thin Solid Films*. 2001;398-399:170-4.
- [194] Yang SJ, Cho JH, Oh GH, Nahm KS, Park CR. Easy synthesis of highly nitrogen-enriched graphitic carbon with a high hydrogen storage capacity at room

- temperature. Carbon. 2009;47:1585-91.
- [195] Kim G, Jhi S-H, Park N. Effective metal dispersion in pyridinelike nitrogen doped graphenes for hydrogen storage. Applied Physics Letters. 2008;92:013106.
  - [196] Vinayan BP, Sethupathi K, Ramaprabhu S. Hydrogen storage studies of palladium decorated nitrogen doped graphene nanoplatelets. Journal of nanoscience and nanotechnology. 2012;12:6608-14.
  - [197] Ao ZM, Hernandez-Nieves AD, Peeters FM, Li S. The electric field as a novel switch for uptake/release of hydrogen for storage in nitrogen doped graphene. Physical Chemistry Chemical Physics. 2012;14:1463-7.
  - [198] Parambath VB, Nagar R, Ramaprabhu S. Effect of Nitrogen Doping on Hydrogen Storage Capacity of Palladium Decorated Graphene. Langmuir. 2012;28:7826-33.
  - [199] Lee S, Lee M, Chung Y-C. Enhanced hydrogen storage properties under external electric fields of N-doped graphene with Li decoration. Physical Chemistry Chemical Physics. 2013;15:3243-8.
  - [200] Lee S, Lee M, Choi H, Yoo DS, Chung Y-C. Effect of nitrogen induced defects in Li dispersed graphene on hydrogen storage. Int J Hydrogen Energy. 2013;38:4611-7.
  - [201] Vinayan BP, Nagar R, Ramaprabhu S. Solar light assisted green synthesis of palladium nanoparticle decorated nitrogen doped graphene for hydrogen storage application. Journal of Materials Chemistry A. 2013;1:11192-9.
  - [202] Kim D, Lee S, Jo S, Chung Y-C. Strain effects on hydrogen storage in Ti decorated pyridinic N-doped graphene. Physical Chemistry Chemical Physics. 2013;15:12757-61.
  - [203] Ma L, Zhang J-M, Xu K-W. Hydrogen storage on nitrogen induced defects in palladium-decorated graphene: A first-principles study. Applied Surface Science. 2014;292:921-7.
  - [204] Ariharan A, Viswanathan B, Nandhakumar V. Nitrogen Doped Graphene as Potential Material for Hydrogen Storage. Graphene. 2017;Vol.06No.02:20.
  - [205] Gohari-Bajestani Z, Akhlaghi O, Yürüm Y, Yürüm A. Synthesis of anatase TiO<sub>2</sub> with exposed (001) facets grown on N-doped reduced graphene oxide for enhanced hydrogen storage. Int J Hydrogen Energy. 2017;42:6096-103.
  - [206] Sankaran M, Viswanathan B. The role of heteroatoms in carbon nanotubes for hydrogen storage. Carbon. 2006;44:2816-21.
  - [207] Zhang Z, Cho K. Ab initio study of hydrogen interaction with pure and nitrogen-doped carbon nanotubes. Physical Review B. 2007;75:075420.
  - [208] Kang KY, Lee BI, Lee JS. Hydrogen adsorption on nitrogen-doped carbon xerogels. Carbon. 2009;47:1171-80.

- [209] Jiang J, Gao Q, Zheng Z, Xia K, Hu J. Enhanced room temperature hydrogen storage capacity of hollow nitrogen-containing carbon spheres. *Int J Hydrogen Energy*. 2010;35:210-6.
- [210] Zhang Y, Sun H, Chen C. New template for metal decoration and hydrogen adsorption on graphene-like  $C_3N_4$ . *Physics Letters A*. 2009;373:2778-81.
- [211] Wang Y, Ji Y, Li M, Yuan P, Sun Q, Jia Y. Li and Ca Co-decorated carbon nitride nanostructures as high-capacity hydrogen storage media. *Journal of Applied Physics*. 2011;110:094311.
- [212] Song N, Wang Y, Sun Q, Jia Y. First-principles study of hydrogen storage on Ti (Sc)-decorated boron-carbon-nitride sheet. *Applied Surface Science*. 2012;263:182-6.
- [213] Wu M, Wang Q, Sun Q, Jena P. Functionalized Graphitic Carbon Nitride for Efficient Energy Storage. *The Journal of Physical Chemistry C*. 2013;117:6055-9.
- [214] Tan X, Kou L, Tahini HA, Smith SC. Charge Modulation in Graphitic Carbon Nitride as a Switchable Approach to High-Capacity Hydrogen Storage. *ChemSusChem*. 2015;8:3626-31.
- [215] Nair AAS, Sundara R, Anitha N. Hydrogen storage performance of palladium nanoparticles decorated graphitic carbon nitride. *Int J Hydrogen Energy*. 2015;40:3259-67.
- [216] Hussain T, Hankel M, Searles DJ. Computational Evaluation of Lithium-Functionalized Carbon Nitride (g- $C_6N_8$ ) Monolayer as an Efficient Hydrogen Storage Material. *The Journal of Physical Chemistry C*. 2016;120:25180-8.
- [217] Nair AAS, Sundara R. Palladium Cobalt Alloy Catalyst Nanoparticles Facilitated Enhanced Hydrogen Storage Performance of Graphitic Carbon Nitride. *The Journal of Physical Chemistry C*. 2016;120:9612-8.
- [218] Hussain T, Kaewmaraya T, Hankel M, Amornkitbamrung V. Functionalized carbon nitride (g-CN) monolayer as a promising energy storage material: A density functional theory study. *Applied Surface Science*. 2017;419:708-12.
- [219] Joseph S, Kempaiah D, Benzigar M, Baskar AV, Talapaneni SN, Jung SH, et al. Metal organic framework derived mesoporous carbon nitrides with a high specific surface area and chromium oxide nanoparticles for  $CO_2$  and hydrogen adsorption. *Journal of Materials Chemistry A*. 2017;5:21542-9.
- [220] Yoshiaki O, Shigeo O, Tsuneo S, Kiyoshi Y, Haruhiko I, Hidetoshi S. Hydrogen Storage in Amorphous Phase of Hydrogenated Carbon Nitride. *Japanese Journal of Applied Physics*. 2002;41:7508.
- [221] Yoshiaki O, Ken-ichi K, Shigeo O, Akira H, Minoru T, Hidetoshi S. Hydrogen Storage Phenomenon in Amorphous Phase of Hydrogenated Carbon Nitride.

- Japanese Journal of Applied Physics. 2003;42:5251.
- [222] Ito H, Nozaki T, Saikubo A, Yamada N, Kanda K, Niibe M, et al. Hydrogen-storage characteristics of hydrogenated amorphous carbon nitrides. *Thin Solid Films*. 2008;516:6575-9.
  - [223] Bai XD, Zhong D, Zhang GY, Ma XC, Liu S, Wang EG, et al. Hydrogen storage in carbon nitride nanobells. *Applied Physics Letters*. 2001;79:1552-4.
  - [224] Kim SY, Kim HS, Augustine S, Kang JK. Nanopores in carbon nitride nanotubes: Reversible hydrogen storage sites. *Applied Physics Letters*. 2006;89:253119.
  - [225] Wang YS, Li M, Wang F, Sun Q, Jia Y. Li and Na Co-decorated carbon nitride nanotubes as promising new hydrogen storage media. *Physics Letters A*. 2012;376:631-6.
  - [226] Kang JK, Yang SH, Shin WH, Bae JH. Transition Metal-Carbon Nanotube Hybrid Catalyst Containing Nitrogen, Method for Preparation Thereof, and Method for Generation of Hydrogen Using the Same. 2009;US20090155163A1(Patent).
  - [227] Yang P, Liu Y, Wang J. A method of preparing a carbon nanotube nitride. 2017;CN105217584B(Patent).
  - [228] Yang P, Liu Y, Wang J. Similar tubular borax-doped graphite phase carbon nitride nanometer material and preparation method thereof. 2017;CN106732736A(Patent).
  - [229] Yang P, Liu Y, Wang J. Carbon-doped graphite-phase carbon nitride nanotube and preparation method thereof. 2017;CN106744745A(Patent).
  - [230] Si Y, Zhang Y, Lu L, Zhang S, Chen Y, Liu J, et al. Boosting visible light photocatalytic hydrogen evolution of graphitic carbon nitride via enhancing its interfacial redox activity with cobalt/nitrogen doped tubular graphitic carbon. *Applied Catalysis B: Environmental*. 2018;225:512-8.
  - [231] Devadoss A, Lee JW, Terashima C, Fujishima A, Kim Y-P, Kang JK, et al. Synergistic oxidation of NADH on bimetallic CoPt nanoparticles decorated carbon nitride nanotubes. *Sensors and Actuators B: Chemical*. 2015;208:204-11.
  - [232] Lu X, Wang H, Zhang S, Cui D, Wang Q. Synthesis, characterization and electrocatalytic properties of carbon nitride nanotubes for methanol electrooxidation. *Solid State Sciences*. 2009;11:428-32.
  - [233] Chilukuri SVV, Kanna N, Gurralla L. Selective aerobic oxidations using carbon nitride nanotubes. 2016;US20160304484A1(Patent).
  - [234] Liu Y, Wang X, Zhu D. Array nanotube, mfg method and use thereof. 2004;CN1401560A(Patent).
  - [235] Ghosh K, Kumar M, Wang H, Maruyama T, Ando Y. Facile Decoration of Platinum Nanoparticles on Carbon-Nitride Nanotubes via Microwave-Assisted



- Chemical Reduction and Their Optimization for Field-Emission Application. *The Journal of Physical Chemistry C*. 2010;114:5107-12.
- [236] Zijiong L, Liangming W, Ping L, Yafei Z. Carbon nitride nanotubes synthesized by high-frequency induction heating quickly and their field-emission properties. 2nd IEEE International Nanoelectronics Conference 2008. p. 958-60.
- [237] Bian S-W, Ma Z, Song W-G. Preparation and Characterization of Carbon Nitride Nanotubes and Their Applications as Catalyst Supporter. *The Journal of Physical Chemistry C*. 2009;113:8668-72.
- [238] Hu Z, Ma Y, Yue B, Yu L. Electrode Catalyst of Carbon Nitride Nanotubes Supported by Platinum and Ruthenium Nanoparticles and Preparation Method Thereof. 2011;US20110065570A1(Patent).
- [239] Kang J-K, Lee J-w, Viswan R, Choi Y-j, Lee Y, Kim S-Y. Method for preparation of hybrid comprising magnetite nanoparticles and carbon nitride nanotubes. 2012;US8110255B2(Patent).
- [240] Song CO, Lee JW, Choi HS, Kang JK. Two-step synthesis of agglomeration-free peroxidase-like  $\text{Co}_3\text{O}_4$  nanoparticles-carbon nitride nanotube hybrids enabling a high redox activity. *RSC Advances*. 2013;3:20179-85.
- [241] Gao J, Zhou Y, Li Z, Yan S, Wang N, Zou Z. High-yield synthesis of millimetre-long, semiconducting carbon nitride nanotubes with intense photoluminescence emission and reproducible photoconductivity. *Nanoscale*. 2012;4:3687-92.
- [242] Zhou Y, Zou Z, Gao J. Preparation method for self-assembly carbonitride nanotube and nanotube prepared by using same. 2013;CN102616757A(Patent).
- [243] Wu C, Zhu X, Wang C, Sheng H, Yang J, Xie Y. Bamboolike carbon nitride nanotubes ( $\text{C}_9\text{N}_5\text{H}_3$ ): Atomic-scale construction, synthesis and lithium battery applications. *Applied Physics Letters*. 2007;90:113116.
- [244] Irannejad N, Rezaei B, Ensafi AA, Momeni MM. Enhanced efficiency of dye-sensitized solar cell by using a novel modified photoanode with platinum  $\text{C}_3\text{N}_4$  nanotubes incorporated  $\text{Ag}/\text{TiO}_2$  nanoparticles. *Electrochimica Acta*. 2017;247:764-70.
- [245] Meyer H-J, Gibson K, Ströbele M, Tragl S. Method for producing carbon nitrides in the form of tubes. 2005;WO2005033000A1(Patent).
- [246] Jordan T, Fechner N, Xu J, Brenner TJK, Antonietti M, Shalom M. "Caffeine Doping" of Carbon/Nitrogen-Based Organic Catalysts: Caffeine as a Supramolecular Edge Modifier for the Synthesis of Photoactive Carbon Nitride Tubes. *ChemCatChem*. 2015;7:2826-30.
- [247] Tong Z, Yang D, Sun Y, Nan Y, Jiang Z. Tubular g- $\text{C}_3\text{N}_4$  Isotype Heterojunction: Enhanced Visible-Light Photocatalytic Activity through Cooperative Manipulation of Oriented Electron and Hole Transfer. *Small*. 2016;12:4093-101.

- [248] Sang Y, Guo D, Zhao L, Cai N, Li H, Ma B, et al. A nitride nanotube and preparation method. 2017;CN105883732B(Patent).
- [249] Guo S, Tang Y, Xie Y, Tian C, Feng Q, Zhou W, et al. P-doped tubular g-C<sub>3</sub>N<sub>4</sub> with surface carbon defects: Universal synthesis and enhanced visible-light photocatalytic hydrogen production. *Applied Catalysis B: Environmental*. 2017;218:664-71.
- [250] Liu B, Ye L, Wang R, Yang J, Zhang Y, Guan R, et al. Phosphorus-Doped Graphitic Carbon Nitride Nanotubes with Amino-rich Surface for Efficient CO<sub>2</sub> Capture, Enhanced Photocatalytic Activity, and Product Selectivity. *ACS Applied Materials & Interfaces*. 2017.
- [251] He F, Chen G, Miao J, Wang Z, Su D, Liu S, et al. Sulfur-Mediated Self-Templating Synthesis of Tapered C-PAN/g-C<sub>3</sub>N<sub>4</sub> Composite Nanotubes toward Efficient Photocatalytic H<sub>2</sub> Evolution. *ACS Energy Letters*. 2016;1:969-75.
- [252] Zhang G, Savateev A, Zhao Y, Li L, Antonietti M. Advancing n→ $\pi^*$  electron transition of carbon nitride nanotubes for H<sub>2</sub> photosynthesis. *Journal of Materials Chemistry A*. 2017;5:12723-8.
- [253] Gong J, Li C, Wang T, Zhang P, Zhang J, Wang S. Preparation method of graphite type carbon nitride nanotubes. 2015;CN103601162B(Patent).
- [254] Zeng Z, Li K, Yan L, Dai Y, Guo H, Huo M, et al. Fabrication of carbon nitride nanotubes by a simple water-induced morphological transformation process and their efficient visible-light photocatalytic activity. *RSC Advances*. 2014;4:59513-8.
- [255] Li K, Yan L, Zeng Z, Luo S, Luo X, Liu X, et al. Fabrication of H<sub>3</sub>PW<sub>12</sub>O<sub>40</sub>-doped carbon nitride nanotubes by one-step hydrothermal treatment strategy and their efficient visible-light photocatalytic activity toward representative aqueous persistent organic pollutants degradation. *Applied Catalysis B: Environmental*. 2014;156-157:141-52.
- [256] Yola ML, Atar N. Phenylethanolamine A (PEA) Imprinted Polymer on Carbon Nitride Nanotubes/Graphene Quantum Dots/Core-Shell Nanoparticle Composite for Electrochemical PEA Detection in Urine Sample. *Journal of The Electrochemical Society*. 2018;165:H1-H9.
- [257] Jin Z, Zhang Q, Yuan S, Ohno T. Synthesis high specific surface area nanotube g-C<sub>3</sub>N<sub>4</sub> with two-step condensation treatment of melamine to enhance photocatalysis properties. *RSC Advances*. 2015;5:4026-9.
- [258] Guo S, Deng Z, Li M, Jiang B, Tian C, Pan Q, et al. Phosphorus-Doped Carbon Nitride Tubes with a Layered Micro-nanostructure for Enhanced Visible-Light Photocatalytic Hydrogen Evolution. *Angewandte Chemie International Edition*. 2016;55:1830-4.

- [259] Adhikari SP, Hood ZD, Wang H, Peng R, Krall A, Li H, et al. Enhanced visible light photocatalytic water reduction from a g-C<sub>3</sub>N<sub>4</sub>/SrTa<sub>2</sub>O<sub>6</sub> heterojunction. *Applied Catalysis B: Environmental*. 2017;217:448-58.
- [260] Mo Z, Xu H, Chen Z, She X, Song Y, Wu J, et al. Self-assembled synthesis of defect-engineered graphitic carbon nitride nanotubes for efficient conversion of solar energy. *Applied Catalysis B: Environmental*. 2018;225:154-61.
- [261] Chapman RP, Averell PR, Harris RR. Solubility of Melamine in Water. *Industrial & Engineering Chemistry*. 1943;35:137-8.
- [262] Son JY, Kang YJ, Kim KS, Kim TH, Lim SK, Lim HJ, et al. Evaluation of Renal Toxicity by Combination Exposure to Melamine and Cyanuric Acid in Male Sprague-Dawley Rats. *Toxicological Research*. 2014;30:99-107.
- [263] Bann B, Miller SA. Melamine And Derivatives Of Melamine. *Chemical Reviews*. 1958;58:131-72.
- [264] Liu Y, Wang Q. Melamine cyanurate-microencapsulated red phosphorus flame retardant unreinforced and glass fiber reinforced polyamide 66. *Polymer Degradation and Stability*. 2006;91:3103-9.
- [265] Dobson RLM, Motlagh S, Quijano M, Cambron RT, Baker TR, Pullen AM, et al. Identification and Characterization of Toxicity of Contaminants in Pet Food Leading to an Outbreak of Renal Toxicity in Cats and Dogs. *Toxicological Sciences*. 2008;106:251-62.
- [266] Nagai D, Kuribayashi T, Tanaka H, Morinaga H, Uehara H, Yamanobe T. A facile, selective, high recovery system for precious metals based on complexation between melamine and cyanuric acid. *RSC Advances*. 2015;5:30133-9.
- [267] Shalom M, Inal S, Fettkenhauer C, Neher D, Antonietti M. Improving Carbon Nitride Photocatalysis by Supramolecular Preorganization of Monomers. *Journal of the American Chemical Society*. 2013;135:7118-21.
- [268] Jun Y-S, Lee EZ, Wang X, Hong WH, Stucky GD, Thomas A. From Melamine-Cyanuric Acid Supramolecular Aggregates to Carbon Nitride Hollow Spheres. *Advanced Functional Materials*. 2013;23:3661-7.
- [269] JIS Committee. Method for measurement of pressure-composition-temperature (PCT) relations of hydrogen absorbing alloys. Japanese Standards Association. 2007:1-10.
- [270] Sing KSW. Reporting Physisorption Data for Gas/Solid Systems With Special Reference to the Determination of Surface Area and Porosity. *Pure Appl Chem*. 1982;54:2201.
- [271] Shin WH, Yang SH, Choi YJ, Jung HM, Song CO, Kang JK. Charge polarization-dependent activity of catalyst nanoparticles on carbon nitride nanotubes for hydrogen generation. *Journal of Materials Chemistry*. 2009;19:4505-9.

- [272] Fina F, Callear SK, Carins GM, Irvine JTS. Structural Investigation of Graphitic Carbon Nitride via XRD and Neutron Diffraction. *Chemistry of Materials*. 2015;27:2612-8.
- [273] Wang X, Maeda K, Thomas A, Takanabe K, Xin G, Carlsson JM, et al. A metal-free polymeric photocatalyst for hydrogen production from water under visible light. *Nature materials*. 2009;8:76-80.
- [274] Xu H, Yan J, She X, Xu L, Xia J, Xu Y, et al. Graphene-analogue carbon nitride: novel exfoliation synthesis and its application in photocatalysis and photoelectrochemical selective detection of trace amount of  $\text{Cu}^{2+}$ . *Nanoscale*. 2014;6:1406-15.
- [275] Cheng F, Wang H, Dong X. The amphoteric properties of g- $\text{C}_3\text{N}_4$  nanosheets and fabrication of their relevant heterostructure photocatalysts by an electrostatic re-assembly route. *Chem Commun*. 2015;51:7176-9.
- [276] Ma H, Shi Z, Li Q, Li S. Preparation of graphitic carbon nitride with large specific surface area and outstanding  $\text{N}_2$  photofixation ability via a dissolve-regrowth process. *J Phys Chem Solids*. 2016;99:51-8.
- [277] Yang S, Gong Y, Zhang J, Zhan L, Ma L, Fang Z, et al. Exfoliated Graphitic Carbon Nitride Nanosheets as Efficient Catalysts for Hydrogen Evolution Under Visible Light. *Advanced Materials*. 2013;25:2452-6.
- [278] She X, Xu H, Xu Y, Yan J, Xia J, Xu L, et al. Exfoliated graphene-like carbon nitride in organic solvents: enhanced photocatalytic activity and highly selective and sensitive sensor for the detection of trace amounts of  $\text{Cu}^{2+}$ . *Journal of Materials Chemistry A*. 2014;2:2563-70.
- [279] Zhou M, Hou Z, Chen X. Graphitic- $\text{C}_3\text{N}_4$  nanosheets: synergistic effects of hydrogenation and n/n junctions for enhanced photocatalytic activities. *Dalton T*. 2017;46:10641-9.